



**AFRL-OSR-VA-TR-2013-0115**

## Eye Safe Polycrystalline Lasers

**John Ballato, Joseph Kolis, Oscar Stafsudd  
Clemson University Research Foundation**

**March 2013  
Final Report**

**DISTRIBUTION A: Approved for public release.**

**AIR FORCE RESEARCH LABORATORY  
AF OFFICE OF SCIENTIFIC RESEARCH (AFOSR)  
ARLINGTON, VIRGINIA 22203  
AIR FORCE MATERIEL COMMAND**

**REPORT DOCUMENTATION PAGE**

*Form Approved  
OMB No. 0704-0188*

The public reporting burden for this collection of information is estimated to average 1 hour per response, including the time for reviewing instructions, searching existing data sources, gathering and maintaining the data needed, and completing and reviewing the collection of information. Send comments regarding this burden estimate or any other aspect of this collection of information, including suggestions for reducing the burden, to the Department of Defense, Executive Services and Communications Directorate (0704-0188). Respondents should be aware that notwithstanding any other provision of law, no person shall be subject to any penalty for failing to comply with a collection of information if it does not display a currently valid OMB control number.

**PLEASE DO NOT RETURN YOUR FORM TO THE ABOVE ORGANIZATION.**

<b>1. REPORT DATE (DD-MM-YYYY)</b> 02-08-2013		<b>2. REPORT TYPE</b> FINAL		<b>3. DATES COVERED (From - To)</b> 08/15/2007 - 08/14/2012	
<b>4. TITLE AND SUBTITLE</b>  Eye-Safe Polycrystalline Lasers				<b>5a. CONTRACT NUMBER</b>	
				<b>5b. GRANT NUMBER</b> FA9550-07-1-0566	
				<b>5c. PROGRAM ELEMENT NUMBER</b>	
<b>6. AUTHOR(S)</b> John Ballato (Clemson), Joseph Kolis (Clemson), Oscar Stafsudd (UCLA)				<b>5d. PROJECT NUMBER</b>	
				<b>5e. TASK NUMBER</b>	
				<b>5f. WORK UNIT NUMBER</b>	
<b>7. PERFORMING ORGANIZATION NAME(S) AND ADDRESS(ES)</b> Clemson University Research Foundation 91 Technology Drive, AMRL Anderson, SC 29625				<b>8. PERFORMING ORGANIZATION REPORT NUMBER</b>	
<b>9. SPONSORING/MONITORING AGENCY NAME(S) AND ADDRESS(ES)</b> Air Force Office of Science and Research 875 Randolph Street Suite 325 Room 3112 Arlington, VA 22203 Dr. Joan Fuller				<b>10. SPONSOR/MONITOR'S ACRONYM(S)</b>	
				<b>11. SPONSOR/MONITOR'S REPORT NUMBER(S)</b> AFRL-OSR-VA-TR-2013-0115	
<b>12. DISTRIBUTION/AVAILABILITY STATEMENT</b> Distribution A - Approved for Public Release					
<b>13. SUPPLEMENTARY NOTES</b>					
<b>14. ABSTRACT</b> This program developed novel ceramic and single crystal laser gain media as a platform for power scaling to +100 kW class levels. Hydrothermal techniques were used for purification, bulk crystal growth and epitaxial growth of complex crystals. Successive recrystallization of commercial powders exhibited one order of magnitude improvement in purity. Bulk single crystal growth was demonstrated for scandia and lutetia single crystals, as well as several lanthanide-doped homologs. Crystal growth was performed at temperatures of about ¼ the melting point of the oxides. The crystals exhibited higher thermal conductivities than that of YAG. A new technique was developed to apply epitaxial crystal growth to refractory oxide systems. Submicrometer-grained transparent ceramics were fabricated by two-step sintering compacts of these nanopowders followed by hot isostatic pressing. These transparent ceramics exhibited equivalent transparency to that of the single crystal in the near-infrared spectral region and initial lasing results have been successful.					
<b>15. SUBJECT TERMS</b> Transparent ceramics, laser gain media, single crystals, sesquioxides					
<b>16. SECURITY CLASSIFICATION OF:</b>			<b>17. LIMITATION OF ABSTRACT</b>	<b>18. NUMBER OF PAGES</b>	<b>19a. NAME OF RESPONSIBLE PERSON</b>
<b>a. REPORT</b>	<b>b. ABSTRACT</b>	<b>c. THIS PAGE</b>			Dr. Joan Fuller
U	U	U	U	95	<b>19b. TELEPHONE NUMBER (Include area code)</b> 703-696-8457

Reset

# Eye-Safe Polycrystalline Lasers

Final Report submitted in requirement of AFOSR Contract # FA9550-07-1-0566 for work funded through the *High Energy Laser Multidisciplinary Research Initiative* (HEL-MRI) program of the US Department of Defense Joint Technology Office (JTO).

Principal Investigator: Prof. John Ballato, Clemson University

Co-Principal Investigators: Profs. Joseph Kolis, Clemson University and Oscar Stafsudd (UCLA)

The overall objective of this program was to develop, characterize, and demonstrate lasing using ceramic laser media. The use of ceramic laser media technological platform lends itself for further power scaling to +100 kW class level suitable for DEW type systems. Although the principal focus will be on monolithic ceramics there will additionally be a seed project on ceramic fiber lasers.

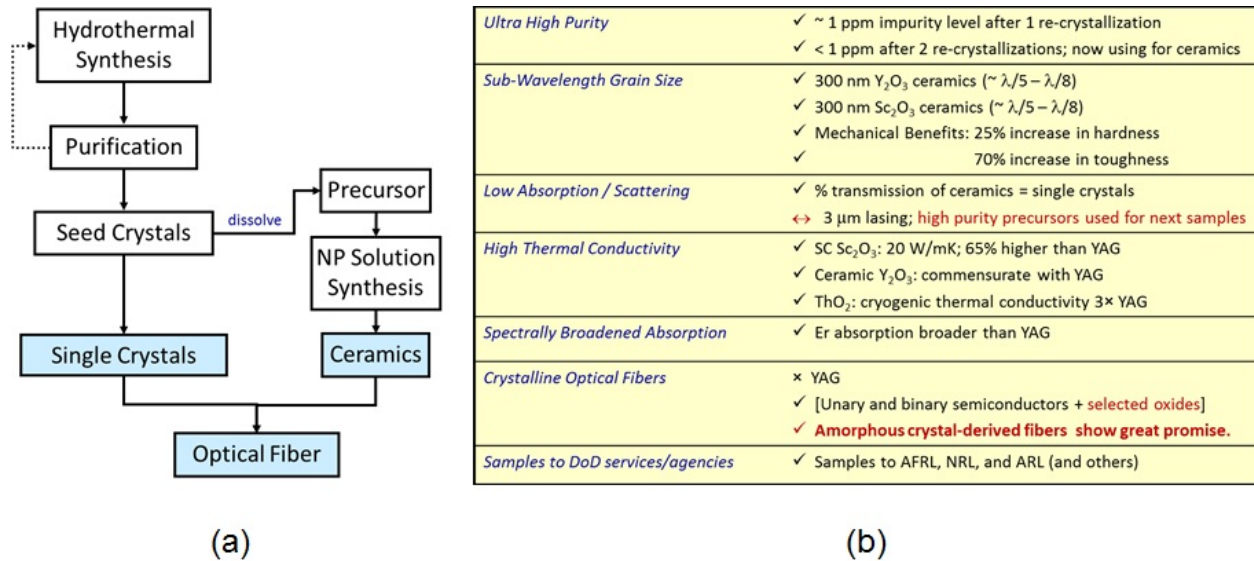


**Figure I.1. (a) Schematic of process flow for fabricating high purity and quality crystals, ceramics, and optical fibers from the same raw-materials. (b) Summary table of goals and successes of this program.**

The technical approach was based on hydrothermal synthetic strategies that lead to the low temperature and low cost fabrication of ultra-pure high-transparency ceramics. Hydrothermal techniques developed at Clemson to grow high purity single crystals were advanced and employed to produce doped nanopowders that subsequently were processed into transparent polycrystalline laser materials; see Figure 1(a). The specific focus will be on Er, Tm, and Ho-doped sesquioxides through garnets were also explored. Starting materials and the finished ceramics should approach the Military Critical Technologies List (MCTL) specifications for Sintered Ceramic Laser Materials (Data Sheet 11.3-10) including ultra-high purity (<1 ppm impurities), nano-scale precursors (<100 nm), low absorption and scattering losses (<0.002 cm<sup>-1</sup>), and high thermal conductivity (>12W/mK). Hydrothermal processes are preferred to other

solid state or solution chemical routes because they permit phase-pure syntheses at considerably lower temperatures (e.g., < 600 °C for Sc<sub>2</sub>O<sub>3</sub>). Such low temperature synthesis yields materials with fewer defects and impurities as well as kinetically hindered compositions, particle morphologies, and enhanced dopants levels than analogs processed at higher temperatures. Hydrothermal methods are used for the production of all synthetic quartz crystals used in frequency control. Accordingly it is a very well established, highly scalable, reproducible, and cost-effective commercial process.

Prior to delving into each topic of this program, a summary of the achieved results are provided in Figure 1 (b). Additionally, following Figure 1, the personnel supported and the scholarly productivity of this program are listed. The technical sections that follow these summaries are sub-divided thematically as follows:

**Section I. Hydrothermal Crystal Growth**

1. *Hydrothermal Crystal Growth Technique*
2. *Purification of Rare Earth Oxides*
3. *Hydrothermal Crystal Growth of Sc<sub>2</sub>O<sub>3</sub> and RE:Sc<sub>2</sub>O<sub>3</sub> Single Crystals*
4. *Hydrothermal Crystal Growth of Lu<sub>2</sub>O<sub>3</sub> and RE:Lu<sub>2</sub>O<sub>3</sub> Single Crystals*
5. *Thermal Conductivity of Rare Earth Oxide Single Crystals*
6. *New Directions: Hydrothermal Epitaxial Growth of YAG*

**Section II. Er-doped Y<sub>2</sub>O<sub>3</sub> Nanoparticles: A Comparison of Different Synthesis Methods**

**Section III: Synthesis, Processing, and Properties of Sub-Wavelength-Grained Highly Transparent Yttria Ceramics**

**Section IV. Sub-micrometer Grain-Sized Transparent Erbium-doped Scandia Ceramics**

**Section V. Synthesis of Er-doped Lu<sub>2</sub>O<sub>3</sub> Nanoparticles and Transparent Ceramics**

**Section VI. On the Fabrication of All-Glass Optical Fibers from Crystals**

**Personnel Supported**

<i>Graduate Students</i>	<i>Undergraduates</i>	<i>Post-Doctoral / Research Associate</i>
1. Evert, Alex	9. Furtick, Joshua	10. Kokuoz, Baris
2. Garcia, Evy		11. Kucera, Courtney
3. Hill Burka, Laura		12. McMillan, Colin
4. Mann, James		
5. Morris, Stephanie		
6. Su, Zhe		
7. Thompson, Daniel		
8. Zhu, Song		

**Journal Publications**

1. C.D. McMillen, M. Mann, J. Fan, L. Zhu, J.W. Kolis, “Revisiting the hydrothermal growth of YAG,” *J. Cryst. Growth* 356 (2012) 58-64.
2. C.D. McMillen, J.W. Kolis, “Bulk single crystal growth in hydrothermal solutions,” *Phil. Mag.* 92 (2012) 2686-2711. (invited review)

3. C. McMillen, D. Thompson, T. Tritt, J. Kolis, "Hydrothermal single crystal growth of  $\text{Lu}_2\text{O}_3$  and lanthanide-doped  $\text{Lu}_2\text{O}_3$ ," *Cryst. Growth Design* **11** (2011) 4386-4391.
4. C. Moore, C.D. McMillen, J.W. Kolis, "Hydrothermal Growth of Single Crystals of  $\text{Lu}_3\text{Al}_5\text{O}_{12}$  (LuAG) and its Doped Analogs" *Crystal Growth and Design*, **2013**, submitted
5. K. Serivalsatit, B. Yazgan Kokuoz, B. Kokuoz, and J. Ballato "Nano-Grained Highly Transparent Yttria Ceramics," *Optics Letters* **34**, 1033 – 1035 (2009). **Highlighted in the June 2009 issue of Laser Focus World.**
6. B. Yazgan Kokuoz, K. Serivalsatit, B. Kokuoz, O. Geiculescu, E. McCormick, and J. Ballato, " $\text{Y}_2\text{O}_3$  Nanoparticles: A Comparison of Different Synthesis Methods," *Journal of the American Ceramic Society*, **92** 2247 – 2253 (2009).
7. K. Serivalsatit, B. Kokuoz, B. Yazgan-Kokuoz, I. Rook, M. Kennedy and J. Ballato, "The Synthesis, Processing, and Properties of Sub-micron Grained Highly Transparent Yttria Ceramics," *Journal of the American Ceramic Society* **93**, 1320 – 1325 (2010).
8. P. Dragic, P.-C. Law, J. Ballato, T. Hawkins, and P. Foy, "Brillouin Spectroscopy of YAG-Derived Optical Fibers," *Optics Express* **18**, 10055 – 10067 (2010).
9. K. Serivalsatit and J. Ballato, "Sub-micrometer Grain-Sized Transparent Scandia Ceramics," *Journal of the American Ceramic Society* **93**, 3657 – 3662 (2010).
10. A. Joshi, O. Stafsudd, K. Serivalsatit, and J. Ballato, "Multiphonon-based Comparison of Erbium-Doped Yttria in Large, Fine Grain Polycrystalline Ceramics and Precursor Forms," *Optical Materials* **34**, 95 – 98 (2011).
11. K. Serivalsatit, T. Wasanapiarnpong, C. Kucera, and J. Ballato, "Synthesis of Er-doped  $\text{Lu}_2\text{O}_3$  Nanoparticles and Transparent Ceramics," submitted to *Optical Materials* (2012).

### Conference Proceedings

1. J. Ballato, C. McMillen, B. Kokuoz, K. Serivalsatit, B. Kokuoz, and J. Kolis, "The synthesis and properties of rare earth doped yttria and scandia for eye-safe single crystal and ceramic lasers," in *Solid State Lasers XVII: Technology and Devices*, edited by W. Andrew Clarkson, Norman Hodgson, Ramesh K. Shori, Proceedings of SPIE Vol. 6871 (SPIE, Bellingham, WA 2008) 68711G.
2. J. Ballato, J. Kolis, C. McMillen, B. Kokuoz, B. Kokuoz, K Serivalsatit, E. McCormick, P. Foy and T. Hawkins, "Synthesis and Properties of Eye-Safe Single Crystal, Ceramic, and Optical Fiber Sources," Vol. 6871: Solid State Lasers XVII: Technology and Devices, W. Andrew Clarkson; Norman Hodgson; R. Shori, Editor, 68711G (2009).
3. K. Serivalsatit and J. Ballato, "Fabrication of Submicrometer-Grained Transparent Sesquioxide Ceramics," 2011 *IOP Conference Series: Materials Science and Engineering*, (2010).
4. J. Ballato and K. Serivalsatit, "Development of Submicrometer-Grained Highly Transparent Sesquioxide Ceramics," in *Advances in Optical Materials*, OSA Technical Digest (CD) (Optical Society of America, 2011), paper AIWA2.
5. K. Serivalsatit and J. Ballato, "Submicrometer-grained highly transparent sesquioxide ceramics: synthesis, processing, and properties," Proceedings of SPIE, Vol. 8039: Laser Technology for Defense and Security VII, Mark Dubinskii; Stephen G. Post, Editors, 80390W (2011).
6. C. McMillen, C. Moore, J. Kolis, "Hydrothermal crystal growth and epitaxy in garnet systems," OSA Technical Digest, *Advances in Optical Materials (AIOM)*, paper IW5D.2 (2012).

7. Advanced smart multifunctional laser crystals for next generation solid-state lasers” D. C. Brown, K. Kowalski, V. Envid, J. Zembek, J.W. Kolis, C.D. McMillen, H. Giesber Laser Technology for Defense and Security VIII SPIE Proceedings **8381-7** 2012.
8. Cryogenic Yb:YAG Picosecond Laser with High Average Power Visible and Ultraviolet Harmonic Generation” D. C. Brown, K. Kowalski, V. Envid, J. Zembek, J.W. Kolis, C.D. McMillen, H. Giesber Laser Technology for Defense and Security VIII SPIE Proceedings **8381-29** 2012.

### Invited Presentations

1. C. McMillen, J. Kolis, and J. Ballato, “Growth and Properties of Doped Scandia Crystals,” IEEE LEOS, Lake Buena Vista, FL, October 2007.
2. J. Ballato, C. McMillan, B. Kokuoz, and J. Kolis, “The Synthesis and Properties of Rare Earth Doped Yttria and Scandia for Eye-Safe Single Crystal and Ceramic Lasers,” SPIE Photonics West, San Jose, CA, January 2008.
3. J. Kolis, C. McMillen, B. Kokuoz, B. Kokuoz, K. Serivalsatit, E. McCormick, P. Foy, T. Hawkins, and J. Ballato "Synthesis and Properties of Novel Eye-Safe and Mid-IR Single Crystal, Ceramic, and Optical Fiber Sources“ SPIE Defense and Security, *Laser Source Technology for Defense and Security IV* Conference, Orlando, FL, March 2008.
4. John Ballato, Joseph W. Kolis, Colin D. McMillen, Baris Kokuoz, Basak Kokuoz, Karn Serivalsatit, Exley McCormick, Paul Foy and Thomas Hawkins, “Synthesis and Properties of Eye-Safe Single Crystal, Ceramic, and Optical Fiber Sources,” *21<sup>st</sup> Annual Solid State and Diode Laser Technology Review*, Directed Energy Professional Society (DEPS), Albuquerque, NM, June 2008.
5. J. Kolis, C. McMillen, and J. Ballato, “Hydrothermal Growth of Single Crystals of Refractory Lanthanide Oxides,” American Conference on Crystal Growth and Epitaxy (ACCGE-17), Lake Geneva, WI, August 2009.
6. J. Ballato, “Advances in Transparent Ceramics,” University of Kyoto, Kyoto, Japan, November 2010.
7. J. Ballato, “Advances in Transparent Ceramics and Crystalline Optical Fibers,” Stanford University, Department of Applied Physics Colloquium, Optics and Electronics Seminar Series (AP 483), January 2011.
8. J. Ballato, “Advances in Laser and Infrared Ceramics, Single Crystals, and Crystalline Optical Fibers,” Air Force Research Laboratory, Dayton, OH, June 2011.
9. J. Ballato, B. Kokouz, J. Kolis, and C. McMillen, “Processing and Fabrication of Lanthanide Sesquioxide Transparent Ceramics,” SPIE Photonics West, January 2012.
10. J. Ballato, J. Kolis, C. McMillen, and P. Dragic, “Advances in Crystals for High Energy Laser Applications” **Plenary Talk**, Beam Control and Advanced High Power Laser Conference, Directed Energy Professional Society, Broomfield, CO, June 2012.
11. J. Ballato, “Sub-Micrometer-Grain Size Transparent Sesquioxide Ceramics,” **Richard M. Fulrath Award Lecture**, Materials Science & Technology (MS&T) Annual Meeting, Houston, TX, October 2010.
12. J. Ballato and K. Serivalsatit, “Fabrication of Sub-Micrometer-Grain Size Transparent Sesquioxide Ceramics,” 3rd International Congress on Ceramics (ICC3), Osaka, Japan, November 2010.
13. J. Kolis, C. McMillen, B. Kokuoz, B. Kokuoz, K. Serivalsatit, E. McCormick, P. Foy, T. Hawkins, and J. Ballato "Synthesis and Properties of Novel Eye-Safe and Mid-IR Single

Crystal, Ceramic, and Optical Fiber Sources“ SPIE Defense and Security, *Laser Source Technology for Defense and Security IV* Conference, Orlando, FL, March 2008.

### Contributed Presentations

1. J. Kolis, C. McMillen, B. Kokuoz, B. Kokuoz, K. Serivalsatit, E. McCormick, P. Foy, T. Hawkins, and J. Ballato "Synthesis and Properties of Novel Eye-Safe and Mid-IR Single Crystal, Ceramic, and Optical Fiber Sources“ SPIE Defense and Security, *Laser Source Technology for Defense and Security IV* Conference, Orlando, FL, March 2008.
2. C. McMillen, J. Ballato, J. Kolis, B. Kokuoz, B. Y. Kokuoz, K. Serivalsatit, and E. McCormick, “Synthesis and properties of eye-safe sesquioxide single crystal and transparent ceramic laser sources,” SPIE Defense and Security, *Laser Source Technology for Defense and Security* Conference, Orlando, FL, April 2009.
3. K. Serivalsatit, B. Yazgan Kokuoz, B. Kokuoz, and J. Ballato “Manufacturing Nano- $Y_2O_3$  Ceramics, Characterization and Properties,” 8th Pacific Rim Conference on Ceramic and Glass Technology, Vancouver, British Columbia, Canada, May 2009.
4. K. Serivalsatit, B. Yazgan Kokuoz, B. Kokuoz, and J. Ballato “Sub-micron grained highly transparent  $Y_2O_3$  ceramics: synthesis, processing, and properties,” Glass and Optical Materials Division of the American Ceramic Society Annual Meeting, Corning, NY, May 2010.
5. K. Serivalsatit, L. Burka, B. Kokuoz, B. Yagan-Kokuoz, M. Kennedy, and J. Ballato, “Sub-Micron Grained Highly Transparent Er-doped  $Y_2O_3$  Ceramics: Synthesis, Processing, and Properties,” Photoluminescence in Rare Earths; Photonic Materials and Devices (PRE '10), Florence, Italy, April 2010.
6. C. McMillen, J. Kolis, C. Liu, A. Kaminski, and J. Ballato, “Hydrothermal Growth and Properties of  $KBe_2BO_3F_2$  (KBBF) and  $RbBe_2BO_3F_2$  (RBBF) Single Crystals,” OSA Optics & Photonics Congress, Nonlinear Photonics Topical Meeting, Karlsruhe, Germany, June 2010.
7. J. Ballato and K. Serivalsatit, “Development of Submicrometer –Grained Transparent Er: $Y_2O_3$  Ceramics,” International Conference on Optical, Optoelectronic and Photonic Materials and Applications (ICOOPMA10), Budapest, Hungary, August 2010.
8. J. Ballato, K. Serivalsatit, B. Yazgan Kokuoz, B. Kokuoz, “Synthesis and Properties of Submicrometer-grained Transparent Sesquioxide Ceramics,” 18th International Conference on Advanced Laser Technologies (ALT'10), Egmond aan Zee, the Netherlands, September 2010.
9. J. Ballato and K. Serivalsatit, “Development of Submicrometer-Grained Highly Transparent Sesquioxide Ceramics,” 2011 Advances in Optical Materials (AIOM), Istanbul, Turkey, February 2011.
10. K. Serivalsatit and J. Ballato, “Submicrometer-grained highly transparent sesquioxide ceramics: synthesis, processing, and properties,” SPIE Defense, Security, and Sensing, Orlando, FL, April 2011.
11. K. Serivalsatit and J. Ballato, “Submicrometer-Grained Transparent Sesquioxide Ceramics,” ACerS 2011 Glass and Optical Materials Division, Savannah, GA, May 2011.
12. L. Jacobsohn, K. Serivalsatit, S. Roberts, E. Yukihara, T. DeVol, and J. Ballato, “Fabrication and Scintillation Response of Rare Earth Doped Transparent Ceramics,” ACerS 2011 Glass and Optical Materials Division, Savannah, GA, May 2011.

13. K. Serivalstit and J. Ballato, "Synthesis of Er-doped  $\text{Lu}_2\text{O}_3$  nanoparticles by homogeneous precipitation method," 9<sup>th</sup> International Meeting of Pacific Rim Ceramic Societies (PacRim9), Cairns, Queensland, Australia, July, 2011.
14. P. Dragic, Y.-S. Liu, J. Ballato, T. Hawkins, and P. Foy, "YAG-Derived Fiber For High-Power Narrow-Linewidth Fiber Lasers," SPIE Photonics West, San Francisco, CA, January 2012.
15. J. Schmitt, C. McPherson, R. Walker, C. Kucera, J. Furtick, C. Quarles, L. Jacobsohn, and J. Ballato, "Consolidation of Nanoparticles Towards Transparent Ceramics: Yttria and YAG," Materials Today Virtual Conference: Nanotechnology (2012 – 2013).
16. E. Brown, U. Hommerich, A. Bluiett, S. Trivedi, C. Kucera, and J. Ballato, "Spectroscopic Characterization and Upconversion Processes in Er doped Yttria Ceramics," LASE 2013, Lasers and Applications in Science and Engineering, Solid-State Lasers XXII: Technology and Devices, SPIE Photonics West, San Francisco, CA, February 2013.

# Technical Report

## Section I. Hydrothermal Crystal Growth

### 1. Hydrothermal Crystal Growth Technique

In parallel with the development of transparent ceramics in this program we also sought to grow single crystals of the target oxides to begin a series of direct comparisons between the single crystals and transparent ceramics. Given the difficulty in preparing single crystals of such refractory oxides using melt-based techniques, we employed the hydrothermal growth method. [1] This technique utilizes aqueous solutions at elevated temperatures and pressures to solubilize and grow single crystals of otherwise recalcitrant species. A mineralizer is typically added to the aqueous fluid to aid in dissolution of the feedstock material. The technique is especially suitable for compounds that have an extremely high melting point, melt incongruently or suffer from stoichiometric deficiencies. Such an approach is useful for bulk crystallization as well exploratory synthesis.

Reactions are typically performed in sealed inert metal liners fashioned from silver, gold or platinum. The experiments described herein were performed in silver liners. These liners are contained within an autoclave and can be either fixed against the wall of the autoclave or freely floating within the autoclave. In the second case, additional water is added to the autoclave to serve as counter pressure and equalize the pressure in the floating liner. The closed nature of the liner-autoclave system in hydrothermal crystal growth lends itself to preparation of high purity crystals. Multiple variables can be individually or simultaneously manipulated including pressure, temperature, temperature gradient and mineralizer concentration, so that crystal growth can be optimized. Once optimum conditions have been identified the growth process can be scaled up quite simply by utilizing autoclaves with a larger inner diameter.

The hydrothermal technique is a relatively low temperature crystal growth method compared to traditional melt techniques. Crystal growth studies during this project were performed at 350-650 °C. By comparison, melt growth of the rare earth sesquioxides requires temperatures exceeding 2400 °C. Thus it is reasonable to suspect that crystals grown at much lower temperatures will exhibit less thermally-induced strain. This approach also further limits impurities introduced from the crystal growth crucible. At such low temperatures the inert metal liners do not interact chemically in any way with the mineralizer solution whereas the oxide melts are well known to attack even robust crucibles made from iridium or rhenium. We feel the exploration and development of alternative crystal growth techniques, such as those described in this report are essential to the continued development of advanced optical materials. Within the scope of the broader project, this section of the report specifically addresses efforts to purify rare earth oxides, grow single crystals of  $\text{Sc}_2\text{O}_3$  [2, 3] and  $\text{Lu}_2\text{O}_3$  [5], characterize some fundamental properties of these single crystals and develop novel epitaxial crystal growth techniques based on the hydrothermal method. [5, 6]

### 2. Purification of Rare Earth Oxides

*Introduction and goals.*

One of the great challenges in the development of high power solid state lasers based on refractory oxides is the difficulty obtaining sufficiently pure materials to work with. The same refractory nature that makes the oxides especially appealing for use as a solid-state laser material also complicates its purification. This is true in the context of single crystals as well as transparent ceramics. However, the crystal growth process is a purifying process in itself, so it can be useful to achieve improvements in purity as the crystal is growing. If the principles of purification by crystal growth could be applied to a precursor useful in the preparation of transparent ceramics, a synergistic approach could be suitable for helping improve the purity and performance in transparent ceramics.

As demonstrated throughout this report, hydrothermal fluids are useful for dissolving and recrystallizing the refractory sesquioxides in this study. Thus, the oxides should be able to be purified by hydrothermal recrystallization. Further, previous phase studies by Roy and Shafer [7, 8] identified hydroxide ( $\text{RE}(\text{OH})_3$ ) and oxide hydroxide ( $\text{REO}(\text{OH})$ ) species which also form from hydrothermal fluids at lower temperatures. Roy and Shafer never attempted to crystallize these phases as large crystals. However, if the hydrothermal technique could be used to crystallize these oxide precursors, then they could presumably be purified in their hydrated state and then converted to whatever form was required for further processing. Our goals for this portion of the project were to develop a low temperature technique for solubilizing sesquioxide feedstock and crystallizing the hydrated species in suitably large crystals to separate them from any impurity species. Concentration levels of impurity elements would be evaluated by ICP elemental analysis after each crystallization procedure, and the effects of subsequent recrystallizations could be compared. Finally, a scheme for scaling up the recrystallization to produce useful quantities of purified material would be investigated.

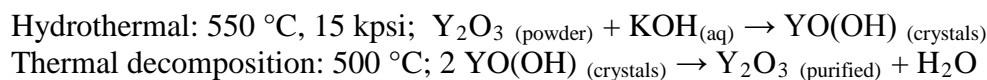
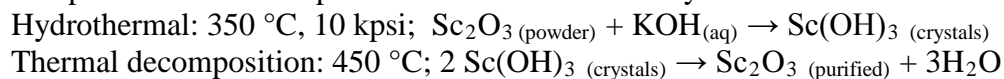
#### *Development of trihydroxide and oxide hydroxide precursors as crystals.*

Using the phase stability studies of Roy and Schafer as a guide, we first sought to crystallize the  $\text{RE}(\text{OH})_3$  and  $\text{REO}(\text{OH})$  compounds as macroscopic crystals. To do so a mineralizer (10 M KOH) was added to the hydrothermal fluid to enhance crystallization in our study. In the  $\text{Sc}_2\text{O}_3$  system, the transition from  $\text{Sc}(\text{OH})_3$  to  $\text{Sc}_2\text{O}_3$  occurs at about 400 °C. Growth at 350 °C resulted in the formation of thin needle-like crystals of the trihydroxide a few millimeters in length. For  $\text{Y}_2\text{O}_3$  and  $\text{Lu}_2\text{O}_3$  the hydrothermal phase diagram is slightly more complex, including a transition from  $\text{Y}(\text{OH})_3$  to  $\text{YO}(\text{OH})$  at about 420 °C and a second transition from  $\text{YO}(\text{OH})$  to  $\text{Y}_2\text{O}_3$  at about 620 °C. The  $\text{Lu}_2\text{O}_3$  system behaves similarly to the  $\text{Y}_2\text{O}_3$  system. In the yttria and lutetia systems the oxide hydroxide species crystallizes extensively from 10 M KOH, forming thick rod-like crystals up to one centimeter in length. As a representative example, hydrothermally-synthesized  $\text{YO}(\text{OH})$  is shown in Figure 2.2.1. Nd, Dy, Ho, Er, Tm and Yb-doped precursors were also readily prepared in this manner with no phase separation. Alternatively, the hydroxide and oxide hydroxide species of those rare earth ions could also be prepared individually.



**Figure 2.2.1: YO(OH) crystallized hydrothermally for purification of Y<sub>2</sub>O<sub>3</sub> powders.**

The procedure used for purification is summarized by these basic reactions:



The as-grown trihydroxide and oxide hydroxide precursors can be easily converted back to the parent oxide compound by simple heating in air at 450-500 °C. The DSC/TGA analyses of the decomposition processes are shown in Figure 2.2.2. The decomposition of YO(OH) indicates a single thermal event at 482 °C corresponding to the loss of 0.5 H<sub>2</sub>O relative to YO(OH) according to the above equations. The observed weight loss was 6.64%, in good agreement with a theoretical loss of 7.38%. The decomposition of Y(OH)<sub>3</sub> consists of two endothermic events. The first step is the loss of 1 H<sub>2</sub>O at 299 °C to produce YO(OH). The second step occurs at 432 °C, and corresponds to the loss of 0.5 H<sub>2</sub>O relative to Y(OH)<sub>3</sub>. Here, the theoretical weight loss is 12.87% for step one and 6.43% for step two. The observed losses of 11.46% and 6.39% are again in agreement. We do note that the YO(OH) resulting from decomposition is slightly destabilized relative to the as-grown YO(OH), as indicated by the lower temperature needed for decomposition to the oxide. Regardless, this has no effect on the resulting Y<sub>2</sub>O<sub>3</sub> that is obtained at the end of the process.

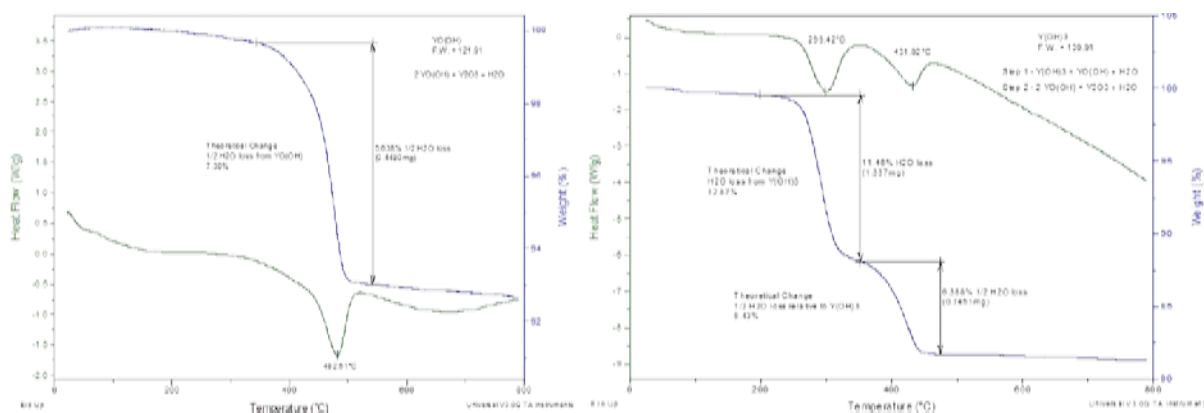


**Figure 2.2.2: Thermal analysis of decomposition of hydroxide and oxide hydroxide precursors.**

This crystallization process could be applied to all of the rare earth oxides, permitting purification of both the host oxides and the dopant oxides. Initial purification reactions were designed to produce ~1 g quantities of REO(OH). Once the process for obtaining large crystals such as those pictured above was found to be repeatable, larger autoclaves were employed. This permitted the production of REO(OH) in ~5-10 g quantities over about a one week period. Further production scaling should be feasible using still larger autoclaves. The preparation of useful quantities of oxide hydroxide precursors is demonstrated for several dopant ions of interest in Figure 2.2.3.



**Figure 2.2.3: From left: YbO(OH) (1g), HoO(OH) (2g), ErO(OH) (5g).**

### *Sequential purification*

To take advantage of the purifying effects of crystallization, hydrothermal crystallization of the precursors followed by thermal decomposition was performed in multiple cycles and the elemental analysis of the resulting  $Sc_2O_3$  or  $Y_2O_3$  powder was evaluated between each crystallization process. An initial survey (Figure 2.3.1) of several elements of interest indicated that, compared to the raw material obtained commercially, the impurity levels were dramatically improved after the first hydrothermal crystallization. In general, small improvements were made

during subsequent recrystallizations. Two recrystallizations was found to be sufficient in reducing the impurity concentrations in the oxides, though more could be applied as needed.

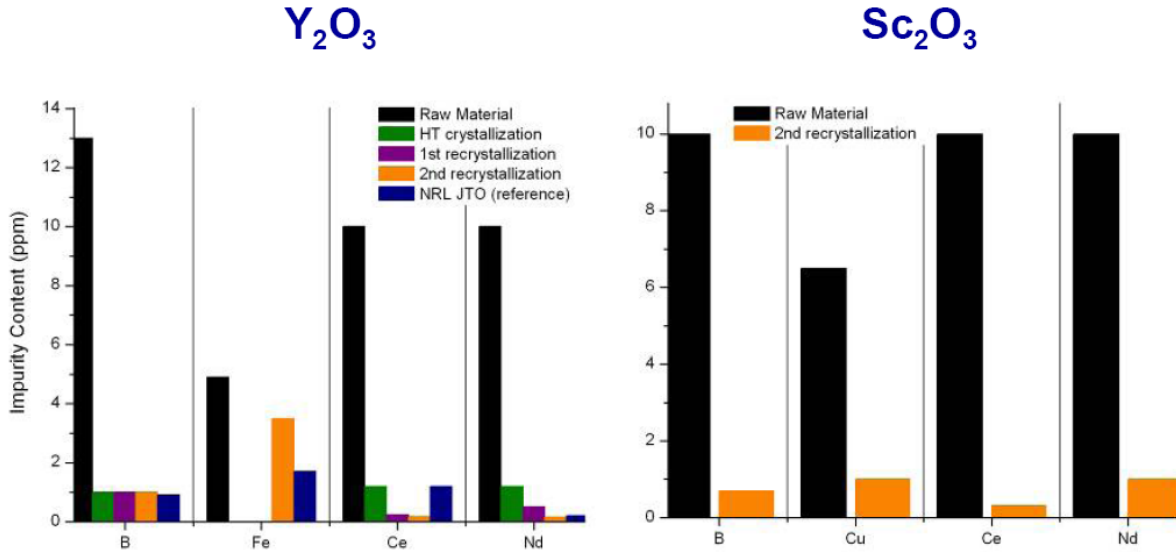


**Figure 2.3.1: Purification by hydrothermal crystallization of yttria and Scandia shown for several impurity elements of interest.**

A more complete survey of the purification is shown in Table 2.3.1. Here the impurity concentrations are compared for the raw material and the oxides obtained after the second recrystallization. We note that in most cases the impurity concentrations have been improved by about an order of magnitude. Some impurities such as Fe and Zn did not exhibit such significant improvement and we are yet unclear as to why this occurred. However, most impurities were reduced to concentrations of 1 ppm or lower, including the rare earth impurities. These are in line with what has been proposed in the past as acceptable impurity levels for preparation of high quality transparent ceramics. Additional recrystallization can be routinely accomplished, or this hydrothermal purification technique could be combined with other established purification techniques in order to achieve further purification. Even so this initial study indicates that high purity material can be easily and quickly prepared by this new technique.

**Table 2.3.1: Oxide purification summary**

Primary impurities	Sc <sub>2</sub> O <sub>3</sub> raw material	Sc <sub>2</sub> O <sub>3</sub> from 2nd re-cryst.	Y <sub>2</sub> O <sub>3</sub> raw material	Y <sub>2</sub> O <sub>3</sub> from 2nd re-cryst.
B	10	0.7	13	1
Mn	1	1.1	1.5	0.85
Fe	7.5	6.4	4.9	3.5
Ni	5.4	1.5	4	0.85
Cu	6.5	1	5	<0.5
Zn	6.5	4.5	5	2.1
La	5	0.26	40	0.54
Ce	10	0.32	10	0.17
Nd	10	1	10	0.15

Eu	1	1	3	1.5
Gd	20	1	20	0.41
Tb	2	0.4	0.5	<0.1

### 3. Hydrothermal Crystal Growth of Sc<sub>2</sub>O<sub>3</sub> and RE:Sc<sub>2</sub>O<sub>3</sub> Single Crystals

Introduction and goals.

In the efforts to extend the capabilities of high power lasers, one of the focuses is developing new materials useful for solid state lasers. Central to this development is identifying those materials with high thermal conductivities (higher than that of YAG) which can facilitate more efficient thermal management during operation at high powers. The rare earth sesquioxides are a particularly intriguing class of compounds in this respect, but their development as single crystals suitable for optical applications has not yet come to fruition. Of the rare earth sesquioxides, Sc<sub>2</sub>O<sub>3</sub> offers a good combination of properties, including a relatively high thermal conductivity, cubic crystal structure, ability to host lanthanide dopants, good hardness and resistance to cracking. [9, 10]

Our goals in this portion of the program were to develop a new technique for the growth of scandia. Once optimized we would use the technique to consistently grow single crystal samples of varying dopants and dopant concentrations for preliminary evaluation of the physical and optical properties.

#### *Spontaneous nucleation and phase stability*

Crystals were first obtained by spontaneous nucleation in 3/8 in. o.d. welded silver ampoules. Powdered Sc<sub>2</sub>O<sub>3</sub> (1 g, Alfa Aesar, 99.9%) was weighed into an ampoule along with solid KOH pellets (2.25–4.5 g, MV Labs, 99.99%). For doped scandia, an amount of the Sc<sub>2</sub>O<sub>3</sub> feedstock was substituted with Ln<sub>2</sub>O<sub>3</sub> (Ln: Ho, Er, Tm, Yb) in the desired ratio. Deionized water (4 mL) was then added, forming the aqueous KOH mineralizer and the ampoule was weld sealed. The ampoule was then placed in an autoclave and the remaining volume was filled with deionized water to serve as counter pressure to prevent the ampoule from bursting. The autoclave was then heated from 400 to 650 °C for 7–21 days.

Sc<sub>2</sub>O<sub>3</sub> was found to be congruently saturating in KOH at temperatures above 400 °C and recrystallizes by spontaneous nucleation. In spite of the high concentrations of KOH used as a mineralizer, no potassium-rich phases were detected and all experiments were phase-pure in scandia. Crystals formed as colorless cubes up to 6 mm in size in some cases. These crystals are pictured in Figure 3.2.1 and were easily of suitable size for use as seed crystals in transport growth experiments. Crystal size increased with increasing temperature, mineralizer concentration and reaction time. These trends are all suggestive of positive-grade solubility and indicate that seeded growth could be possible over a wide range of conditions.

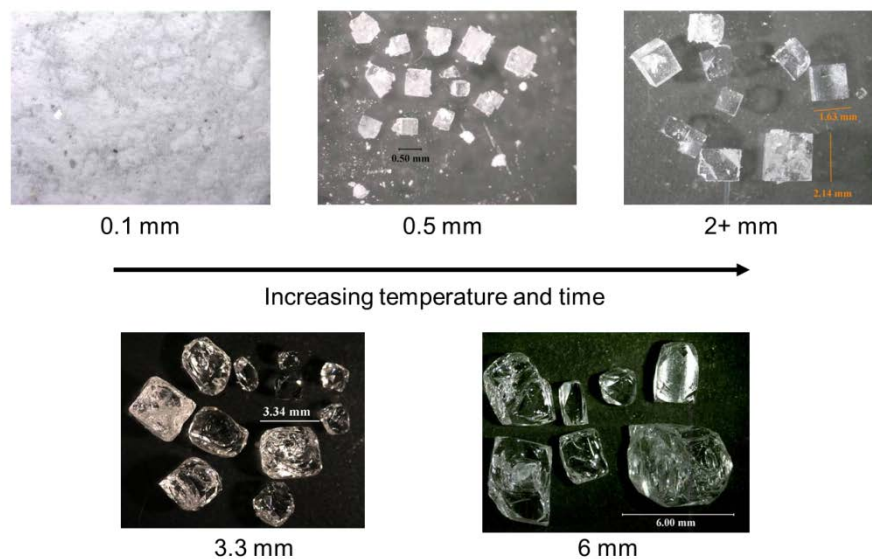


**Figure 3.2.1: Spontaneous nucleation of scandia single crystals.**

Scandia doped with trivalent Ho, Er, Tm and Yb was also obtained by spontaneous nucleation, but crystals were typically less than 2mm in size. Crystals doped with  $\text{Er}^{3+}$  or  $\text{Yb}^{3+}$  tended to be the largest, and these dopants have been incorporated in concentrations ranging from 0.4% to 9.1%. This doping is accompanied by a regular expansion of the unit cell. For example, the unit cell axis length is 9.8444(11) in  $\text{Sc}_2\text{O}_3$ , 9.8529(11) in 1.2%  $\text{Yb}:\text{Sc}_2\text{O}_3$  and 9.9012(11) in 9.1%  $\text{Yb}:\text{Sc}_2\text{O}_3$ . Co-doping is also possible, as small crystals of (Ho, Tm): $\text{Sc}_2\text{O}_3$  and (Er, Yb): $\text{Sc}_2\text{O}_3$  have been obtained by spontaneous nucleation.

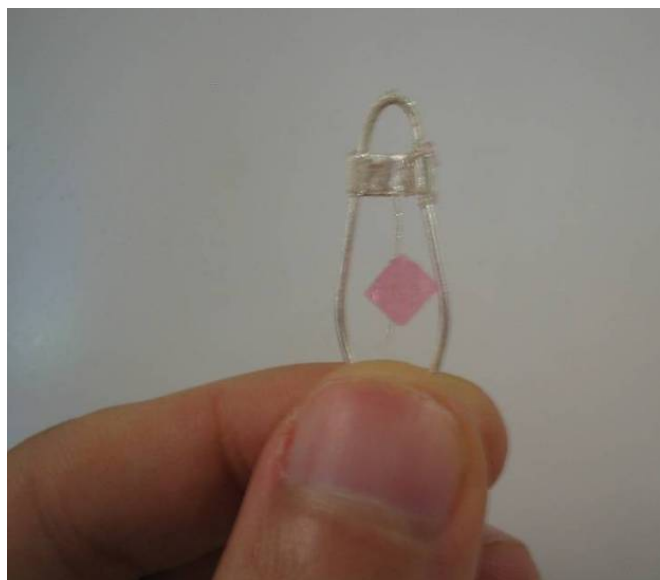


**Figure 3.3.1: Proof-of-concept hydrothermal 3%  $\text{Er}:\text{Sc}_2\text{O}_3$  growth.**

### 3.3. Seeded crystal growth and optimization.

A transport crystal growth survey was also performed to demonstrate proof of mass transport and establish a starting point for the optimization of growth rate and quality. Since  $\text{Er}:\text{Sc}_2\text{O}_3$  of

suitable size for use as seed crystals was not obtained by spontaneous nucleation, initial Er:Sc<sub>2</sub>O<sub>3</sub> growth was directed onto undoped scandia seeds. Growth was performed at 630 °C with a thermal gradient of 45 degrees. The as-grown crystal grown in this experiment is shown in Figure 3.3.1, still attached to the silver ladder on which it was grown. We observed a definitively cubic morphology in the as-grown crystal.

This was an extremely informative experiment, as it also demonstrated that any lattice mismatch imparted by growing a doped layer on an undoped substrate seems to be mitigated using the hydrothermal technique and an interface of good apparent quality is observed. Any defects in the seed were not propagated especially far into the new growth. Figure 3.3.2 shows this interface as an optical and electron micrograph. This holds promise for future epitaxial hydrothermal growth studies of oxide single crystals.

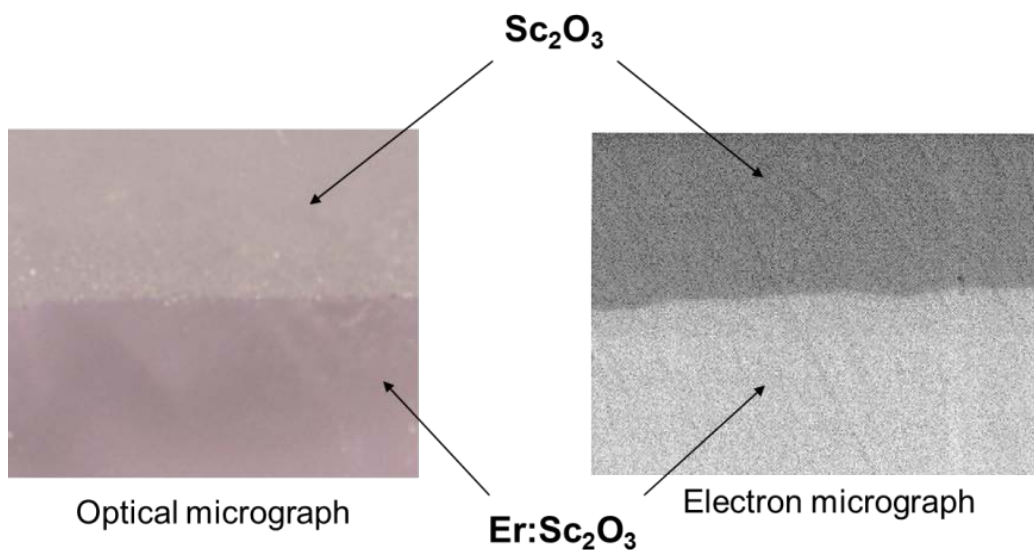


**Figure 3.3.2: Examination of the interface between the Er-doped new growth and the undoped substrate after hydrothermal growth.**

The success of the initial growth experiment also enabled further transport experiments to be performed by harvesting well developed, oriented faces from this now larger crystal. A thin (1 0 0) slice of new Er:Sc<sub>2</sub>O<sub>3</sub> growth from these initial experiments was then used as a seed crystal for subsequent Er:Sc<sub>2</sub>O<sub>3</sub> growth experiments. Thus the growth process was found to be repeatable and new seed crystals were constantly being generated with each subsequent growth experiment. A wide range of conditions (500-650 °C) was studied for Sc<sub>2</sub>O<sub>3</sub> and Er:Sc<sub>2</sub>O<sub>3</sub> with typical growth rates of 0.5-1 mm/week observed. The temperature and thermal gradient were varied to identify the conditions resulting in the best apparent optical clarity. Optimization of the growth rate (Figure 3.3.3) was noted to occur at 650 °C with a thermal gradient of 35 degrees. However, improvements in optical clarity were noticed at lower thermal gradients and growth of optical quality crystals was preferred at gradients of 20-30 degrees. The growth rate was also reduced at wider thermal gradients, but in this case the rate was quenched due to excessive spontaneous nucleation at the top of the autoclave near the seed crystal. This produced a large

number of competitive growth sites where feedstock was deposited, slowing growth on the seed crystal. Thus, conditions of 600-650 °C with a gradient of 20-30 degrees and a 20 M KOH mineralizer solution were found to be optimum. A collection of the as-grown crystals grown during the optimization study is shown in Figure 3.3.4. Large regions of transparent material were exposed after fabrication (Figure 3.3.4, right). Parallel flats were polished and crystals were prepared for optical and physical properties characterization.

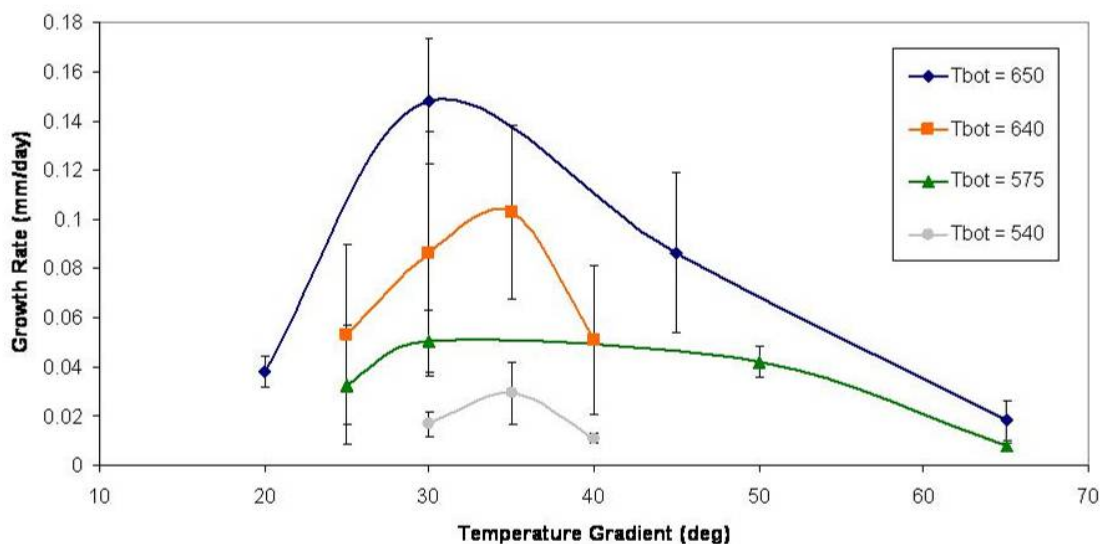


Figure 3.3.3: Growth rate optimization of  $\text{Sc}_2\text{O}_3$ .

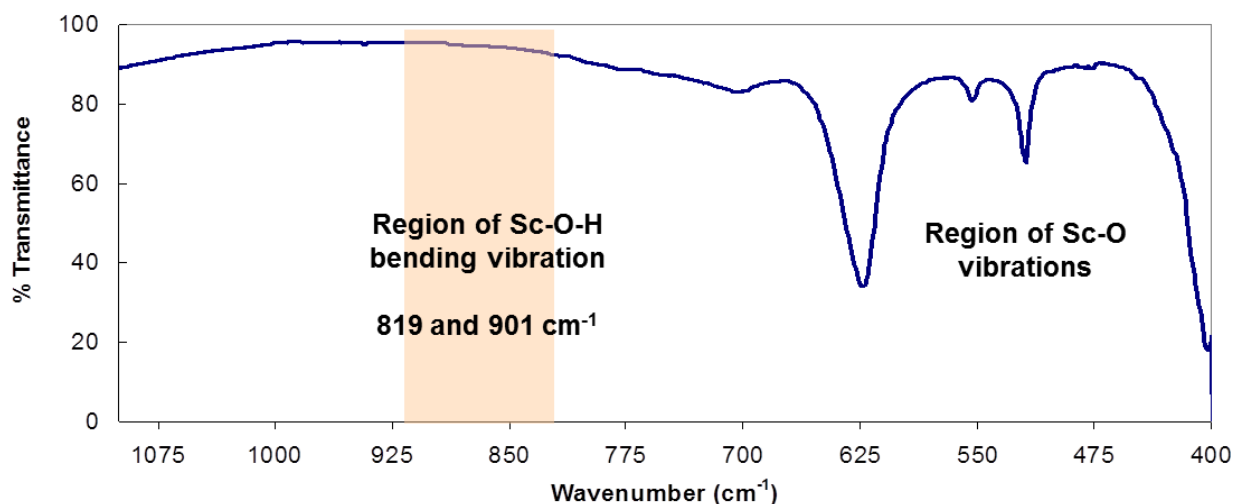


Figure 3.3.4: Left: As-grown scandia and Er-doped scandia single crystals. Right: Scandia single crystals after fabrication. The bottom right image shows Er: $\text{Sc}_2\text{O}_3$  (left) and Yb: $\text{Sc}_2\text{O}_3$  (right) crystals.

#### Characterization

Infrared spectroscopy was used to determine whether any hydroxide from the aqueous mineralizer solution was incorporated into the crystal structure of the new growth. Unlike hydrothermally grown quartz crystals, these sesquioxides do not exhibit the characteristic OH

band at  $3000\text{-}3500\text{ cm}^{-1}$  (not shown), nor do they exhibit any bands in the region diagnostic for Sc-O-H bending vibrations (Figure 3.4.1). We postulate that this occurs because of the higher growth temperature used for the growth of scandia ( $\sim 600\text{ }^{\circ}\text{C}$ ) than that used for quartz ( $\sim 350\text{ }^{\circ}\text{C}$ ).



**Figure 3.4.1: Infrared absorption spectrum of hydrothermally grown scandia single crystals.**

Optical absorption spectra (Figure 3.4.2) and fluorescence lifetime were also measured on Er:Sc<sub>2</sub>O<sub>3</sub>. The absorption spectra show the typical absorption bands for Er<sup>3+</sup> in the near infrared, with the absorption band into the <sup>4</sup>I<sub>11/2</sub> state centered at 975 nm and the absorption band into the <sup>4</sup>I<sub>13/2</sub> state occurring by a complex manifold with the most intense Stark level at about 1538 nm. The fluorescence lifetime was found to be about 5 ms for 0.44% Er:Sc<sub>2</sub>O<sub>3</sub>. This is comparable to that of a 0.5% Er:YAG standard measured for comparison (Figure 3.4.3).

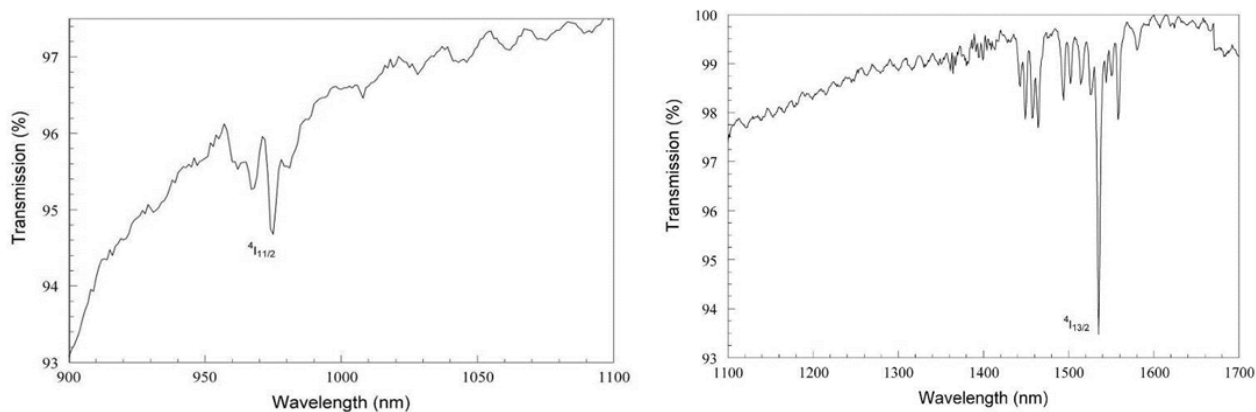


**Figure 3.4.2: Near infrared absorption spectrum of Er:Sc<sub>2</sub>O<sub>3</sub>.**

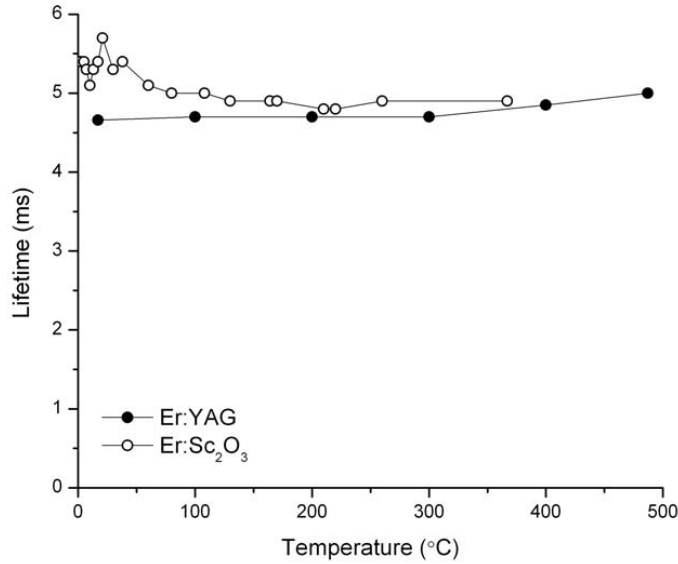


**Figure 3.4.3: Fluorescence lifetime as a function of temperature.**

Co-doping is also possible in Sc<sub>2</sub>O<sub>3</sub>, and crystals were obtained in the same manner as those with a singular dopant. Excitation and emission spectra of (8.1% Yb, 1.7% Er):Sc<sub>2</sub>O<sub>3</sub> are given in Figure 3.4.4. The excitation spectrum was collected at a constant emission of 1550 nm and the emission spectrum at a constant excitation of 980 nm. The peaks observed between 890 and 980 nm are attributed to the  $^2F_{7/2} \rightarrow ^2F_{5/2}$  excitation in Yb<sup>3+</sup>, verifying the proposed mechanism for energy transfer between the  $^2F_{5/2}$  state of Yb<sup>3+</sup> and  $^4I_{11/2}$  state of Er<sup>3+</sup> (which relaxes to the  $^4I_{13/2}$  manifold then to the  $^4I_{15/2}$  ground state to produce the ~1550 nm emission well known for Er<sup>3+</sup>). Direct excitation of Er<sup>3+</sup> occurs at 800 nm as well as some contribution to the 980 nm peak. As expected, the primary emission is from the  $^4I_{13/2} \rightarrow ^4I_{15/2}$  transition at 1540 nm.

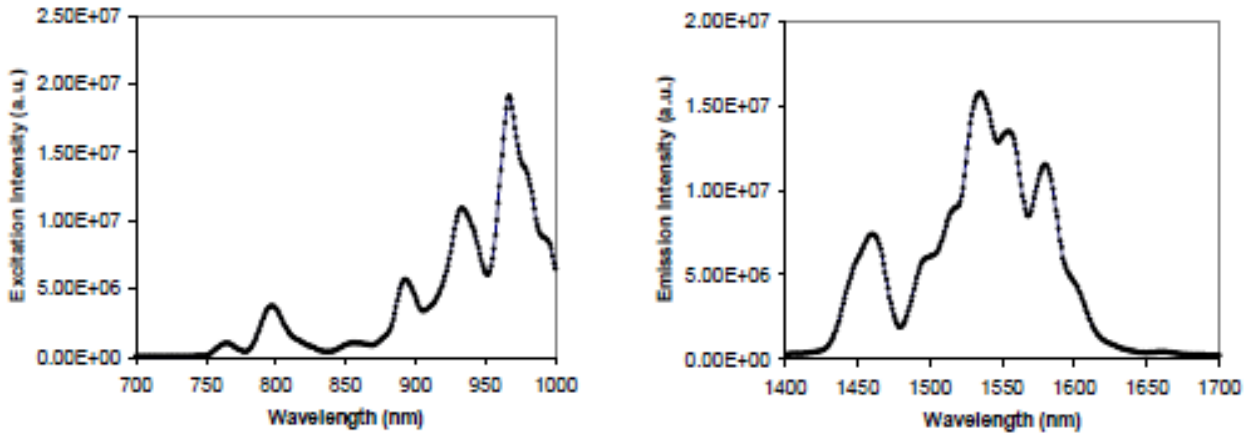


**Figure 3.4.4: Excitation and emission spectrum of Yb,Er co-doped scandia.**

Most of the interesting eye-safe spectroscopy for Ho<sup>3+</sup> and Tm<sup>3+</sup> (>1.8 μm) occurs beyond the detection limit of the instrument used to collect this preliminary data. Ho<sup>3+</sup> has a strong laser emission at 2.06 μm from its  $^5I_7 \rightarrow ^5I_8$  transition and Tm<sup>3+</sup> emits at 1.8-1.9 μm from its  $^3F_4 \rightarrow$

$^3H_6$  transition. However, a 1.5  $\mu\text{m}$  emission is also present for  $\text{Tm}^{3+}$  and can be accentuated by co-doping with  $\text{Ho}^{3+}$ . The  $^3H_4 \rightarrow ^3F_4$  transition that lases at 1.5  $\mu\text{m}$  is shown in the excitation and emission spectra for  $\text{Ho,Tm:Sc}_2\text{O}_3$  (2%  $\text{Ho}^{3+}$ , 0.5%  $\text{Tm}^{3+}$ ) in 3.4.5. The excitation spectrum was measured based on a steady 1575 nm emission, while the emission spectrum was recorded from 780 nm excitation. This verifies that a number of useful co-doping schemes can be pursued in the future in these sesquioxide systems.

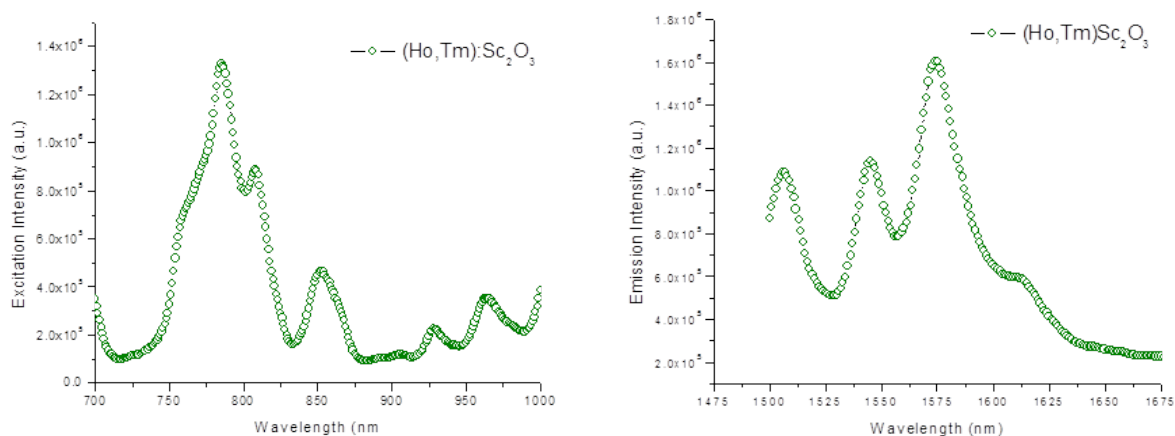


**Figure 3.4.5: Excitation and emission spectra of  $\text{Ho,Tm:Sc}_2\text{O}_3$  single crystals.**

Several physical properties were measured on undoped scandia to obtain baseline values for single crystalline material. Thermal conductivity measurements are discussed in specific detail in a later section of this report. Coefficient of thermal expansion (CTE) measurements as percent linear expansion were also made from 100-800  $^{\circ}\text{C}$ . This is shown in Figure 3.4.6. We note a linear increase in percent linear expansion from 100-800  $^{\circ}\text{C}$ . This results in a calculated CTE of  $12.2725 \times 10^{-6} / ^{\circ}\text{C}$  for the hydrothermally-grown single crystal.

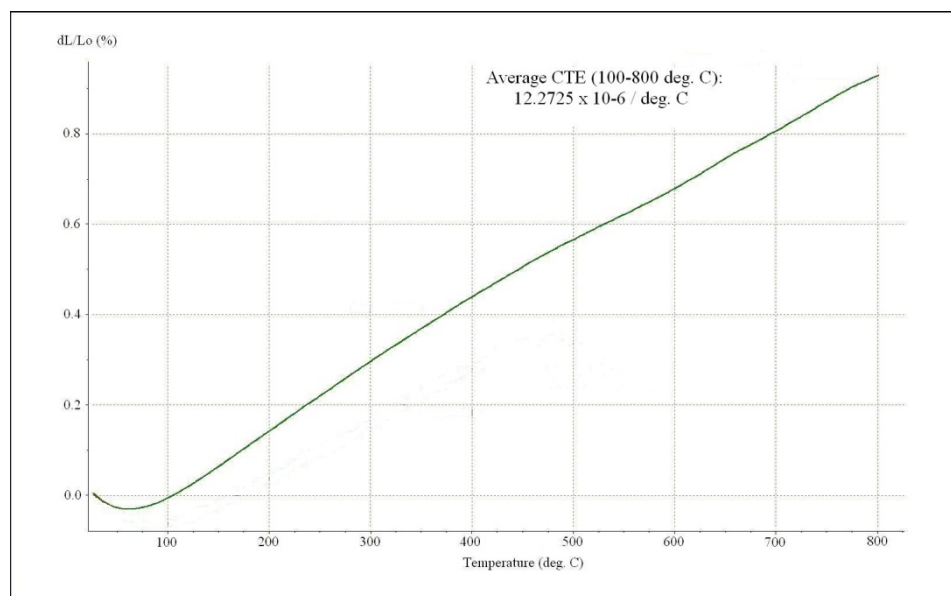


**Figure 3.4.6: Percent linear expansion of undoped scandia.**

#### **4. Hydrothermal Crystal Growth of Lu<sub>2</sub>O<sub>3</sub> and RE:Lu<sub>2</sub>O<sub>3</sub> Single Crystals**

##### *Introduction and goals*

To alleviate some of the challenges in thermal management in high power lasers an ideal scenario would be to utilize a host material whose host ion mass closely matches those of the dopant ions to produce a doped crystal having the highest possible thermal conductivity. In the case of the rare earth oxides, the ideal host ion would be Lu<sup>3+</sup>, since it is closest in size and mass to the primary dopant ions of interest, Yb<sup>3+</sup> and Er<sup>3+</sup>. Thus the technology applied to develop Sc<sub>2</sub>O<sub>3</sub> as a host single crystal was applied to Lu<sub>2</sub>O<sub>3</sub> in this portion of the study.

Like the other rare earth oxides, the high melting point of Lu<sub>2</sub>O<sub>3</sub> presents a challenging crystal growth problem, with limited success being achieved primarily using the heat exchanger method. [11,12] Crystals grown by that method again tend to be primarily polycrystalline and often suffer from thermal strain, oxygen defects and inclusions from the crucible. Even so some encouraging preliminary studies on small single crystals have indicated lutetia to be a promising laser host. [13, 14] However, the growth has not yet proceeded to where single crystals of lutetia are readily available for evaluation and use, and the work is primarily limited to just one overseas research group.

Herein we sought to identify a lower temperature method of crystal growth suitable for the growth of high purity Lu<sub>2</sub>O<sub>3</sub> single crystals. This would enable characterization of fundamental materials properties by providing single crystal baseline data. Following this we planned to extend the hydrothermal technique to demonstrate rare earth doping and seeded crystal growth to prove in concept the growth of multiple crystals and provide an optimized method for the scalable production of testable samples. Preliminary evaluation of the spectroscopy and thermal conductivity of the doped materials would then be undertaken.

##### *Spontaneous nucleation and phase stability.*

Spontaneous nucleation experiments were used to determine the phase stability of Lu<sub>2</sub>O<sub>3</sub> in aqueous hydroxide mineralizer solutions and to synthesize an initial seed crystal required to commence seeded transport growth. Experiments were performed in 3/8" o.d. silver ampoules that were weld-sealed using a tungsten inert gas welder. Lu<sub>2</sub>O<sub>3</sub> powder (1 g, Alfa Aesar, 99.99%) was first weighed into an ampoule along with solid KOH pellets (2.25-4.5 g, MV Labs, 99.99%) and an appropriate amount of deionized water (2-4 mL) was then added to form an aqueous KOH mineralizer of 10-20 M concentration. The ampoule was weld sealed and placed in an autoclave, and the remaining volume of the autoclave was filled with deionized water to serve as counter pressure to prevent the ampoule from bursting during the heating cycle. The autoclave was then heated from 550-660 °C for 7 days, cooled to room temperature (over about 12 hours) and the ampoule was subsequently opened. Er:Lu<sub>2</sub>O<sub>3</sub> and Yb:Lu<sub>2</sub>O<sub>3</sub> crystals were synthesized in the same manner, with substitution of Er<sub>2</sub>O<sub>3</sub> (Aldrich, 99.9%) or Yb<sub>2</sub>O<sub>3</sub> (Alfa Aesar, 99.9%) for Lu<sub>2</sub>O<sub>3</sub> in the desired quantities.

Building on the work of Roy and Schafer on Sc<sub>2</sub>O<sub>3</sub> and Y<sub>2</sub>O<sub>3</sub> done in deionized water, [7, 8] the present study utilized 20 M KOH as a mineralizer to synthesize crystals of the target phase Lu<sub>2</sub>O<sub>3</sub>. Given the chemical similarity of Y<sub>2</sub>O<sub>3</sub> and Lu<sub>2</sub>O<sub>3</sub> we anticipated that hydrothermal

solutions above 600 °C would be required to stabilize lutetia relative to hydrated phases such as LuO(OH) and Lu(OH)<sub>3</sub>. The phase stability from our study in 20 M KOH is shown in Figure 4.2.1. At all temperatures from 550-600 °C we observed only the formation of large (3-8 mm) crystals of LuO(OH). From 600-620 °C a mixture of LuO(OH) and Lu<sub>2</sub>O<sub>3</sub> was obtained. Above 620 °C the cubic Lu<sub>2</sub>O<sub>3</sub> crystals were the lone product, generally occurring in sizes of 0.5-1 mm<sup>3</sup> with one crystal of ~2 mm<sup>3</sup> occurring out of numerous attempted spontaneous nucleation reactions. This lone crystal was harvested for seeded growth reactions and all further seeded growth experiments can be traced to it in some way. Representative crystals from spontaneous nucleation are shown in Figure 4.2.2.

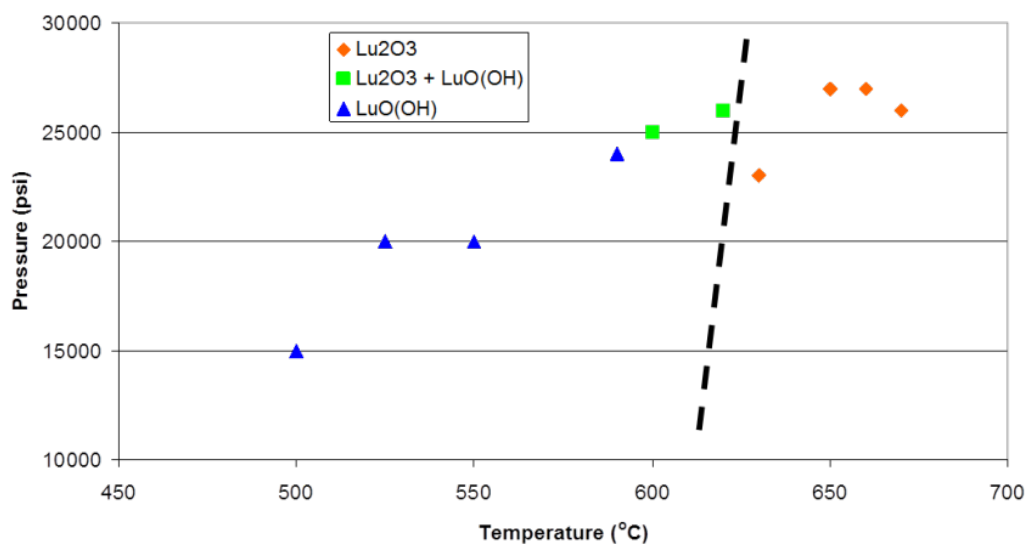
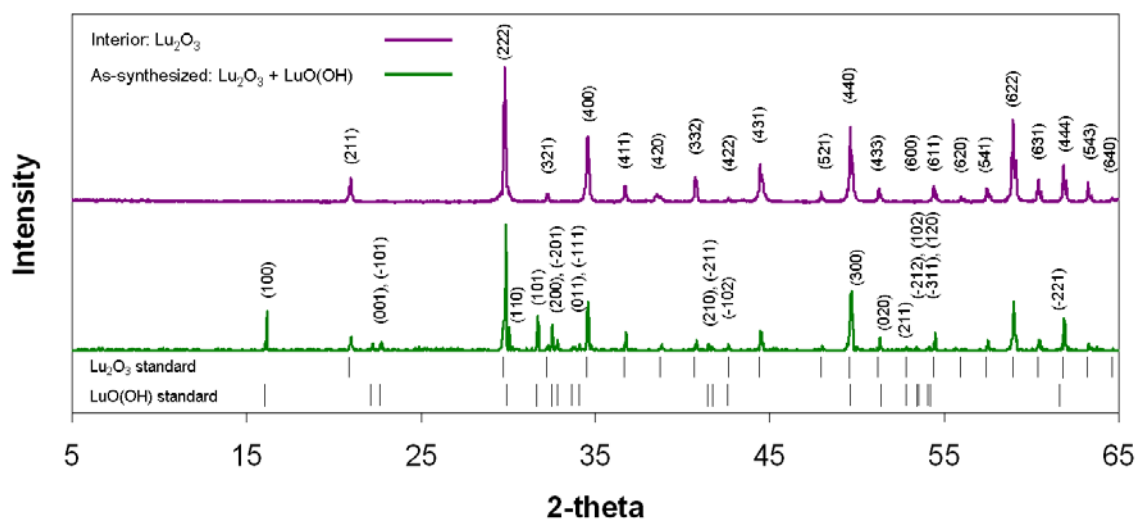


Figure 4.2.1: Phase stability of lutetia in hydrothermal solutions of 20 M KOH.



Figure 4.2.2: Lu<sub>2</sub>O<sub>3</sub> crystals from hydrothermal spontaneous nucleation.

An interesting feature of these cubic crystals is the opaque and irregular material deposited on the outer 50-100  $\mu\text{m}$  of the crystals, physically resembling polycrystalline  $\text{LuO}(\text{OH})$ . However since no bulk  $\text{LuO}(\text{OH})$  crystals were observed in the reaction products, it thus appears that the layer of  $\text{LuO}(\text{OH})$  was deposited only on the outside of nucleated cubic  $\text{Lu}_2\text{O}_3$  crystals. This likely occurs during the cool-down process as the autoclave is cooled through a regime of  $\text{LuO}(\text{OH})$  stability. This was verified by powder XRD in Figure 4.2.3 comparing the powder pattern of the as-synthesized crystals and crystals from the same reaction that have had their outermost surfaces polished away to reveal a clear, colorless interior. The interior is consistent with  $\text{Lu}_2\text{O}_3$ , while the bulk, entire product is a mixture of  $\text{Lu}_2\text{O}_3$  and a smaller amount of  $\text{LuO}(\text{OH})$ .



**Figure 4.2.3: Powder XRD analysis of  $\text{Lu}_2\text{O}_3$  spontaneous nucleation.** (hkl) assignments for  $\text{Lu}_2\text{O}_3$  are made on the top pattern, while (hkl) assignments for  $\text{LuO}(\text{OH})$  are made on the bottom pattern. Positions of the most intense standard reflections for each phase are denoted below the experimental patterns.

#### *Seeded crystal growth and optimization*

Using the largest crystal pictured in Figure 4.2.2 ( $2.3 \times 2.1 \times 1.8 \text{ mm}^3$ ) an initial proof-of-concept mass transport experiment was performed duplicating the conditions producing the largest spontaneous nucleation for 13 days. After transport, the seed crystal grew to a size of  $4.5 \times 4.4 \times 3.2 \text{ mm}^3$ . The new growth was mostly transparent throughout, with the exception of  $\sim 100 \mu\text{m}$  of polycrystalline  $\text{LuO}(\text{OH})$  on the outermost surfaces. This crystal was cut into multiple pieces to be used as seed crystals in subsequent growth experiments designed to optimize growth rate and optical clarity as a function of temperature and temperature gradient and as seeds to grow bulk  $\text{Er}^{3+}$  and  $\text{Yb}^{3+}$  doped crystals. The growth optimization studies were performed at 640 and 650  $^\circ\text{C}$  with thermal gradients of 20-55 degrees to ensure that the growth zone of the autoclave was above 600  $^\circ\text{C}$  to maximize growth of the oxide over nucleation of  $\text{LuO}(\text{OH})$  crystals. This study is summarized in Table 4.3.1. Figure 4.3.1 provides a sampling of the  $\text{Lu}_2\text{O}_3$  crystals grown during the optimization study to provide a point of reference for the reported optical clarity (that is, the optical clarity of the internal  $\text{Lu}_2\text{O}_3$  material after the outer  $\text{LuO}(\text{OH})$  layer has been removed). In all cases the as-grown  $\text{Lu}_2\text{O}_3$  crystals were colorless (or pink in the case of

Er:Lu<sub>2</sub>O<sub>3</sub>) and required no post-growth annealing treatment to remove color centers as is necessary for crystals grown using melt techniques in oxygen-poor atmospheres.

**Table 4.3.1: Lutetia Growth Optimization Summary**

Condi on	Tem p.	Temp. Gradient	Avg. Growth	Apparent Clarity of New Growth, Other Comments
1	650	20	0.74	Clear; some small Lu <sub>2</sub> O <sub>3</sub> spontaneous
2	650	25	0.75	Clear; some small Lu <sub>2</sub> O <sub>3</sub> s.n.
3	650	30	1.03	Most areas clear; some medium-size Lu <sub>2</sub> O <sub>3</sub>
4	650	45	1.07	Mostly clear, cloudy near seed; much Lu <sub>2</sub> O <sub>3</sub>
5	650	50	0.60	Cloudy; significant small Lu <sub>2</sub> O <sub>3</sub> + LuO(OH)
6	650	55	0.65	Mostly cloudy w/ small clear areas; much
7	640	25	0.59	Clear; some small Lu <sub>2</sub> O <sub>3</sub> + LuO(OH) s.n.
8	640	30	0.75	Mostly clear; some small Lu <sub>2</sub> O <sub>3</sub> + LuO(OH)
9	640	35	0.70	Clear and cloudy areas; much Lu <sub>2</sub> O <sub>3</sub> +
10	640	40	0.74	Mostly cloudy; much Lu <sub>2</sub> O <sub>3</sub> + LuO(OH) s.n.

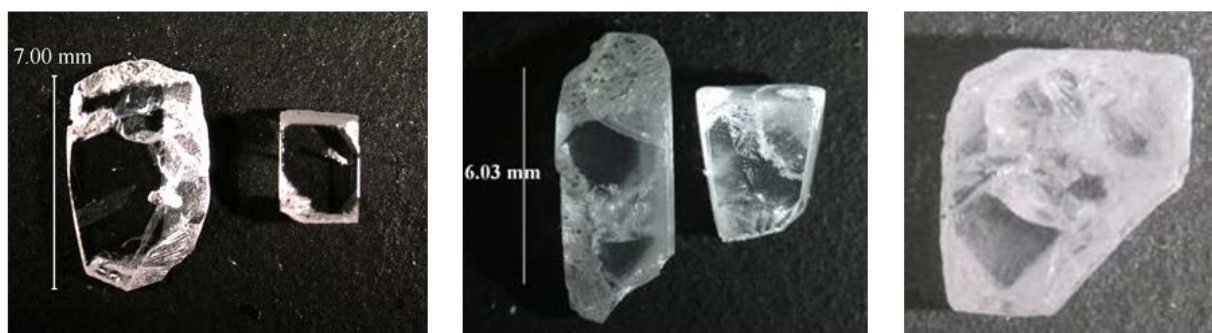


**Figure 4.3.1: Lutetia crystals grown during the optimization study. Referring to the conditions in Table 4.3.1, the crystals were grown by condition 1 (left), condition 3 (center) and condition 4 (right). The silver wire used to tie the crystal to the ladder remains embedded in many of these crystals.**

Average growth rates of 0.55-1.1 mm/week were regularly observed in this study. For all thermal gradients, faster growth always occurred at 650 °C compared to 640 °C presumably because of a greater overall solubility at higher temperatures (which is required for any growth to occur on the seed in this experimental design). Moderate thermal gradients of 30-45 degrees produced the fastest observed growth for both dissolution zone temperatures studied. These conditions afforded a larger solubility gradient than narrower temperature gradients but still minimized competing spontaneous nucleation which quenched growth when wider gradients were used. In terms of optical clarity, a decided dependence on temperature gradient was observed. In all cases lutetia growth resulting from 20-30 degree gradients was fully transparent. Growth using 30-45 degree gradients had mixtures of opaque and transparent regions with opacity generally increasing with wider gradients. The wider gradients of these experiments also correspond to growth zone temperatures that are very close to the border of lutetia stability relative to LuO(OH), so higher temperature experiments are needed to determine whether the

observed opacity truly results from a wider thermal gradient, or if it is rather a function of proximity to the stability limit of lutetia. Regardless it appears in this system the growth zone temperature should be kept well above 600 °C. Thus we identified a dissolution zone temperature of 650 °C with a temperature gradient of 20-30 degrees as optimum conditions for long term bulk growth of optical quality  $\text{Lu}_2\text{O}_3$ ,  $\text{Er}:\text{Lu}_2\text{O}_3$  and  $\text{Yb}:\text{Lu}_2\text{O}_3$ .

Crystals with dimensions up to 7-10 mm were grown over periods of 4-6 weeks, depending on the initial size of the seed crystal. After polishing off the oxide hydroxide surface, the new oxide growth was cut away from the seed crystal and silver wire and then optically polished to yield clear regions 2-5 mm in size. Typical progressions from seed crystals to fabricated, polished pieces resulting from feedstock compositions of 3%  $\text{Er}:\text{Lu}_2\text{O}_3$  and 11%  $\text{Yb}:\text{Lu}_2\text{O}_3$  are shown in Figure 4.3.2. High doping levels were selected in these particular growth experiments to ensure a reasonable detection resolution by EDX and basic optical absorption experiments. The pictured crystals were each grown at 650 °C with a temperature gradient of 20 degrees at an average rate of 0.65 mm/week for  $\text{Er}:\text{Lu}_2\text{O}_3$  and 0.73 mm/week for  $\text{Yb}:\text{Lu}_2\text{O}_3$ . Growth on the  $\text{Er}:\text{Lu}_2\text{O}_3$  seed was also accompanied by some relatively large spontaneous nucleation crystals on the side of the autoclave liner that were also transparent once polished.



**Figure 4.3.2: Growth progression of Er:Lu<sub>2</sub>O<sub>3</sub> (top) and Yb:Lu<sub>2</sub>O<sub>3</sub> (middle) crystals: seed (left), as-grown (center), polished (right). Bottom image shows several transparent doped and undoped lutetia single crystals.**

#### *Preliminary spectroscopic analysis*

The dopant concentrations of the crystals shown above in Figure 4.3.2 were determined by EDX elemental analysis as well as single crystal X-ray diffraction measurement of the lattice parameter. The average concentration of Er<sup>3+</sup> in the resulting Er:Lu<sub>2</sub>O<sub>3</sub> crystals was 3.2 (+/- 0.4) at. % measured by EDX. This doping resulted in a measured increase in unit cell parameter from 10.3980(12) Å in undoped hydrothermal lutetia to 10.4038(12) Å in the doped crystal. EDX of the above Yb:Lu<sub>2</sub>O<sub>3</sub> crystals indicated an average Yb<sup>3+</sup> concentration of 11 (+/- 1) at. %, but a suitable single crystal small enough for lattice parameter measurements by single crystal XRD was not produced in this case. Based on the similarities of the dopant concentrations in the measured crystals to those in the feedstock used to grow them there appears to be minimal partition coefficient difference between the host and dopant ions in these hydrothermal systems and essentially any reasonable dopant concentration can be achieved.

Doping was also verified by absorption spectroscopy shown in Figure 4.4.1. The spectra in Figures 4.4.1a and 4.4.1b are characteristic of the typical near infrared transitions for Yb<sup>3+</sup> and Er<sup>3+</sup>. The <sup>2</sup>F<sub>7/2</sub> to <sup>2</sup>F<sub>5/2</sub> transition in Yb:Lu<sub>2</sub>O<sub>3</sub> spans 900-1040 nm with the most intense absorption into the various Stark levels occurring at 976 nm. This is a unique result, as most typical hosts exhibit a much more intense Stark level absorption at 940 nm when doped with Yb<sup>3+</sup>. The fact that Yb:Lu<sub>2</sub>O<sub>3</sub> exhibits a 976 nm absorption nearly twice as intense as that at 940 nm could have major implications on new pumping schemes developed for Yb-based lasers, and could lead to a lower quantum defect and produce less latent heat. Based on this spectrum from the hydrothermal crystal it appears that pumping at 976 nm will result in the subsequent emission at 1033 nm, which is consistent with melt-grown material (1034 nm). [9] Er:Lu<sub>2</sub>O<sub>3</sub> exhibits an absorption peak centered at 975 nm attributed to the <sup>4</sup>I<sub>15/2</sub> to <sup>4</sup>I<sub>11/2</sub> transition often used to pump the eye-safe 1.5 μm emission that subsequently results from the <sup>4</sup>I<sub>13/2</sub> to <sup>4</sup>I<sub>15/2</sub> transition. The corresponding absorption from the ground state to the <sup>4</sup>I<sub>13/2</sub> manifold is accounted for in this region of Figure 4.4.1b with the most intense absorption occurring at 1536 nm. The intensity of all of these bands in the 1.5 μm region could prove advantageous for resonant pumping. The remaining transitions of Er<sup>3+</sup> occurring in the visible region are resolved in Figure 4.4.1c.

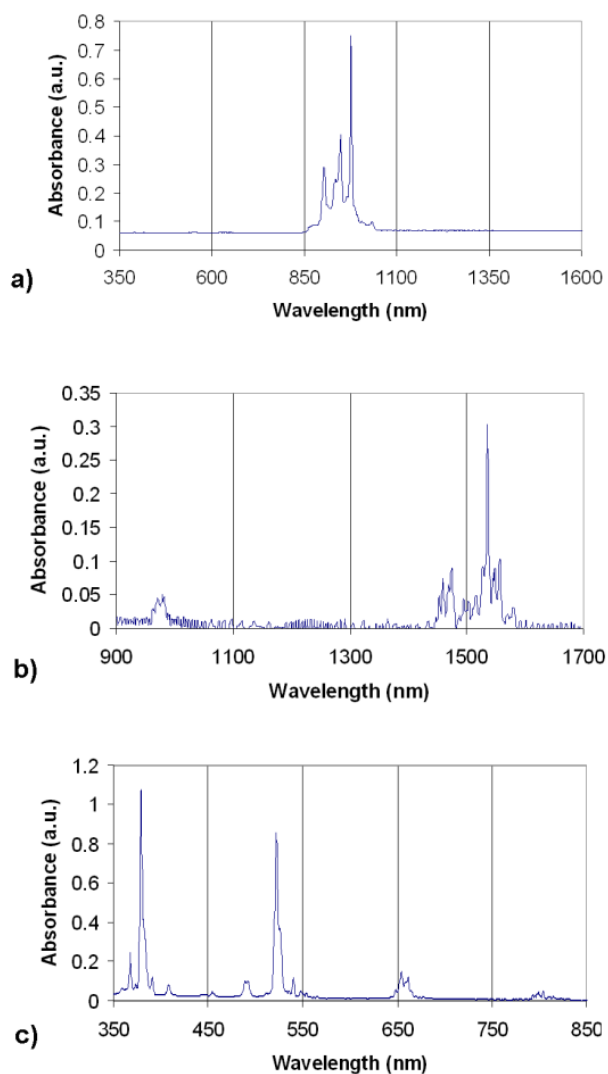


**Figure 4.4.1: Single crystal absorption spectra of hydrothermally-grown samples a) Yb:Lu<sub>2</sub>O<sub>3</sub>, b) Er:Lu<sub>2</sub>O<sub>3</sub> (900-1700 nm) and c) Er:Lu<sub>2</sub>O<sub>3</sub> (350-850 nm).**

## 5. Thermal Conductivity of Rare Earth Oxide Single Crystals

### *Introduction and goals*

The high thermal conductivities of the rare earth oxides make them particularly attractive for high average power solid state laser applications. However, because of the difficulty in obtaining pure, high quality crystals of the sesquioxides already outlined previously, as well as the challenges in making reliable thermal conductivity measurements there is very little consistent, fundamental data available on the thermal conductivity of these oxides. Having demonstrated the growth of high quality crystals of some rare earth sesquioxides we felt we were in a good position to contribute a consistent study of this nature. Further, having grown Er- and Yb-doped single crystals the effects of doping on thermal conductivity could be studied. Knowing the associated drop in thermal conductivity upon doping could be fundamental data in

future efforts to design thermal management systems, as well as identify optimized doping schemes in the crystals.

During this program, the thermal conductivities of pure scandia and lutetia crystals were determined along with the thermal conductivities of the Er-doped scandia, Er-doped lutetia and Yb-doped lutetia. As a reference point single crystals of YAG were also measured using the exact same technique so all discussion can be made relative to YAG data. It is anticipated that thermal conductivity will always decrease upon doping relative to a pure host since any dopant will act as a lattice defect in the phonon transport mechanism. We postulate that the decrease for  $\text{Lu}_2\text{O}_3$  will be significantly less upon doping than it would be for  $\text{Sc}_2\text{O}_3$  or  $\text{Y}_2\text{O}_3$ . For example the similarity in mass between Lu and the dopants Er or Yb would decrease the phonon defects in the doped material.

#### *Thermal conductivity measurement and evaluation*

Thermal conductivity ( $\kappa$ ) measurements were performed on a custom designed system from 10 to 300K using a steady state technique. The system and measurement technique are detailed by Pope et al. [15] Crystals approximately  $2 \times 2 \times 5 \text{ mm}^3$  in size having 3 sets of mutually perpendicular, optically polished parallel flats, were mounted in the removable sample apparatus using Dupont silver paste 4929N. Joule heating establishes a temperature gradient,  $\Delta T$ , across the sample from power,  $P$ , supplied to a  $120 \Omega$  strain gauge resistor mounted on top of the sample. The slope of the  $P$  vs.  $\Delta T$  curve gives the thermal conductance,  $K$ , ( $K = \kappa A/L$ ), where  $A$  is the sample area and  $L$  is the distance between the thermocouples from whence  $\kappa$  is calculated. An undoped YAG crystal was used as an independent standard for comparison. A comparison of undoped host crystals is made in Figure 5.2.1. In the case of undoped  $\text{Sc}_2\text{O}_3$  and  $\text{Lu}_2\text{O}_3$ , both materials show a greater thermal conductivity than YAG at room temperature (ca. 10 W/mK for YAG versus about 12 and 15 for  $\text{Lu}_2\text{O}_3$  and  $\text{Sc}_2\text{O}_3$ , respectively). All the undoped compounds show a substantial increase in thermal conductivity as the temperature is lowered due to the loss of phonon-phonon coupling as expected. We note that the shape of the curves are similar to those of YAG reported previously by Aggarwal et al., but the absolute values of our YAG conductivities at low temperatures are somewhat lower than their values. [16] We attribute this differential to the experimental difficulty in obtaining absolute values of thermal conductivity of our small samples at cryogenic temperatures. For the present we will use the curves as relative values to study the comparative behavior of the samples.

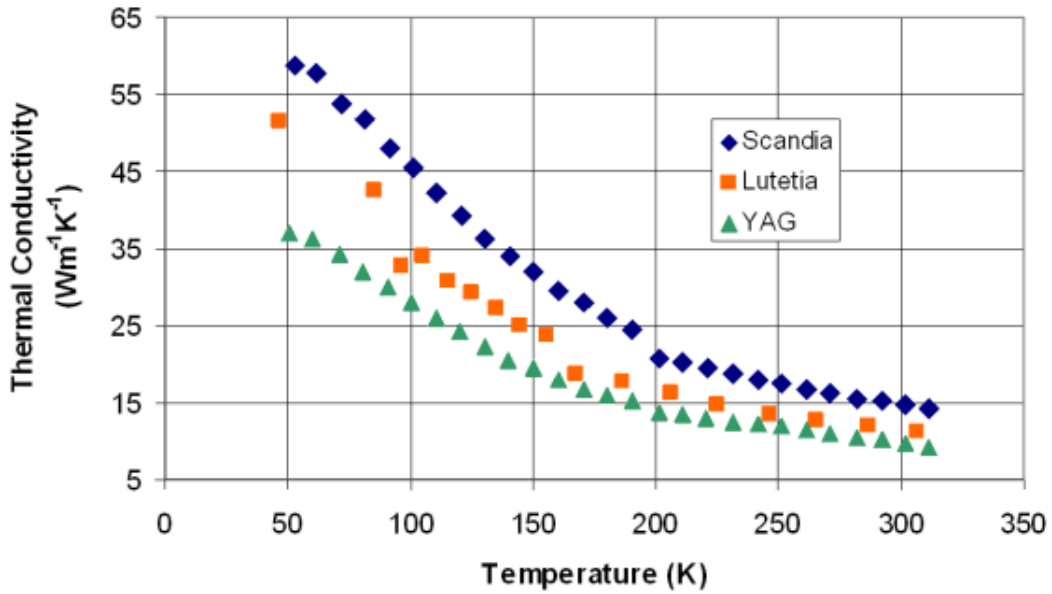


**Figure 5.2.1: Thermal conductivity of undoped oxide single crystals.**

We observe that the thermal conductivity of  $\text{Sc}_2\text{O}_3$  and  $\text{Lu}_2\text{O}_3$  increases dramatically to 77K. It can be noted that the values for undoped  $\text{Sc}_2\text{O}_3$  and  $\text{Lu}_2\text{O}_3$  are respectively about 40 and 30% greater than undoped YAG at 77K. The thermal conductivities of the doped single crystals are shown in Figure 5.2.2. The Er-doped materials show a significant drop off in thermal conductivity as expected, but 3% Er: $\text{Lu}_2\text{O}_3$  shows a significantly smaller drop off than identically doped  $\text{Sc}_2\text{O}_3$  relative to their respective undoped crystals (Figure 5.2.1). Thus 3% Er doped  $\text{Lu}_2\text{O}_3$  shows a 25% decrease to a thermal conductivity of  $\sim 9$  W/mK at room temperature and 50% drop off to about 20 W/mK at 77K, while 3%Er: $\text{Sc}_2\text{O}_3$  shows about a 60% drop off to  $\sim 6$  W/mK at room temperature and nearly a 75% drop off to  $\sim 13$  W/mK at 77K. The effects of Er doping on the thermal conductivities of oxide hosts such as the sesquioxides or garnets are not as commonly discussed in the literature as Yb doping, but the magnitudes of the decreases in thermal conductivity observed in the present study seem reasonable compared to those observed in Yb-doped materials. As expected, Yb doping in  $\text{Lu}_2\text{O}_3$  does not result in such a significant decrease in thermal conductivity as Er doping. We observed only about a 13% decrease in room temperature thermal conductivity (to about 10.5 W/mK) for 11% Yb: $\text{Lu}_2\text{O}_3$ . Other workers have similarly observed only small drops in the room temperature thermal conductivity from Yb doping of lutetium-based oxide hosts, namely about a 10% drop in 3% Yb: $\text{Lu}_2\text{O}_3$ , [11] and about a 4% drop in 10% Yb:LuAG compared to about a 35% drop in 10% Yb:YAG. [17] Thus from a thermal management standpoint  $\text{Lu}_2\text{O}_3$  single crystals appear to be very optimal hosts for Er- or Yb-doped lasers.

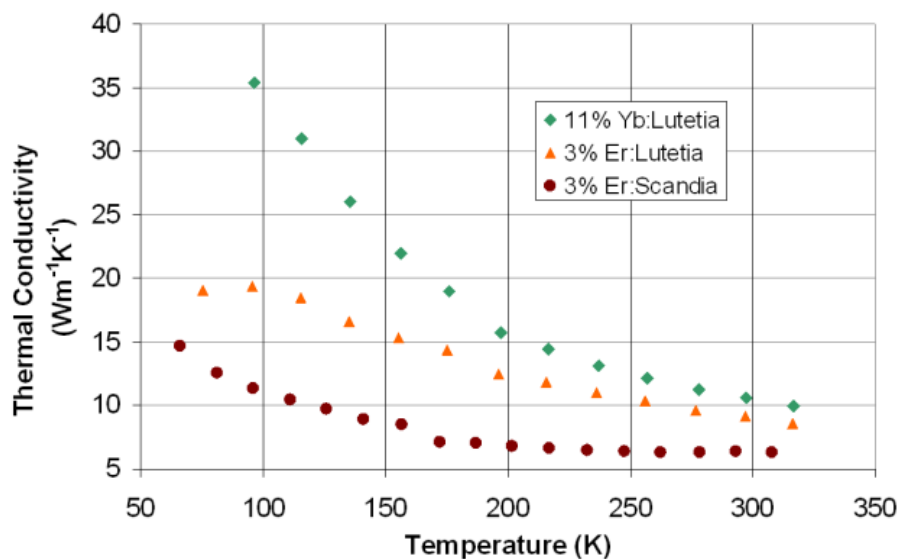


Figure 6: Thermal conductivity of lanthanide-doped sesquioxide single crystals.

## 6. New Directions: Hydrothermal Epitaxial Growth of YAG

### *Introduction and goals*

Having demonstrated an ability to solubilize feedstocks containing refractory oxide powders and crystallize them as high quality single crystals, we sought to extend the study to garnet systems, which are well known for their utility in a variety of applications including solid state lasers. While the growth of garnets such as YAG is well established using traditional crystal growth techniques (unlike the rare earth sesquioxides) the field remains ripe with opportunities to develop new crystal growth ideas, including new crystal compositions, new ways of doing epitaxial growth, growing waveguide single crystals, multifunctional single crystals, and new single crystal architectures. The pursuit of such crystal growth avenues holds great promise for improving optical performance, miniaturizing devices and adding optical functionality.

Reports on the growth of garnets using the hydrothermal technique are generally limited in number and confined to the magnetic garnets. [18, 19] Singular preliminary studies on the growth of YAG and GGG are documented, [20, 21] but these were performed at lower temperatures, 500-550 °C. Given our success growing the sesquioxides at temperatures above 600 °C we felt it was worthwhile to see if any new progress could be made beyond that made 40 years ago. Our goals were to develop the hydrothermal growth technique as a means of epitaxial crystal growth. This could accelerate progress in the area of multifunctional crystals by permitting the growth of single crystals having multiple zones of functionality, rather than relying on diffusion bonding techniques to combine individual crystals. In this portion of the project we focused on two areas: 1) the growth of doped YAG having customized dopant composition and layer thickness, and 2) the growth of crystals having lasing and q-switching functionalities.

### *Epitaxial Growth of YAG*

Transport experiments where the YAG seeds were suspended on a ladder in the upper region of the autoclave and held at a cooler temperature than a feedstock of the component oxides located in the lower region of the autoclave. This feedstock consisted of a stoichiometric mixture of  $Y_2O_3$  powder (Alfa Aesar, 99.99%) and irregularly-sized fragments (0.25-3 mm) of  $Al_2O_3$ . Preliminary experiments suggested that this feedstock combination dissolved and reacted much more favorably than using finely powdered  $Al_2O_3$ . Dopants were introduced as oxides or chlorides in the desired ratio (typically 0.03-5.0 at.%, but sometimes as high as 30 at.%) and aqueous  $K_2CO_3$  was added to reach a fill level of 50-70%. Sealed autoclaves were heated to 600-640 °C using ceramic band heaters to establish the desired thermal gradient between the dissolution and growth zones. These conditions typically resulted in contained pressures of 15-25 kpsi. As an example of the growth of a doped crystal, Nd:YAG was grown during a 21 day reaction from a feedstock consisting of 1.118 g (4.95 mmol)  $Y_2O_3$ , 0.026 g (0.1 mmol)  $NdCl_3$  and 0.84 g (8.24 mmol)  $Al_2O_3$  using 2 M  $K_2CO_3$  as a mineralizer with dissolution and growth zone temperatures of 640 and 610 °C, respectively.

YAG crystals in this study were most often grown on rectangular seed crystals where the most prominent surface was a {100} face. The remaining sides of the seed crystal were oriented either as {100} or {110} crystal forms. Growth experiments using seeds of both orientations exhibited initial hillock growth on the {100} surfaces, but these surfaces tended to become smoother as the layers grew thicker. Average growth rates on the most prominent (100) faces (that is, the increase in thickness along [100]) on those seeds also having {100} sides was 510  $\mu\text{m}/\text{side}/\text{week}$  for a 3-4 week growth period. Comparable growth occurred on the remaining {100} faces (the sides) until these faces terminated. By using thicker seed crystals the time required to terminate growth in these directions could be prolonged and more total lateral growth could be obtained. There was considerable growth rate anisotropy in crystals whose edges were {110} oriented. While these crystals increased in thickness along  $\langle 100 \rangle$  at a similar average rate of 480  $\mu\text{m}/\text{side}/\text{week}$  the average growth rate of the remaining lateral dimensions (along  $\langle 110 \rangle$ ) was much slower, occurring at 95  $\mu\text{m}/\text{side}/\text{week}$ . This is not surprising given the prevalence of {110} forms observed in the spontaneously nucleated material. Because of this, total mass transport was always greater in seeds fully bound by {100} forms. For comparison, a limited number of growth runs were performed using {111} oriented seed crystals, and the average growth rates on these seeds was 205  $\mu\text{m}/\text{side}/\text{week}$  along  $\langle 111 \rangle$ .

The hydrothermal growth of transparent, good quality YAG and rare earth doped YAG crystals with layers of new growth ranging from 0.1-2.75 mm/side in thickness along [100] enables a number of different crystal growth experiments designed to reach various useful crystal configurations. In the simplest form, an undoped YAG seed crystal can serve as a substrate for the growth of doped material. So far we have grown epitaxial layers of YAG doped with the rare earth ions  $Nd^{3+}$ ,  $Sm^{3+}$ ,  $Ho^{3+}$ ,  $Er^{3+}$  and  $Yb^{3+}$ , as well as transition metals such as Co and Cr. A few of these are shown in Figure 6.2.1 as representative examples. In the case of  $Nd^{3+}$  and  $Sm^{3+}$  doping the dopant concentration in the as-grown crystals was typically about half of that contained in the feedstock and further studies will be needed to identify any partitioning of the other dopant ions of interest. In Yb-doped samples we often observe a faint blue-green coloration due to reduction of  $Yb^{3+}$  to  $Yb^{2+}$ . This is easily mitigated by post-growth annealing in air at 1000 °C.

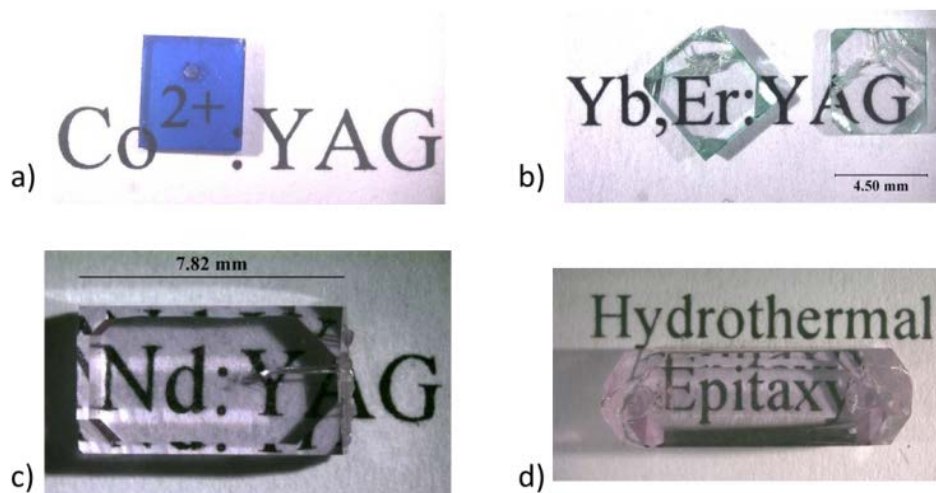


**Figure 6.2.1: YAG crystals coated hydrothermally with epitaxial layers of doped YAG: a) as-grown 1% Co,Si:YAG (100  $\mu\text{m}$  thick layer), b) inspection polished 5% Yb, 0.5% Er:YAG (1.3 mm thick pieces cut away from the seed), c) as-grown 1% Nd:YAG (840  $\mu\text{m}$  thick layers), d) as-grown 1% Nd, 0.03% Ca, 0.03% Cr:YAG (1.7 mm thick layers).**

In the case of the transition metal doping, charge-compensating ions such as  $\text{Ca}^{2+}$  or  $\text{Si}^{4+}$  can be included in the feedstock to target specific oxidation states such as  $\text{Cr}^{4+}$  or  $\text{Co}^{2+}$ , respectively. These are typically included in the feedstock as  $\text{CaO}$ ,  $\text{SiO}_2$ ,  $\text{CrO}_2$  and  $\text{CoCl}_2$ . We note that in the case of  $\text{Ca}^{2+}$ ,  $\text{Cr}^{4+}$  doping (see Figure 6.2.2) the hydrothermal reaction itself does not stabilize the  $\text{Cr}^{4+}$  oxidation state, as the resulting crystals are forest green in color (octahedral  $\text{Cr}^{3+}$ ). However, following the thermal treatment described by Feldman [22] the crystals change color (see Figure 6.2.3) first to bright red at 700  $^\circ\text{C}$  (octahedral  $\text{Cr}^{4+}$ ), then yellow-brown at 1000  $^\circ\text{C}$  (distorted tetrahedral  $\text{Cr}^{4+}$ ). This was confirmed by an optical absorption spectrum exhibiting the tetrahedral  $\text{Cr}^{4+}$  bands around 1 micron and 650 nm (Figure 6.2.2b). It should be noted that the Cr concentrations ( $\sim 1\%$ ) in this experiment may be too large for meaningful q-switching at this thickness, but the concentration was deliberately exaggerated to confirm the spectral and colorimetric transformation. Comparatively, the absorption spectrum of  $\text{Cr}^{3+}$ :YAG prior to thermal treatment exhibits only the typical bands for octahedral  $\text{Cr}^{3+}$  at about 435 and 600 nm.

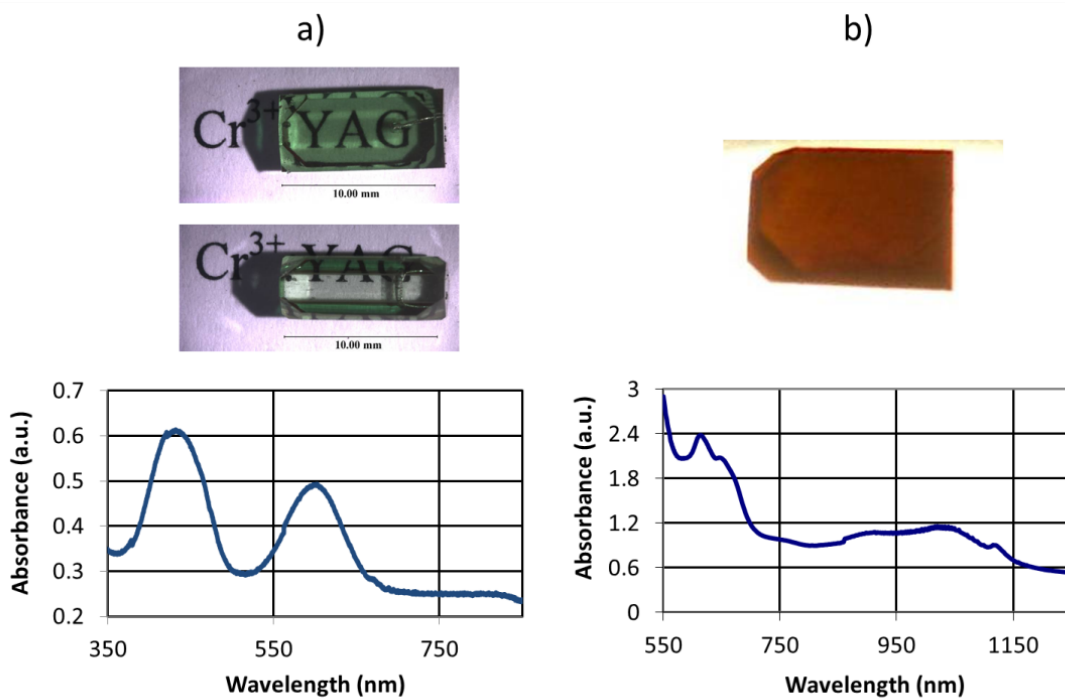


**Figure 6.2.2:** Crystals of Ca,Cr:YAG grown on an undoped YAG substrate and their corresponding absorption spectra: a) as-grown Ca,Cr<sup>3+</sup>:YAG; b) oxidized (post-growth) Ca,Cr<sup>4+</sup>:YAG.

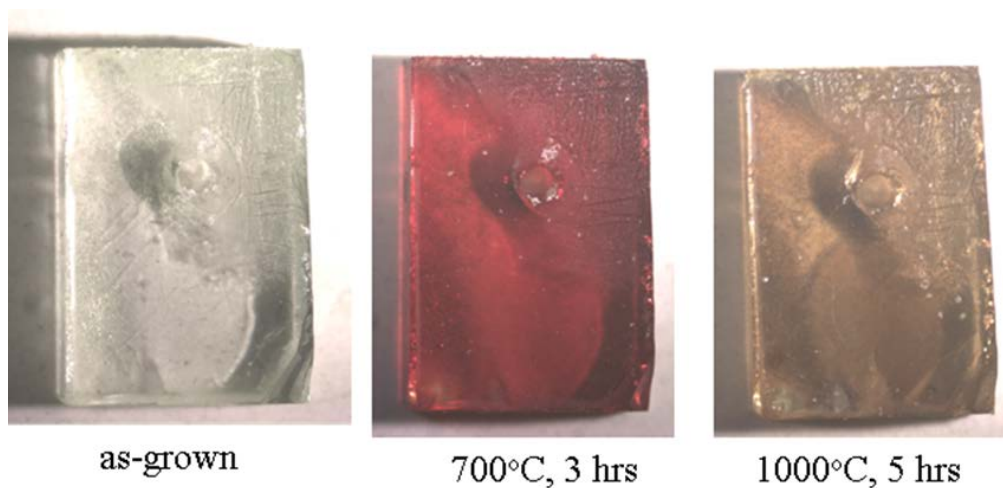


**Figure 6.2.3:** Thermal conversion of Cr<sup>3+</sup>:YAG to Cr<sup>4+</sup>:YAG (0.25% Cr).

More complex arrangements to achieve multifunctional single crystals such as the growth of multiple layers or co-doped crystals were also explored in concept. As an example of a potential eye-safe self-q-switching crystal, a co-doped Yb,Er:YAG crystal was grown on an undoped substrate and the new growth was cleaved. This was used as a substrate for the next epitaxial layer, which was grown to include Co<sup>2+</sup> (with Si<sup>4+</sup> as a charge compensator) as a dopant (since eye-safe q-switching is usually achieved by Co:spinel). The crystal was then cut and polished to reveal the two independent layers of functionality on one crystal. The entire sequence is depicted in Figure 6.2.4. Individual absorption spectra of the layers are shown in Figure 6.2.5

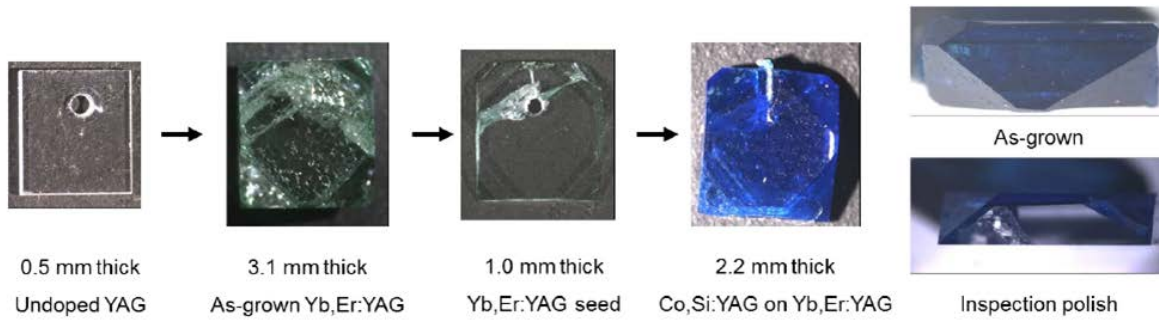


**Figure 6.2.4: Growth of subsequent layers of optical functionality by hydrothermal epitaxy in the YAG system.**

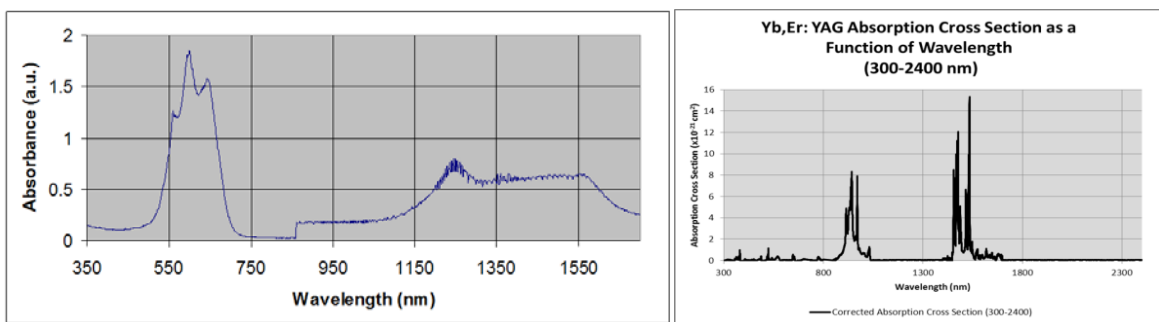


**Figure 6.2.5: Absorption spectra of Co<sup>2+</sup>:YAG (left) and Yb,Er:YAG (right).**

#### *Evaluation of growth/substrate interface quality*

In crystals such as these having multiple layers of functionality the interface between the epitaxial layers deserves some comment. All effort should be made during crystal growth to minimize the presence of absorption or scattering centers. We have tested an approach to optimizing this interface using the hydrothermal epitaxial technique. The apparent quality of the interface is compared in Figure 6.3.1 for two separate crystals grown at 630 °C. The first crystal (top, bottom left) was grown by establishing a dissolution zone temperature of 630 °C and a growth zone temperature of 627 °C for three days, then gradually cooling the growth zone temperature to 600 °C over the next four days. Growth was then allowed to proceed with this 30 degree thermal gradient for three weeks. Alternatively, the second crystal (middle, bottom right) was grown by immediately establishing the 30 degree thermal gradient. In particular when comparing the cross sections of these crystals we observed the presence of a thin cloudy line comprised of numerous inclusions between the seed crystal and the epitaxial layer of Nd:YAG on the crystal where the 30 degree thermal gradient was immediately established. In the sample where the gradient was slowly established only a colorimetric transition from the colorless undoped seed to the lavender growth was observed. The impact of this thin interface on overall crystal clarity is shown in the bottom of Figure 6.3.1.

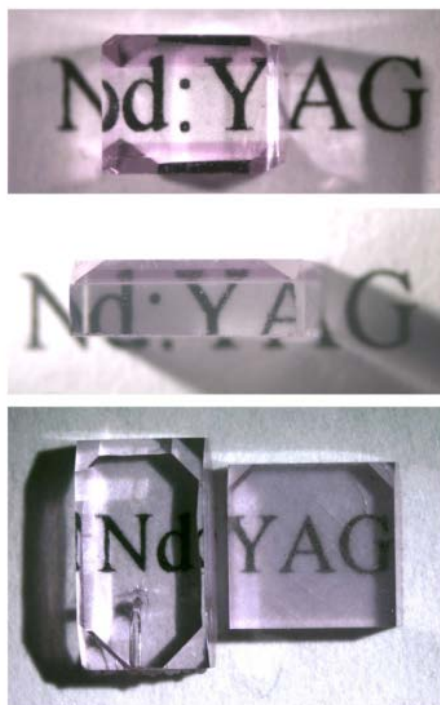


**Figure 6.3.1: Comparison of interfaces between seed crystals and new growth for Nd:YAG crystals grown using a narrow thermal gradient followed by slow expansion of the gradient (top, bottom left) and a wider thermal gradient established immediately (middle, bottom right).**

Characterization of the interface between new growth and the substrate was performed using a laser scattering technique. To investigate the interface scattering, we placed the sample under a microscope and used collimated red light from a He-Ne laser (633nm, Thorlabs HRR020), attenuated by variable neutral density filters, as the incident light. The laser beam was aligned to be perpendicular to the optical axis of the microscope. Therefore only scattered light from the crystal is collected by the microscope and captured by a CCD camera. The imaging system provides a nearly homogenous illumination in the field of view. Two different configurations were used: (1) the incident light is normal to the growth/substrate interface; (2) the incident light is along the length of the growth/substrate interface. In both configurations, the scattered light from the upper side (the new growth) of the sample was used for imaging.

Comparing the scattering images measured for incident light along the interface (Figure 6.3.2, middle), it is clear that the crystal grown using a narrow initial gradient followed by slow expansion to 30 degrees (“slow gradient”) exhibits much less scattering than the crystal grown by immediate establishment of the 30 degree thermal gradient (“fast gradient”). This suggests a nearly seamless transition occurs between the substrate and growth in this “slow gradient” crystal. An obvious scattering pattern associated with the substrate/growth interface is apparent in the “fast gradient” crystal. To distinguish interface scattering from surface scattering, we slowly move the objective lens back and forth and observe any intensity changes that could be associated with surface point defects. The scattering pattern near the interface for the “fast gradient” crystal was essentially unchanged in this test case, meaning scattering effects are almost entirely contributed by the interface. Similarly, when the incident laser is normal to the

interface (Figure 6.3.2, bottom) there is significant scattering observed in the “fast gradient” crystal, and scattering is greatly reduced for the “slow gradient” crystal. The small amount of scattering present in this image (Figure 6.3.2, bottom right) was determined to be caused by point defects on the inspection-polished surface, again by movement of the objective lens.

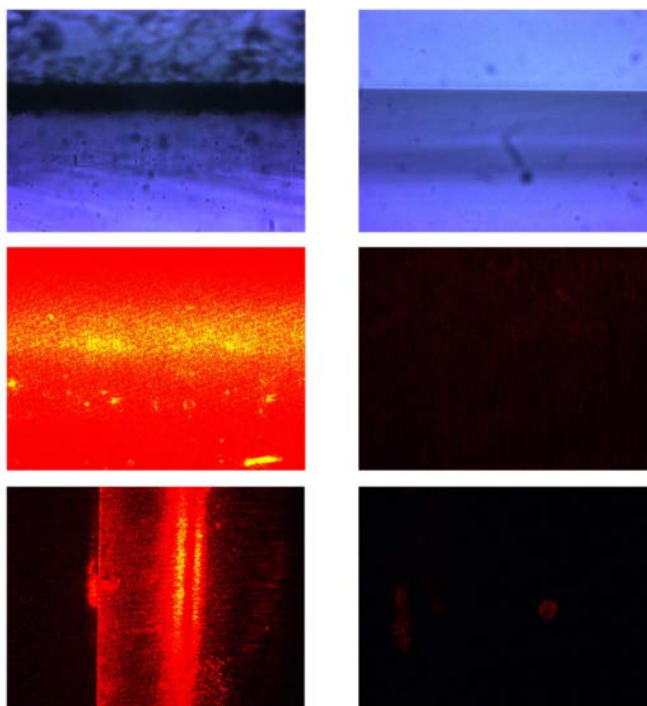


**Figure 6.3.2: Evaluation of the substrate/growth interface for hydrothermal Nd:YAG grown using a narrow thermal gradient followed by slow expansion of the gradient (right, “slow gradient”) and using a thermal gradient established immediately (left, “fast gradient”). Top: white light images at 200x magnification. Middle: laser scattering for incident light along the interface (200x magnification). Bottom: laser scattering for incident light normal to the interface (50 x magnification).**

### Section Conclusions

Single crystal growth was pursued as an aspect of this project to begin the process of comparing fundamental materials properties of single crystal versus transparent ceramic materials. Specifically, the hydrothermal technique was explored in several contexts throughout the course of this project including purification, bulk crystal growth and epitaxial growth of complex crystals. Commercial powders of rare earth oxides were found to readily dissolve in hydrothermal fluids and could be recrystallized in their oxide form, or in other hydrated forms. After successive recrystallization experiments the oxide powders typically exhibited one order of magnitude improvement in their impurity concentrations. The method has so far been scaled to quickly produce multi-gram quantities of high purity oxide material suitable for use as a precursor for the preparation of transparent ceramics. The method was then extended to bulk single crystal growth, and this was demonstrated for scandia and lutetia single crystals, as well as several lanthanide-doped homologs. Crystal growth was performed at temperatures of about  $\frac{1}{4}$  the melting point of the oxides. Transparent crystals of good apparent optical quality were regularly grown and the process was optimized to produce a number of testable samples.

Characterization of various physical and optical properties was performed on these single crystals. In particular, the thermal conductivities of the scandia and lutetia single crystals were studied from room temperature to cryogenic temperatures. As undoped crystals, both materials exhibited higher thermal conductivities than that of YAG. Upon doping with Yb or Er,  $\text{Lu}_2\text{O}_3$  performed particularly well and exhibited a much smaller drop in thermal conductivity upon doping than  $\text{Sc}_2\text{O}_3$  or than that reported for YAG. Thus lutetium containing materials hold great promise for improving thermal management in high average power lasers. Finally, a new technique was developed to apply epitaxial crystal growth to refractory oxide systems. YAG was chosen as a test bed for this work. Hydrothermal epitaxy was shown to be particularly useful in growing YAG crystals with custom dopants and concentrations, as well as developing single crystals which have multiple zones of functionality. The development of new crystal growth techniques and their application to challenging crystal growth problems, including highly refractory oxides like the garnets and sesquioxides appears encouraging for future optical materials development.

### Section References:

1. C.D. McMillen, J.W. Kolis, *Phil. Mag.* 92 (2012) 2686-2711.
2. C.D. McMillen, J.W. Kolis, *J. Cryst. Growth* 310 (2008) 1939-1942.
3. C.D. McMillen, J.W. Kolis, J. Ballato, *Proc. IEEE, Lasers and Electro-Optic Society (LEOS)*, (2007) 437-438.
4. C. McMillen, D. Thompson, T. Tritt, J. Kolis, *Cryst. Growth Des.* 11 (2011) 4386-4391.
5. C. McMillen, C. Moore, J. Kolis, *Proc. OSA, Advances in Optical Materials (AIOM)*, (2012) paper IW5D2.
6. C.D. McMillen, M. Mann, J. Fan, L. Zhu, J.W. Kolis, *J. Cryst. Growth* 356 (2012) 58-64.
7. M.W. Shafer, R. Roy, *Z. Anorg. Allgem. Chem.* 276 (1954) 275-288.
8. M.W. Shafer, R. Roy, *J. Am. Ceram. Soc.* 42 (1959) 563-570.
9. K. Petermann, G. Huber, L. Fornasiero, S. Kuch, E. Mix, V. Peters, S.A. Basun, *J. Lumin.* 87-89 (2000) 973-975.
10. L. Fornasiero, E. Mix, V. Peters, K. Petermann, G. Huber, *Cryst. Res. Technol.* 34 (1999) 255-260.
11. V. Peters, A. Bolz, K. Petermann, G. Huber, *J. Cryst. Growth* 237-239 (2002) 879-883.
12. R. Peters, C. Krankel, K. Petermann, G. Huber, *J. Cryst. Growth* 310 (2008) 1934-1938.
13. S.V. Marchese, C.R.E. Baer, R. Peters, C. Krankel, A.G. Engqvist, M. Golling, D.J.H.C. Maas, K. Petermann, T. Sudmeyer, G. Huber, U. Keller, *Opt. Express* 15 (2007) 16966-16971.
14. C.R.E. Baer, C. Krankel, C.J. Saraceno, O.H. Heckl, M. Golling, R. Peters, K. Petermann, T. Sudmeyer, G. Huber, U. Keller, *Opt. Lett.* 34 (2009) 2823-2825.
15. A.L. Pope, B. Zawilski, T.M. Tritt, *Cryogenics* 41 (2001) 725-731.
16. R.L. Aggarwal, D.J. Ripin, R.J. Ochoa, T.Y. Fan, *J. Appl. Phys.* 98 (2005) 103514-1-103514-14.
17. K. Beil, S.T. Fredrich-Thornton, F. Tellkamp, R. Peters, C. Krankel, K. Petermann, G. Huber, *Opt. Express* 18 (2010) 20712-20722.
18. R.A. Laudise, J.H. Crockett, A.A. Ballman, *J. Phys. Chem.* 65 (1961) 359-361.
19. B. Ferrand, J. Daval, J.C. Joubert, *J. Cryst. Growth* 17 (1972) 312-314.
20. R.C. Puttbach, R.R. Monchamp, J.W. Nielsen, in: H.S. Peiser (Ed.), *Hydrothermal Growth of Y3Al5O12 in Crystal Growth*, Pergamon, Oxford, 1967, pp. 569-571.
21. E.D. Kolb, R.A. Laudise, *J. Cryst. Growth* 29 (1975) 29-39.

22. R. Feldman, Y. Shimony, Z. Burshtein, *Opt. Mater.* 24 (2003) 333-344.

## **Section II. Er-doped $Y_2O_3$ Nanoparticles: A Comparison of Different Synthesis Methods**

**Section Summary:** Nanoparticles of erbium-doped yttria (Er:Y<sub>2</sub>O<sub>3</sub>) are important precursors to transparent ceramics for high power solid state lasers systems. Since structure influences properties and, subsequently, performance the purpose of this work is to compare the morphological and chemical nature of the nanoparticles synthesized using two common methods: solution precipitation and combustion synthesis. A thorough characterization of as-prepared and calcined powders was performed using Fourier transform infrared spectroscopy (FTIR), x-ray diffraction (XRD), conventional (TEM) and high resolution (HR-TEM) transmission electron microscopy, and Brunauer-Emmet-Teller (BET) methods. Solution precipitation was found to lead to two different precursor compositions (yttrium carbonate or yttrium hydroxide) depending on the precipitating reagent whereas combustion synthesis yielded only phase-pure, cubic Er:Y<sub>2</sub>O<sub>3</sub>. The hydroxide precipitation and combustion synthesis methods exhibited agglomerated particles with low surface area after calcining the precursors at 900°C. The addition of a small amount of ammonium sulfate during combustion synthesis was found to reduce the level of agglomeration, resultant particle size and degree of crystallinity of the calcined Er:Y<sub>2</sub>O<sub>3</sub> nanoparticles. The amount of carbon dioxide (CO<sub>2</sub>) and water (H<sub>2</sub>O) on the surface of the Er:Y<sub>2</sub>O<sub>3</sub> powders is dependent on the powder surface area, however increasing levels of gas absorption on the particle surfaces do not have a detrimental effect on the sinterability. The sintered density increases with increasing surface area and decreasing agglomeration.

### **Introduction**

Rare earth-doped yttria (Y<sub>2</sub>O<sub>3</sub>) has generated considerable attention as a gain media in high power solid state laser systems. This is due principally to the higher thermal conductivity and broadened emission line-widths relative to more-conventional hosts like yttrium aluminum garnet (YAG) [1,2]. Since the high melting point of yttria (~ 2450 °C) makes for considerable difficulties in growing single crystals, transparent yttria ceramics are gaining appreciation. Recently, nano-grain-sized Y<sub>2</sub>O<sub>3</sub> ceramic, which exhibited equivalent transparency to that of the single crystal beyond 1200 nm was fabricated by pressure assisted sintering [3]. The single-crystal-like transmittance of the nano-grained yttria ceramics in the visible and infrared region is represents an important advance especially for high power laser hosts where transparency must be maximized.

In order to minimize scattering and achieve a high degree of transparency, a nearly pore free (<0.01%) microstructure is essential. Although pressure-assisted sintering methods such as hot pressing or hot isostatic pressing can promote full densification, fine porosity may still be trapped and left inside grains after these processes if the starting powders are highly agglomerated [4]. This residual porosity tends to greatly reduce the in-line transmittance. Therefore, the importance of synthesizing ultra-fine, highly sinterable nanopowders becomes clear [5].

Combustion synthesis [6] and solution precipitation [7-10] are among the various methods to fabricate  $Y_2O_3$  nano powders. Previous efforts have studied the effect of synthesis method [6-8] and calcination temperature [9,10] on particle characteristics. However, a thorough comparison of the characteristics of the as-prepared and calcined  $Y_2O_3$  nanopowders fabricated through these two efficient synthesis approaches has not been made so far.

While the increased sinterability that is associated with the large surface area of ultra-fine  $Y_2O_3$  particles aids in reducing the sintering temperatures [8,9] it also can be responsible for undesired agglomeration and adsorption of atmospheric gases (such as  $CO_2$ ) on the particle surfaces [11]. These gases can react and form carbonate compounds and further evolve  $CO_2$  gas during sintering. This  $CO_2$  release during sintering could remain as residual porosity within the sintered body and, thus reduce the optical quality of  $Y_2O_3$  transparent ceramics [12].

The purpose of this section is to compare erbium- doped yttria ( $Er:Y_2O_3$ ) nanopowders synthesized using two different synthesis methods: solution precipitation and combustion synthesis. The use of erbium as a dopant is because it has an efficient emission at 1.55  $\mu m$  that is considered more eye-safe than the shorter wavelength emissions of  $Nd^{3+}$  and  $Yb^{3+}$  at approximately 1  $\mu m$  in wavelength [13]. More specifically, the precursor characteristics, size and morphology, as well as the  $CO_2$  and  $H_2O$  absorption on the surfaces of the  $Er:Y_2O_3$  powders are compared with the aim of developing the level of understanding of the factors that influence the sinterability of  $Y_2O_3$  nanopowders.

## **Selected Procedures**

### *Powder Synthesis: Solution Precipitation*

The solution precipitation method involved two different precipitation routes for the synthesis of  $Er:Y_2O_3$  nanoparticles. The first route uses ammonium bicarbonate (AHC) as the precipitating reagent to obtain yttrium carbonate precursor, whereas the second approach involves ammonium hydroxide ( $NH_4OH$ ) to precipitate yttrium hydroxide precursor. Two separate batches of 0.25 M parent solution were prepared for each precipitation route, by dissolving yttrium nitrate hexahydrate (99.9% purity, Acros Organics, Fair Lawn, NJ) and erbium nitrate pentahydrate (99.9% purity, Acros Organics, Fair Lawn, NJ) in 200 ml ultra-pure water. The  $[Er^{+3}]/[Y^{+3}]$  concentration was fixed at 0.25 mol%. In order to precipitate the yttrium carbonate precursor, a 0.25 M, 200 ml ammonium bicarbonate (99.5% purity, Fluka, St. Lois, MO) solution was added into one of the parent solution batches, whereas yttrium hydroxide precipitation involved adding 45 ml of ammonium hydroxide (28.9 % purity, Fisher Scientific, Fair Lawn, NJ) into the other batch.

Both batches were aged for 24 h at room temperature. The yttrium carbonate and hydroxide precursors were recovered by centrifuging and washed several times with ultra-pure water followed by ethanol to remove the by-products. After the final washing step, the precursors were dried under vacuum, at 60°C over-night.

Calcination of the precursors was performed at 900°C at a heating rate of 30°C/min and held for a dwell time of 2h. Powders synthesized through ammonium bicarbonate were given additional

calcination treatments at 1000°C and 1100°C. All calcination treatments were performed under oxygen, flowing at 3L/min.

#### *Powder Synthesis: Combustion Synthesis*

The combustion synthesis of 0.25 mol% Er:Y<sub>2</sub>O<sub>3</sub> utilized yttrium nitrate hexahydrate (99.9% purity, Acros Organics, Fair Lawn, NJ), erbium nitrate pentahydrate (99 % purity, Acros Organics, Fair Lawn, NJ) and glycine (99.9% purity, Sigma Aldrich, St. Lois, MO). These precursors were dissolved in distilled water at a constant glycine-to-nitrate ratio of 1:1. The solution was heated at 500°C for an hour and then cooled down to room temperature. The resultant particles were either crushed by mortar and pestle and then calcined at 900°C for 4h or were dispersed in a 5 mol% ammonium sulfate (99.99% purity, Sigma Aldrich, St. Lois, MO) solution under mild stirring for 10 minutes. Following dispersion in the ammonium sulfate solution, particles were separated using centrifuge and dried in a vacuum oven at 60°C, overnight and subsequently calcined at 900°C for 4 h.

#### *Powder Characterization*

Phase evolution of the Er:Y<sub>2</sub>O<sub>3</sub> powders were investigated by Fourier transform infrared spectroscopy (FTIR), x-ray diffraction (XRD), Brunauer-Emmet-Teller (BET), conventional (TEM) and high resolution (HR-TEM) transmission electron microscopy. All the measurements were performed at room temperature (~20°C) except for BET as described below. The FTIR spectra were measured using a Fourier transform infrared spectrometer (Model Nicolet 6700, Thermo Scientific), over the 500-4000 cm<sup>-1</sup> wave number region with a resolution of 2 cm<sup>-1</sup>. X-ray diffraction patterns were collected with a  $\theta$ - 2 $\theta$  diffractometer ( Model XDS-2000, Scintag) using a Li-doped Si detector utilizing Cu-K $\alpha$  radiation, operating at 40 kV and 30 mA. The effect of synthesis technique on the specific surface area (S<sub>p</sub>) of the calcined powders was investigated using the standard Brunauer-Emmet-Teller (BET) technique with nitrogen (N<sub>2</sub>) adsorption at approximately 195°C, using an automatic surface area analyzer (Model ASAP 2010, Micromeritics). Microstructural characterization of the powders was performed using a conventional (TEM) and high resolution (HR-TEM) transmission electron microscopy. TEM (Model 7600, Hitachi Instruments) was operated at 120 kV, whereas HR-TEM (Model 9500, Hitachi Instruments) was operated at 300 kV. TEM samples were prepared by diluting yttria powder (0.05g) in 30 ml methanol. The suspension was sonicated for 15 minutes in order to de-agglomerate the powders. One drop of this solution was placed on a copper grid for further microscopic examination.

#### *Sintering Er:Y<sub>2</sub>O<sub>3</sub> powders*

After calcination, the Er:Y<sub>2</sub>O<sub>3</sub> nanopowders were uniaxially compacted into pellets in a 13 mm diameter steel die at 10 MPa. The pellets were then pressed isostatically at 200 MPa for 6 min. using a cold isostatic press ( Model 3-12-60 C, American Isostatic Press). The pellets were sintered isothermally at 1700°C for 4 h using a vertical tube furnace (Model CTF 18/300, Carbolite) under vacuum (~10<sup>-5</sup> Pa). Finally, the density of the sintered pellets were measured using the Archimedes principle. In this paper the relative density is defined as the ratio of the experimentally measured density of sintered Er:Y<sub>2</sub>O<sub>3</sub> pellets to the theoretical density of Er:Y<sub>2</sub>O<sub>3</sub> (5.01 g/cm<sup>3</sup>).

## **Results and Discussion**

### 3.1. Precursor Composition

The influence of the fabrication method on the precursor composition was examined using FTIR spectroscopy and XRD analysis. Figure 1a provides the FTIR spectrum of the carbonate derived powder in the mid-infrared region (500-4000  $\text{cm}^{-1}$ ). Observed are peaks relating to carbonate ( $\text{CO}_3^{2-}$ ) species and water. The peaks at 1502  $\text{cm}^{-1}$  and 1416  $\text{cm}^{-1}$  correspond to the  $\nu_3$  asymmetric and symmetric stretching of the  $\text{CO}_3^{2-}$  group, respectively, and confirms the presence of  $\text{CO}_3^{2-}$  ions in the yttrium precursor [14]. Additional evidence of carbonate is found within the region below 1100  $\text{cm}^{-1}$  where the peaks at about 1095  $\text{cm}^{-1}$  and 844  $\text{cm}^{-1}$  are assignable to the  $\nu_1$  symmetric stretching mode and  $\nu_2$  out-of-plane deformation mode of  $\text{CO}_3^{2-}$ , respectively. Furthermore, the bands between 800  $\text{cm}^{-1}$  and 650  $\text{cm}^{-1}$  are due to the out-of-plane  $\nu_4$  deformation of  $\text{CO}_3^{2-}$  [15].

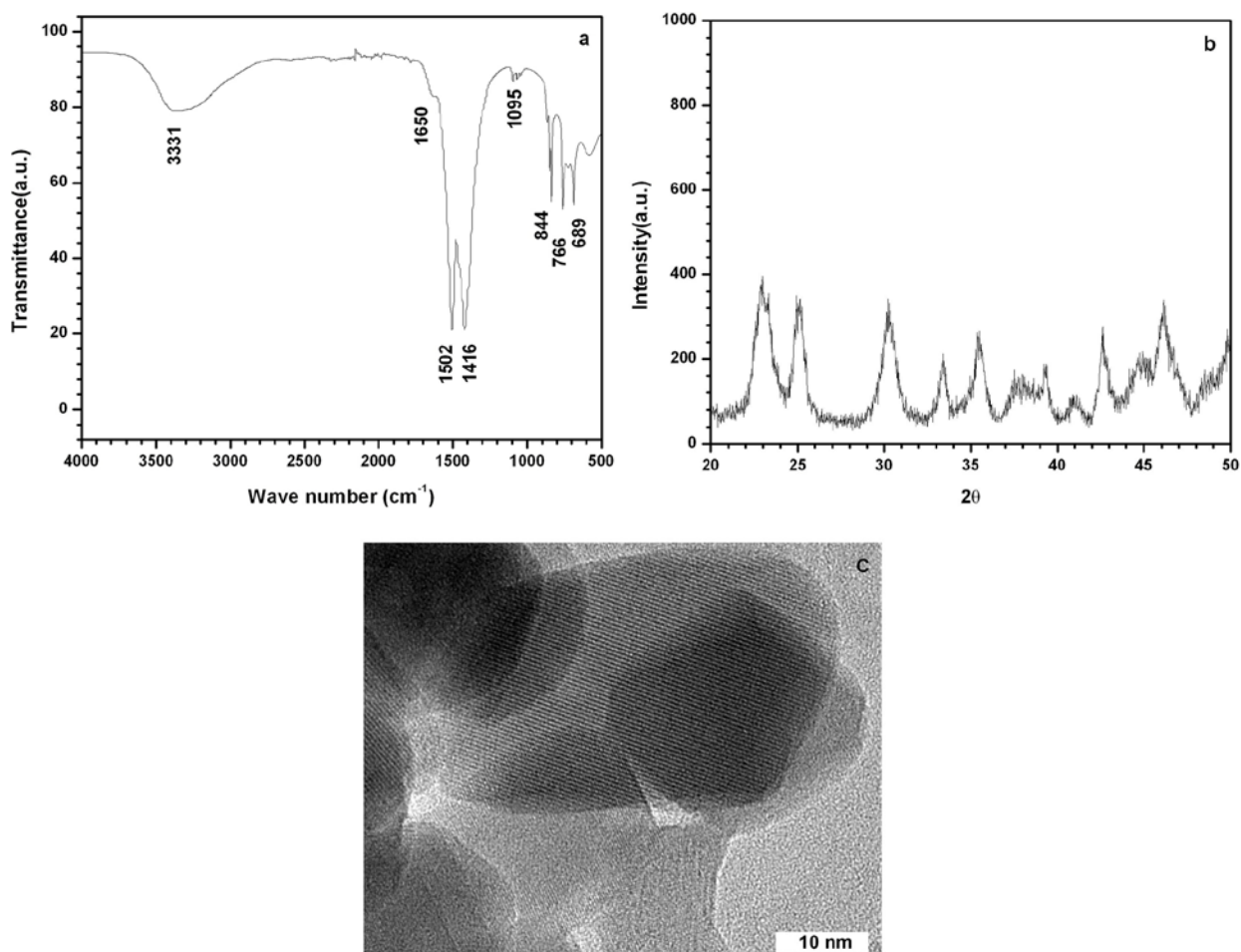


**Figure 1. Yttrium carbonate hydrate ( $\text{Y}_2(\text{CO}_3)_3(\text{H}_2\text{O})_2$ ) synthesized using ammonium hydrogen carbonate (AHC) reagent. a) FTIR spectrum b) XRD pattern (JCPDS card number of  $\text{Y}_2(\text{CO}_3)_3(\text{H}_2\text{O})_2$  is 81-1538; ref. 16 and c) HR-TEM micrograph.**

The FTIR spectrum also exhibits a broad absorption band over the range 3000-3500  $\text{cm}^{-1}$ , with greatest intensity occurring at 3331  $\text{cm}^{-1}$  and a less intense absorption at 1650  $\text{cm}^{-1}$ . The broad peak can be attributed to the OH stretching frequency, whereas the OH bending frequency at 1650  $\text{cm}^{-1}$  is very weak and appears as a shoulder on the left hand side of the  $\text{CO}_3^{2-}$  asymmetric stretching band [11].

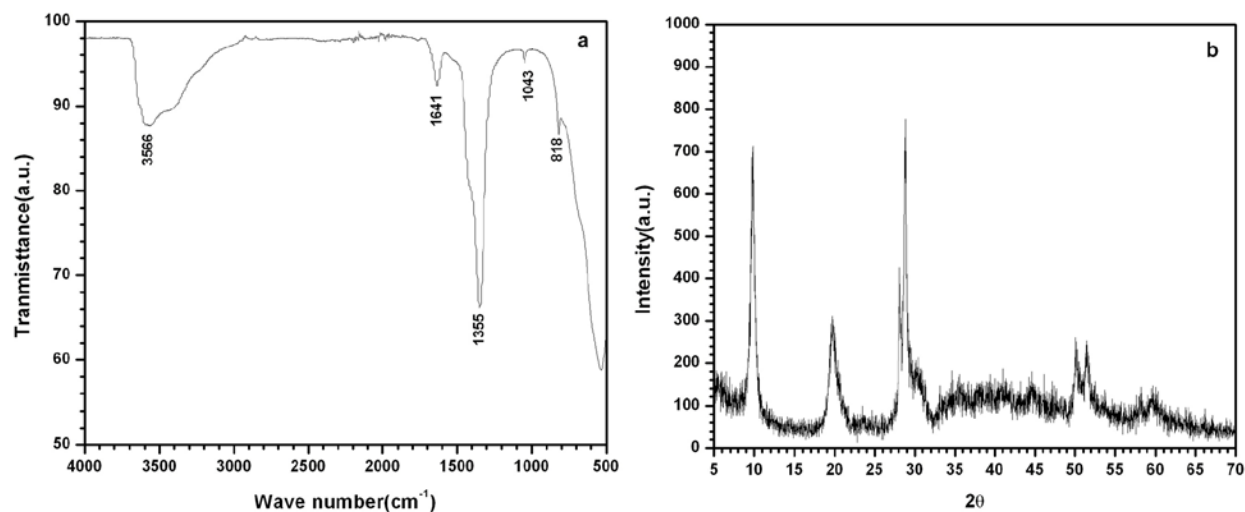


**Figure 2. Yttrium nitrate hydroxide hydrate ( $\text{Y}_2(\text{OH})_{5.14}(\text{NO}_3)_{0.86} \cdot n\text{H}_2\text{O}$ ) synthesized using ammonia water ( $\text{NH}_4\text{OH}$ ) reagent. a) FTIR spectrum b) XRD pattern (JCPDS card number of the  $\text{Y}_2(\text{OH})_{5.14}(\text{NO}_3)_{0.86} \cdot n\text{H}_2\text{O}$  is 32-1435; Ref.[18].**

The chemical phase of the yttrium carbonate precursor, as identified using XRD, is nominally yttrium carbonate hydrate ( $\text{Y}_2(\text{CO}_3)_3(\text{H}_2\text{O})_2$ ), [16] as shown in Figure 1b. The XRD pattern indicates that yttrium carbonate precursor has partially crystallized. The semi-crystalline nature of the yttrium carbonate precursor was also verified using high resolution transmission electron microscope (HR-TEM) and by observing lattice fringes associated with particles, Figure 1c. The FTIR spectrum of yttrium precursor synthesized using ammonium hydroxide ( $\text{NH}_4\text{OH}$ ) is shown in Figure 2a. The presence of OH groups in the precursor was confirmed by the peaks in the region 3000-3600  $\text{cm}^{-1}$  and at 1641  $\text{cm}^{-1}$ , which can be assigned to OH stretching and bending vibration modes, respectively. Evidence for nitrate ( $\text{NO}_3^-$ ) formation can be found at 1350  $\text{cm}^{-1}$  and presence  $\nu_1$  symmetric stretching mode of  $\text{CO}_3^{2-}$  at 1043  $\text{cm}^{-1}$  indicates that the yttrium precursor had come in contact to carbon dioxide ( $\text{CO}_2$ ) during preparation. It is well known that, yttrium hydroxide, like other lanthanides, can absorb  $\text{CO}_2$  from the atmosphere during precursor drying and/or exposure of dried powder to the air [11,17].

The XRD analysis helped to verify that the hydroxide -derived precursor is a hydrated yttrium hydroxyl-nitrate with chemical formula  $\text{Y}_2(\text{OH})_{5.14}(\text{NO}_3)_{0.86} \cdot n\text{H}_2\text{O}$  (see Figure 2b)[18]. The FTIR spectrum of the combustion synthesis -derived nanoparticles is shown in Figure 3a. The characteristic absorption bands of the  $\text{CO}_3^{2-}$  can again be observed at 1493  $\text{cm}^{-1}$ , 1407  $\text{cm}^{-1}$ , 1078  $\text{cm}^{-1}$  and 844  $\text{cm}^{-1}$ . The split frequency peaks of the  $\nu_3$  asymmetric and symmetric

stretching vibration of the  $\text{CO}_3^{-2}$  group is clearly visible at  $1505\text{ cm}^{-1}$  and  $1420\text{ cm}^{-1}$ , as well as the  $\nu_1$  symmetric stretching mode and at  $1078\text{ cm}^{-1}$  and  $\nu_2$  out of plane deformation mode at  $844\text{ cm}^{-1}$ . Furthermore, broad transmittance peak corresponding to the absorbed water is present over the range  $3000\text{--}3500\text{ cm}^{-1}$ .

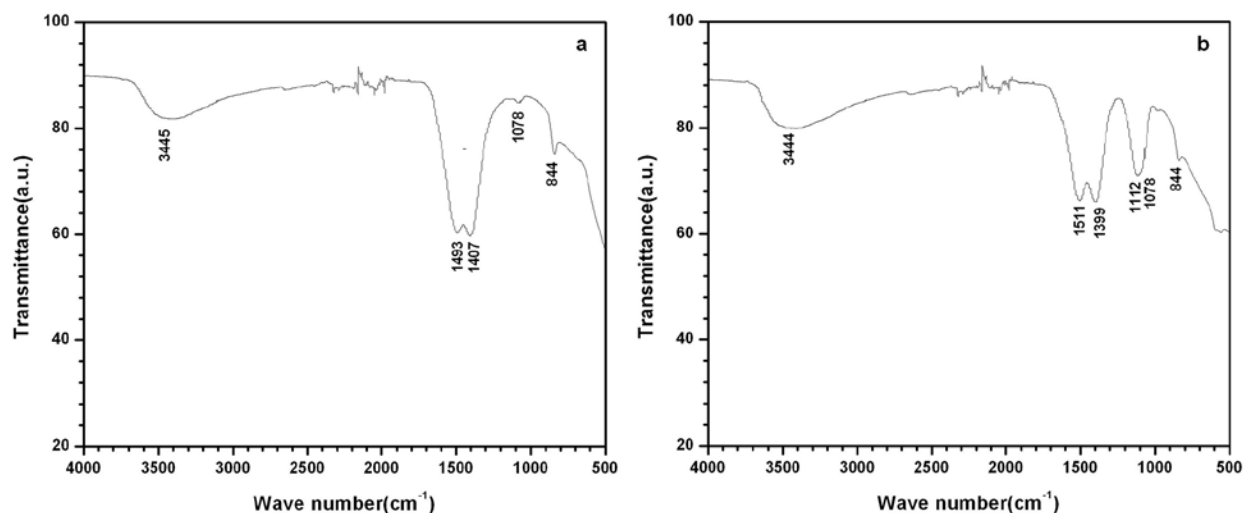


**Figure 3. FTIR spectrum of combustion synthesized yttrium precursors. Combustion synthesis was performed a) without sulfate ions and b) with sulfate ions.**

The influence of adding sulfate ions ( $\text{SO}_4^{-2}$ ) to the initial solution on the resultant phase of the yttrium precursor is shown in Figure 3b. In addition to the aforementioned molecular water and carbonate groups, the FTIR spectrum of the precursor displays an extra peak at around  $1100\text{ cm}^{-1}$  which is associated with ionic sulfate,  $\text{SO}_4^{-2}$  [19]. The combustion synthesized precursors exhibited identical x-ray diffraction patterns independent of doping history as, shown in Figure 4. The XRD peaks of these precursors are consistent with that of cubic yttrium oxide [20]. Furthermore, the broad XRD peaks and high back ground of the diffraction spectrum indicates that precursors have poor crystallinity.

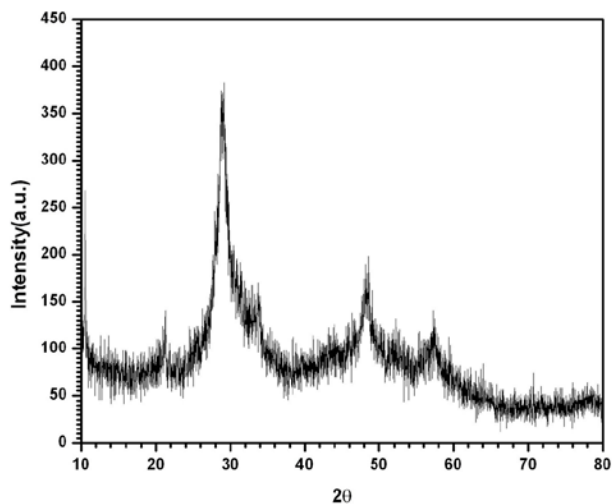


**Figure 4. XRD patterns of combustion synthesized yttrium precursors (JCPDS card number of  $Y_2O_3$  is 89-5591; ref. [20]).**

### *Calcined Powders*

Yttrium precursors, synthesized using different fabrication methods, were calcined at  $900^\circ\text{C}$  in order to obtain highly crystalline yttrium oxide powders. The XRD patterns of the calcined powders, given in Fig. 5, are consistent with cubic  $Y_2O_3$ , [20] indicating that, independent of the synthesis route,  $900^\circ\text{C}$  is sufficient to convert yttrium precursors into crystalline  $Y_2O_3$ . The x-ray peaks of the  $Y_2O_3$  powders fabricated through combustion synthesis with the addition of sulfate ions (Figure 5a) appear to be broader in comparison to those of the combustion synthesized  $Y_2O_3$  without sulfate ions (Figure 5b), as well as the solution precipitated  $Y_2O_3$  powders (Figures 5c and d) which suggests a lesser degree of crystallinity.

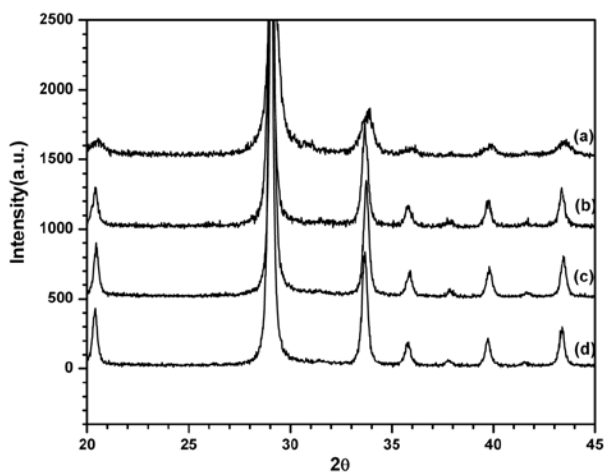


**Figure 5. XRD patterns of  $Y_2O_3$  powders calcined at  $900^\circ\text{C}$ . The powders were synthesized using a) combustion synthesis (with sulfate ions) b) combustion synthesis c) solution precipitation (AHC) d) solution precipitation ( $NH_4OH$ ).**

The effect of the addition of a small amount ammonium sulfate during combustion synthesis on the degree of crystallinity can be understood by considering the resultant particle size and the level of agglomeration of calcined  $Y_2O_3$  nanoparticles. Figures 6a and b compare the TEM micrographs of combustion-synthesized  $Y_2O_3$  powders with and without the addition of sulfate ions. As is evidenced by these micrographs, the sulfate doped particles are spherical, well-dispersed and generally smaller particles when compared to the relatively larger and rather agglomerated particles synthesized without ammonium sulfate.

$Y_2O_3$  crystals that were synthesized from yttrium carbonate precursor are pseudo-spherical in shape and loosely agglomerated powders, as shown in Figure 6c. However, these particles grow and develop into well-defined crystals during calcination. Finally, the platelet-like morphology of  $Y_2O_3$  particles synthesized using ammonium hydroxide reagent, given in Figure 6d, is consistent with the anisotropic growth behavior of yttrium hydroxy-nitrates. As shown by Voigt, the yttrium hydroxide precursors are layered structures and grow more rapidly in the direction perpendicular to the plane of layers and result in the platelet-like morphology [21].

The BET analysis, given in Figure 7, further supports the fact that the sulfate doping decreases the particles size, as a result the surface area of  $Y_2O_3$  particles increase from  $19.35 \text{ m}^2/\text{g}$  to  $43.12 \text{ m}^2/\text{g}$ ; corroborating the TEM observations.  $Y_2O_3$  particles in deionized water solutions with pH levels smaller than 8.5 have a positive zeta potential [22]. Since the diluted solution of  $Y_2O_3$  in deionized water considered in this study had a pH of 6.9, one may expect the  $SO_4^{-2}$  ions to adsorb onto the surface of  $Y_2O_3$  particles. Figure 8 provides a measure of the  $SO_4^{-2}$  ion concentration in the combustion synthesized and calcined  $Y_2O_3$  powder. The  $SO_4^{-2}$  peak at  $1100 \text{ cm}^{-1}$  can be observed in the FTIR spectrum of  $Y_2O_3$  combustion synthesized using sulfate ions (see Figure 8b). The presence of  $SO_4^{-2}$  at these high temperatures is expected to reduce diffusion between neighboring particles during calcination and result in smaller particle size and better dispersion. Moreover, TEM observations suggest that, these  $SO_4^{-2}$  ions tend to decrease the anisotropy of the surfaces, hence eliminate unequal growth rates along different crystallographic directions during calcination and generate spherical particles.

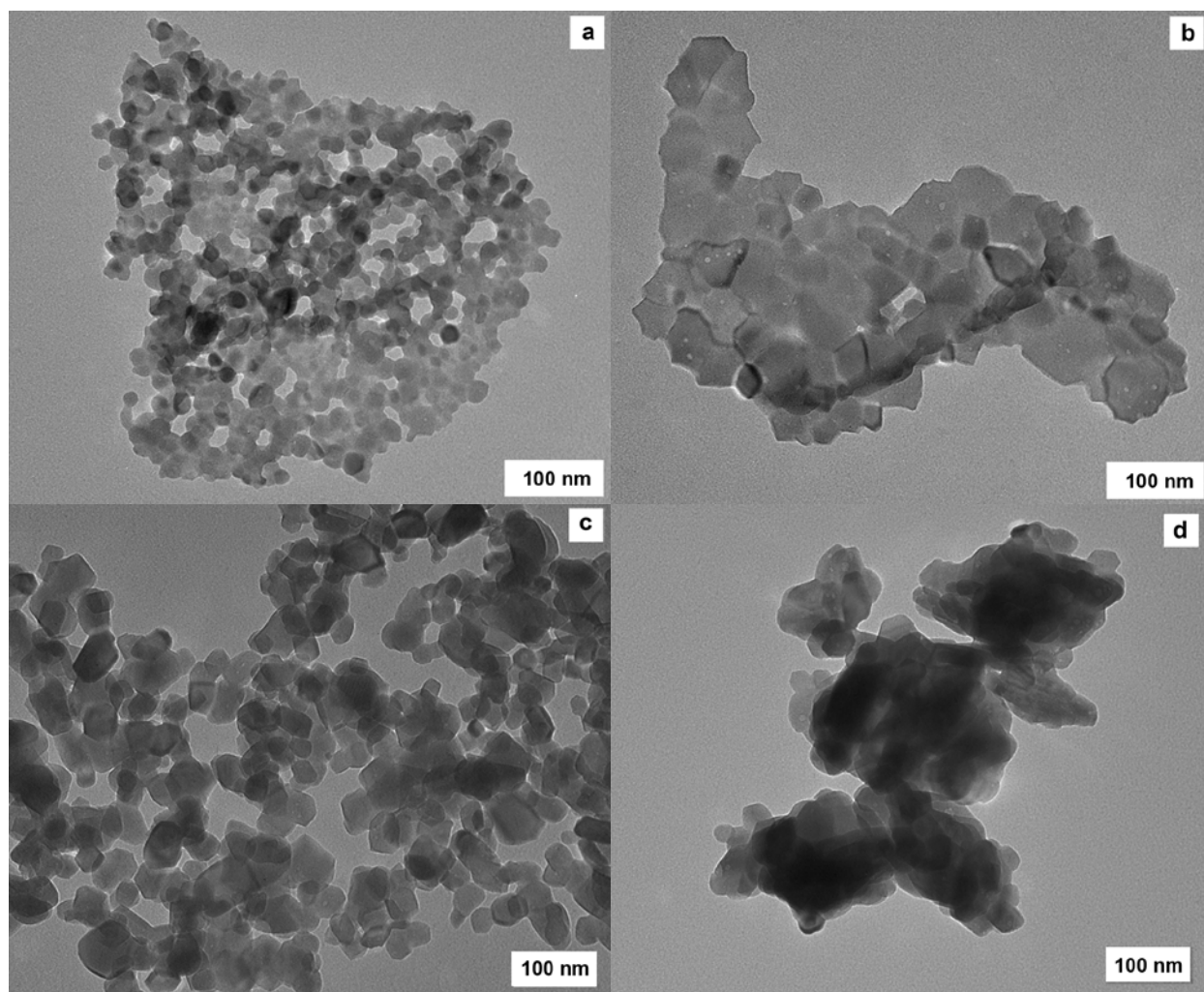


**Figure 6.** TEM micrographs of  $Y_2O_3$  powders calcined at  $900^\circ\text{C}$  and synthesized using a) combustion synthesis (with sulfate ions), b) combustion synthesis, c) solution precipitation (AHC) d) solution precipitation ( $NH_4OH$ ).

Furthermore, it was found through BET analysis that carbonate derived  $Y_2O_3$  powders, calcined at  $900^\circ C$ , have a relatively high surface area ( $S_p=24.04 \text{ m}^2/\text{g}$ ) when compared to combustion synthesized  $Y_2O_3$  powders without any sulfate addition ( $S_p=19.35 \text{ m}^2/\text{g}$ ) and the powders synthesized using ammonium hydroxide ( $S_p=18.34 \text{ m}^2/\text{g}$ ). The rapid preferential growth of along a specific crystallographic direction and severe agglomeration appears to be responsible for the lowest measured surface area of the powders synthesized using ammonium hydroxide. Nevertheless, the combustion synthesized, sulfate doped powders exhibited the highest surface area when compared to solution precipitated, as well as the combustion synthesized un-doped  $Y_2O_3$ . Higher surface area, thus the smaller particle size of these nanopowders may be accounted for the decreased low observed during XRD analysis.

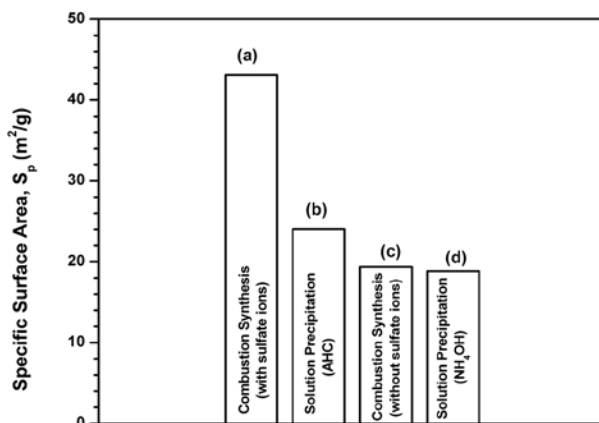


**Figure 7. BET surface area measurements of  $Y_2O_3$  powders calcined at  $900^\circ C$  and synthesized using a) combustion synthesis (with sulfate ions) b) solution precipitation (AHC) c) combustion synthesis d) solution precipitation ( $\text{NH}_4\text{OH}$ ).**

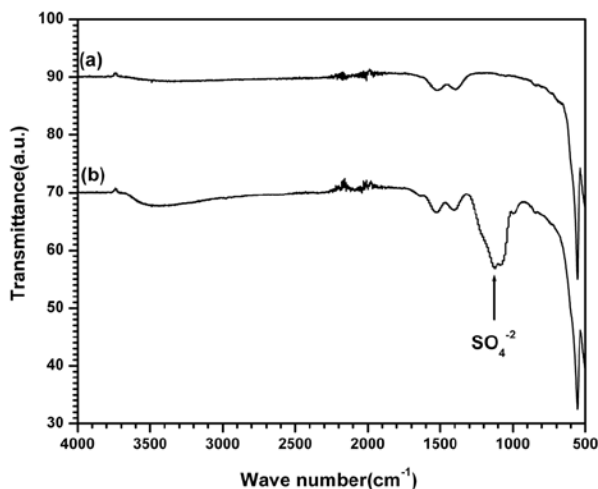


**Figure 8. FTIR spectrum of combustion synthesized  $Y_2O_3$  powders calcined at  $900^\circ C$ . Combustion synthesis was performed a) without sulfate ions and b) with sulfate ions.**

Finally, in order to understand the effect of calcination temperature on the morphology and surface area of the powders, in addition to  $900^\circ C$ , the carbonate-derived  $Y_2O_3$  particles were calcined at  $1000$  and  $1100^\circ C$  and the resultant powder characteristics were compared using TEM and BET analysis. Crystal growth with increasing calcination temperature was evidenced from the transmission electron micrographs of the powders calcined at  $1000$  and  $1100^\circ C$  given in Figures 9a and b, respectively. Upon examining these micrographs it can be concluded that the microstructural evolution of the  $Y_2O_3$  nanoparticles with increasing calcining temperature can be explained by an Oswald ripening process where larger particles grow at the expense of smaller ones. The Oswald ripening is expected to decrease the overall surface area, corroborated by the BET measurements, shown in Figure 10, and total surface energy because the particle growth is accompanied by the aggregation of neighboring particles into larger particles.

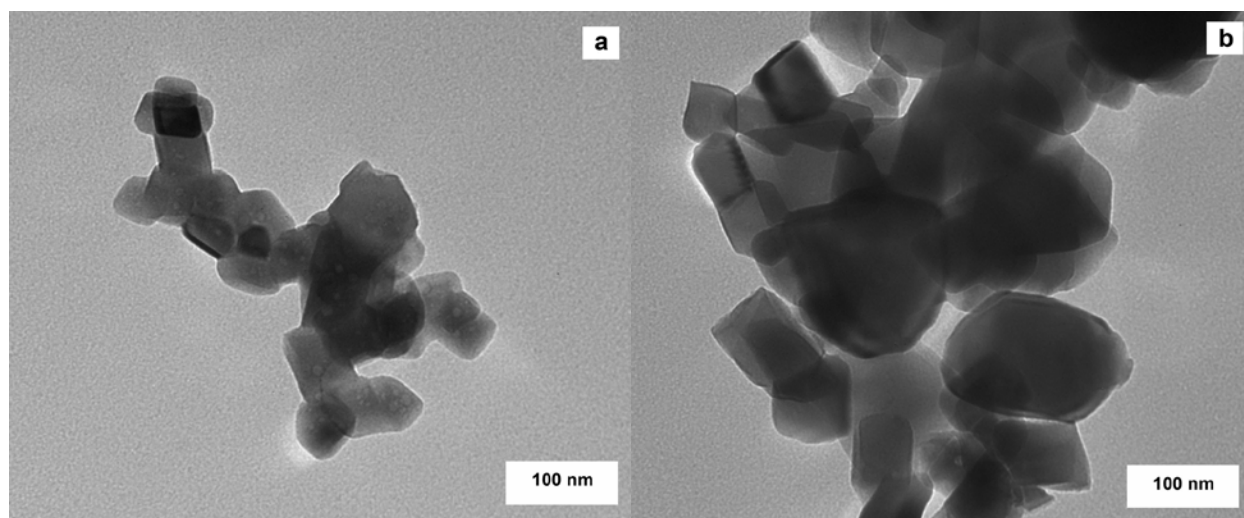


**Figure 9. TEM micrographs of the AHC derived  $Y_2O_3$  powders calcined at a)  $1000^\circ C$  and b)  $1100^\circ C$ .**

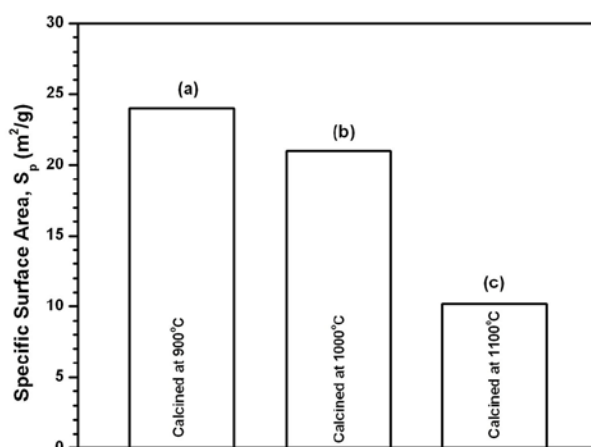


**Figure 10.** BET surface area measurements of the AHC derived  $Y_2O_3$  powders calcined at a)  $900^\circ C$ , b)  $1000^\circ C$  and c)  $1100^\circ C$ .

#### *Surface Activity of the Calcined Powders*

The FTIR spectra of the  $Y_2O_3$  nanoparticles calcined at  $900^\circ C$  confirmed the existence of the characteristic vibration of Y-O bond at approximately  $560\text{ cm}^{-1}$ , shown in Figure 11. In addition to  $Y_2O_3$  formation, the FTIR spectra, independent of the synthesizing approach, show evidence of adsorbed water (broad band over  $3650\text{--}3000\text{ cm}^{-1}$ ) as well as carbonate formation (split peak at  $1537\text{ cm}^{-1}$  and  $1434\text{ cm}^{-1}$ ), as indicated by the characteristic peaks of each molecular group.

The intensity of the peaks, observed in the FTIR spectrum, relative to the background transmission, can be used for a semi-quantitative analysis of the remnant carbonate and adsorbed OH. The differing intensities of the peaks corresponding to the  $CO_3^{2-}$  and OH groups suggest that carbonate and adsorbed OH levels in the powders depends on the synthesizing route. It should be noted that the FTIR spectrums given in Figure 11 are off-set from one another, thus the intensity of the peaks do not reflect the actual percent transmittance but rather are in arbitrary units. The combustion synthesized and sulfate doped  $Y_2O_3$  powder exhibits the highest amount of carbonate and hydroxyl indicating that  $Y_2O_3$  powders fabricated in this manner contain the maximum carbonate and water amounts. The carbonate and hydroxyl peaks associated with the  $Y_2O_3$  powders precipitated using  $NH_4OH$  have the smallest intensity and indicates the smallest carbonate and water amounts.

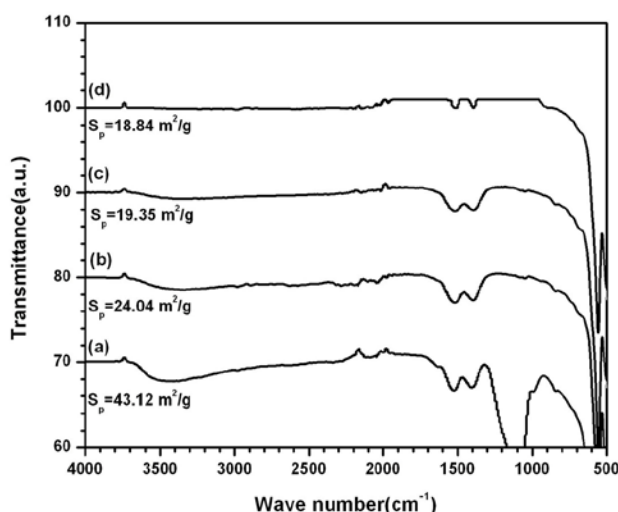


**Figure 11.** FTIR spectrum of  $Y_2O_3$  powders calcined at  $900^\circ C$ . Powders were synthesized using a) combustion synthesis (with sulfate ions), b) solution precipitation (AHC), c) combustion synthesis, d) solution precipitation ( $NH_4OH$ ). The intensity of the hydroxyl and carbonate peaks decreases from a to d. The specific surface area ( $S_p$ ) of  $Y_2O_3$  fabricated through different synthesis approaches are also given on the figure.

In order to examine the influence of calcination temperature on the remnant carbonate and adsorbed water, AHC derived  $Y_2O_3$  powders calcined at  $900$ ,  $1000$  and  $1100^\circ C$  were examined using FTIR and the results of this analysis is given in Figure 12. This figure indicates that, the relative intensities of the peaks corresponding to  $CO_3^{2-}$  and OH groups are temperature dependent and decreases with increasing calcination temperature.

Interestingly, the FTIR analysis of the  $Y_2O_3$  powders synthesized through different methods, as well as that of the AHC derived powders calcined at different temperatures showed that, the calcined powders with the greatest carbonate and hydroxyl stretching also have to the highest surface area and the intensity of carbonate and hydroxyl peaks decreases with decreasing surface area.

The hydrated yttrium carbonate decomposes at relatively low temperatures, typically below  $700^\circ C$  [23]. It is believed that the  $H_2O$  and  $CO_3^{-2}$  groups observed in the FTIR data arise from  $H_2O$  and  $CO_2$  adsorption from the air during various stages of handling. Moreover, varying quantities of  $H_2O$  and  $CO_3^{-2}$  on the particle surfaces demonstrate that the surface activity of the particles depends on the fabrication history; particles with higher surface area being more susceptible to  $H_2O$  and  $CO_2$  absorption when exposed to air.

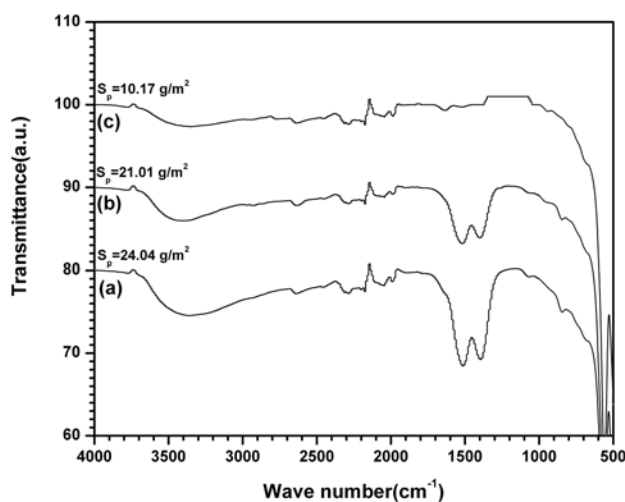


**Figure 12.** FTIR spectrum of the AHC derived  $Y_2O_3$  powders calcined at a)  $900^\circ C$  b)  $1000^\circ C$  and c)  $1100^\circ C$ .

#### *Sinterability of the $Y_2O_3$ powders*

The calcined  $Y_2O_3$  powders were compacted into pellets and sintered at  $1700^\circ C$  for 4 h under vacuum in order to examine the influence of the tradeoff between increasing surface area and respectively increasing gas absorption of the  $Y_2O_3$  starting powders on their final density. The relative density of the  $Y_2O_3$  samples is plotted as a function of relative gas absorption, as well as surface area, as shown in Figure 13. A qualitative measure of the amount gas absorption on the  $Y_2O_3$  nanoparticles after calcination is given using numbers from one through four. These numbers correspond to the relative intensities of  $CO_3^{-2}$  and  $H_2O$  peaks observed during the FTIR analysis, one representing the lowest amount of gas absorption and four representing the highest amount. Figure 13 shows that the relative density of the  $Y_2O_3$  particles increased with increasing surface area. Although this condition also results in a higher gas adsorption, increasing gas adsorption on the particle surfaces was not associated with the lower density. On the contrary, the  $Y_2O_3$  particles which exhibited the smallest gas adsorption also had the lowest sintered density. Whereas  $Y_2O_3$  powders fabricated by combustion synthesis with the addition of sulfate ions showed the highest sinterability with a relative density of about 97%. The particles

fabricated using this method had the highest surface area and highest gas absorption after calcination.

### Section Conclusions

Two different powder synthesis methods, solution precipitation and combustion synthesis, were used to fabricate erbium-doped yttria ( $\text{Er:Y}_2\text{O}_3$ ) nanoparticles. Yttrium carbonate or yttrium hydroxide can be obtained as a precursor through solution precipitation depending on the precipitating reagent whereas phase-pure, cubic  $\text{Y}_2\text{O}_3$  is obtained through combustion synthesis.  $\text{Er:Y}_2\text{O}_3$  nanoparticles synthesized from yttrium hydroxide precursors and from precursors obtained through combustion synthesis are agglomerated and have lower surface area. Agglomeration, particle size, and crystallinity of the combustion synthesized  $\text{Er:Y}_2\text{O}_3$  particles can be reduced by addition of a small amount of ammonium sulfate.

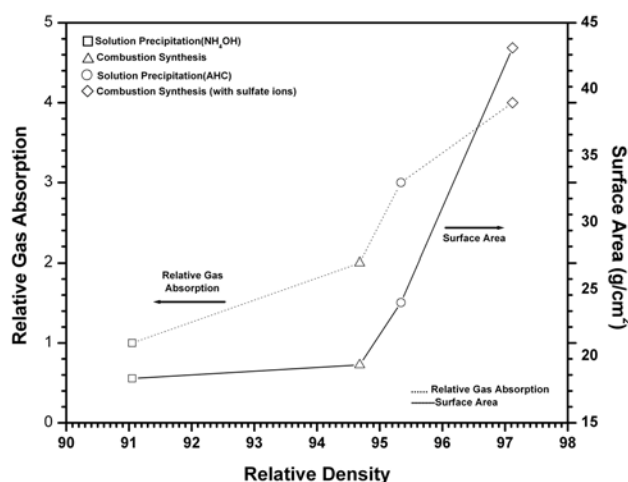


**Figure 13. Relative density of the sintered  $\text{Y}_2\text{O}_3$  nanopowders as a function of gas absorption and surface area of the starting powders. The powders were synthesized using solution precipitation ( $\text{NH}_4\text{OH}$ ; □), combustion synthesis ( $\Delta$ ), Solution precipitation (AHC; o) and combustion synthesis (with sulfate ions;  $\diamond$ )**

The high surface area achieved through the addition of ammonium sulfate indicates a higher degree of powder sinterability. However, FTIR analysis indicated that calcined  $\text{Er:Y}_2\text{O}_3$  particles absorb carbon dioxide and water when exposed to air and the amount of  $\text{CO}_2$  and  $\text{H}_2\text{O}$  adsorption depends on the surface area, with the increasing surface area being associated with increasing  $\text{CO}_2$  and  $\text{H}_2\text{O}$  absorption on the nanoparticle surfaces. Although, both  $\text{CO}_2$  and  $\text{H}_2\text{O}$  are expected to evolve as gases during sintering of these nano-sized oxides and result in porosity within the sintered ceramic, the release of extensive amount of  $\text{CO}_2$  and  $\text{H}_2\text{O}$  gases during sintering do not degrade the benefit of increased powder sinterability due to increased surface area. Our results indicate that the condition for obtaining a high relative density after sintering is using  $\text{Y}_2\text{O}_3$  particles with a large surface area. Although, this condition also increases the amount of gas absorption on the surface of the particles, increased gas absorption does not have a detrimental influence on the sintered density. This study indicated that the most favorable synthesis powder fabrication method for achieving a high sintered density was combustion synthesis with the addition of sulfate ions.

## Section References

- 1 T. Y. Fan, D. J. Ripin, R. L. Aggarwal, J. R. Ochoa, B. Chann, M. Tilleman, and J. Spitzberg, *IEEE J. Sel. Top. Quant. Electron.*, **13** [3] 448- 59 (2007).
- 2 M. Mandel, *App. Phys. Lett.*, **2** [10] 197-98 (1963).
- 3 K. Serivalsatit, B.Y.K. Kokuoz, B. Kokuoz and J. Ballato, *Opt. Lett.* **34** [7] 1033-5 (2009).
- 4 J. Mouzon, A. Maitre, L. Frisk, N. Lehto, and M. Odén, *J. Eur. Ceram. Soc.*, **29** [2] 311-6 (2009).
- 5 H. Eilers, *J. Eur. Ceram. Soc.*, **27** [16] 4711-17 (2007).
- 6 T. Ye, Z. Guiwen, Z. Weiping, and X. Shangda, *Mater. Res. Bull.*, **32** [5] 501-6 (1997).
- 7 N. Saito, S. Matsuda, and T. Ikegami, *J. Am. Ceram. Soc.*, **81** [8] 2023-28 (1998).
- 8 L. Wen, X. Sun, Q. Lu, G. Xu, and X. Hu, *Opt. Mater.*, **29** [2-3] 239-45 (2006).
- 9 T. Ikegami, J. G. Li, and T. Mori, *J. Am. Ceram. Soc.*, **85** [7] 1725-29 (2002).
- 10 Z. Huang, X. Sun, Z. Xiu, S. Chen, and C. Tsai, *Mater. Lett.* **58** [15] 2137-42 (2004).
- 11 L. M. Seaverson, S. Q. Luo, P. L. Chen, and J. F. McClelland, *J. Am. Ceram. Soc.*, **69** [5] 423-29 (1986).
- 12 H. Gong, D. Y. Tang, H. Huang, T. S. Zhang, and J. Ma, *Matls. Chem. Phys.*, **112** [2] 423-26 (2008).
- 13 Z. Mierczyk, M. Kwanśny, K. Koczyński, A. Gietka, T. Lukasiewicz, Z. Frukacz, J. Kisielewski, R. Stepień and K. Jedrzejewski, *J. Alloys Compd.*, **300-301** 398-406 (2000).
- 14 S.D. Ross and J. Goldsmith, *Spectrochim. Acta*, **20** [5] 781-4 (1964).
- 15 A. B. Ali, M. O. Awaleh, M. Leblanc, L. S. Smiri, V. Maisonneuve, and S. Houlbert, *C.R.Chimie*, **7** [6-7] 661-8 (2004).
- 16 JCPDS card no. 81-1538, The International Centre for Diffraction Data (Newtown Square, PA, USA).
- 17 Y. Li, X. Lin, Y. Wang, J. Luo, and W. Sun, *J. Rare Earths*, **24** [1] 34-8 (2006).
- 18 Y. Li, X. Lin, Y. Wang, J. Luo, and W. Sun, *J. Rare Earths*, **24** [1] 34-8 (2006).
- 19 JCPDS card no. 32-1435, The International Centre for Diffraction Data (Newtown Square, PA, USA).
- 20 K. Nakamoto, pp. 106-15 in *Infrared Spectra of Inorganic and Coordination Compounds*, Wiley-Interscience, New York, 1970.
- 21 JCPDS card no. 89-5591, The International Centre for Diffraction Data (Newtown Square, PA, USA).
- 22 J. A. Voigt, PhD Dissertation, Iowa State University, 1986.
- 23 L. Jin, X. Mao, S. Wang, and M. Dong, *Ceram. Int.*, **35** [2] 925-27 (2009).
- 24 S. Ramanathan, M. B. Kakade, P. V. Ravindran, B. B. Kalekar, K. V. Chetty, and A. K. Tyagi, *J. Therm. Anal. Cal.*, **84** [2] 511-19 (2006).

## Section III: Synthesis, processing, and properties of sub-micron grained highly transparent yttria ceramics

### Section Summary

This section reports the fabrication of 0.3  $\mu\text{m}$  average grain sized transparent yttria ceramics by a modified two-step sintering approach. This process yielded full densification of the yttria ceramics with greatly reduced grain-growth. These transparent yttria ceramics exhibited equivalent transparency to that of single crystals in the near-infrared spectral region. The

microhardness and fracture toughness of the 0.3  $\mu\text{m}$  average grain sized transparent yttria ceramics fabricated by a modified two-step sintering were found to exceed those of  $\sim 300 \mu\text{m}$  average grain sized transparent yttria ceramics fabricated by conventional sintering by 25% and 70%, respectively.

## Introduction

For many years, rare earth doped yttria ( $\text{Y}_2\text{O}_3$ ) has been considered as a candidate host material for solid state lasers [1-3].  $\text{Y}_2\text{O}_3$  possesses a higher thermal conductivity and a lower thermal expansion than the widely used yttrium aluminum garnet (YAG), which is critical for thermal management as laser powers continue to increase and generate more heat during operation. The thermal conductivity and linear thermal expansion of  $\text{Y}_2\text{O}_3$  are about  $17 \text{ W}\cdot\text{m}^{-1}\text{K}^{-1}$  and  $6\text{-}7 \times 10^{-6} \text{ K}^{-1}$ , respectively, while those of YAG are about  $12 \text{ W}\cdot\text{m}^{-1}\text{K}^{-1}$  and  $7.8 \times 10^{-6} \text{ K}^{-1}$  [3].

However, due to the refractory nature of  $\text{Y}_2\text{O}_3$ , recent efforts have focused on transparent  $\text{Y}_2\text{O}_3$  ceramics rather than single crystals. Like YAG,  $\text{Y}_2\text{O}_3$  is a cubic crystal (Ia3d for YAG; Ia3 for  $\text{Y}_2\text{O}_3$ ) and is optically isotropic which is ideal for the fabrication of transparent ceramics.

Typically, transparent  $\text{Y}_2\text{O}_3$  ceramics are fabricated by pressure sintering (hot pressing [4] or hot isostatic pressing [5-6]), or pressureless sintering at high temperatures [7-10]. Some additives are used to enhance densification such as  $\text{ThO}_2$  [11],  $\text{La}_2\text{O}_3$  [12], and  $\text{HfO}_2$  [13]. The grain size of transparent  $\text{Y}_2\text{O}_3$  ceramics fabricated by the above methods usually is in a range tens to hundreds of micrometer due to significant grain growth at the final stage of sintering. Large-grained ceramics tend to have lower strength than smaller grained ceramics and, as a result, the large-grained ceramics are less desirable in applications demanding high thermal shock resistance such as high energy solid state lasers.

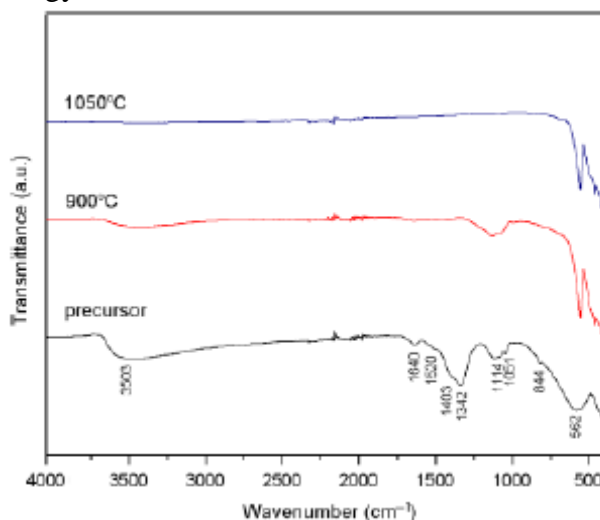


Figure 1. FTIR spectra of the precursor and calcined powder at 900° and 1050 °C.

While the strength of ceramics can be enhanced by a reduction in grain size, [14] it is difficult to produce bulk dense nano-grained ceramics because of rapid grain growth during the final stage of sintering. Chen and Wang have developed a new two-step sintering technique [15-16]. The first step entails heating the sample to a high temperature ( $T_1$ ) in order to achieve a density

greater than about 75% such that sufficient triple junctions exist throughout the sample to pin grain boundaries. In the second step, the sample then is cooled to a lower temperature ( $T_2$ ) where grain boundary diffusion is active but grain boundary migration is impeded due to this triple junction pinning. Therefore, densification continues without significant grain growth by prolonged isothermal heating at this lower temperature ( $T_2$ ). This technique has been successfully utilized for producing nano-grained  $Y_2O_3$  ceramics with grain sizes of  $<200$  nm [16]. However, from the reported densities, those  $Y_2O_3$  ceramics were not fully dense and contained small amounts of residual porosity. These pores would cause optical scattering, making the ceramics translucent and not transparent.

Our previous work reported the fabrication of sub- $\mu\text{m}$  grain-sized transparent  $Y_2O_3$  ceramics [17]. The resulting sub- $\mu\text{m}$  grained  $Y_2O_3$  ceramics exhibit optical transparency equivalent to that of single crystals at near-infrared wavelengths of practical interest. In this work, we report in detail the fabrication of sub- $\mu\text{m}$  grain-sized transparent  $Y_2O_3$  ceramics by employing a modified two-step sintering approach. The microhardness and fracture toughness of these ceramics are reported as well.

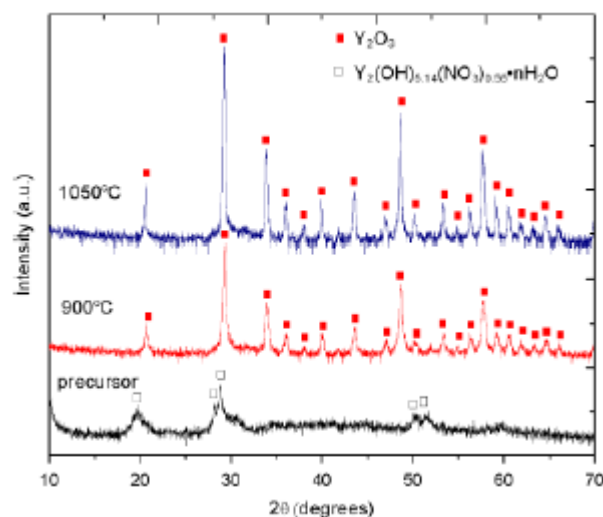


Figure 2. XRD patterns of the precursor and calcined powder at  $900^\circ$  and  $1050^\circ\text{C}$ .

## Selected Procedures

### *Powder preparation and sample compaction*

In the present study, 0.25 atom% Er doped  $Y_2O_3$  nanopowders were prepared by co-precipitation with ammonium hydroxide. A 0.25 M of erbium doped yttrium nitrate solution was prepared by dissolving yttrium nitrate hexahydrate (Acros Organics, 99.9%, Fair Lawn, NJ) and erbium nitrate pentahydrate (Acros Organics, 99.9%, Fair Lawn, NJ) in ultrapure water. A 5 mole % solution of ammonium sulfate (Sigma Aldrich, 99.99%, St. Louis, MO) was added into the nitrate solution and a 2.0 M ammonium hydroxide (Fisher Scientific, Certified A.C.S. Plus, Fair Lawn, NJ) solution was added drop-wise in order to precipitate a yttrium nitrate precursor. The precipitated precursor was aged for 3 hours at room temperature and then washed twice with ultrapure water and ethanol. After the final washing, the precipitate was dried at  $60^\circ\text{C}$  overnight

under vacuum. The dried precursor was calcined at 1050 °C for 4 hours under oxygen, flowing at 3 l/min to yield Y<sub>2</sub>O<sub>3</sub> nanopowders.

The morphology and particle size of Y<sub>2</sub>O<sub>3</sub> nanopowders were determined using transmission electron microscopy (TEM; model H7600T, Hitachi, Pleasanton, CA). The average particle size was measured by averaging approximately 200 particles from TEM images. The specific surface area of the Y<sub>2</sub>O<sub>3</sub> nanopowders was determined by the Brunauer-Emmet-Teller method (BET; model ASAP 2010, Micrometrics, Norcross, GA) with nitrogen (N<sub>2</sub>) adsorption at approximately 195°C. The equivalent particle size ( $D_{BET}$ ) could be estimated from BET surface area using

$$D_{BET} = \frac{6}{\rho \cdot S_{BET}} \quad (1)$$

where  $\rho$  is the theoretical density of Y<sub>2</sub>O<sub>3</sub>, which is 5.031 g/cm<sup>3</sup> (JCPDS card no.41-1105);  $S_{BET}$  is the specific surface area measured by BET method.

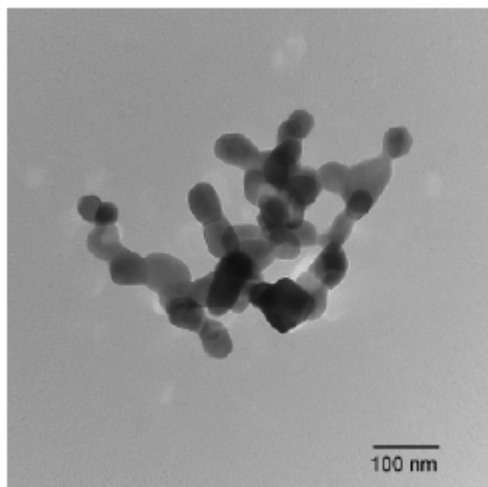


**Figure 3. Transmission electron microscopy of Er-doped Y<sub>2</sub>O<sub>3</sub> powders calcined at 1050 °C for 4 h.**

Phase identification was performed by X-ray diffractometer (XRD; XDS 2000, Scintag, Cupertino, CA) using CuK $\alpha$  with wavelength of 0.15406 nm. Infrared spectra was collected using a Fourier transformed infrared spectrometer (Nicolet 6700 FT-IR, Thermo Scientific, Waltham, MA).

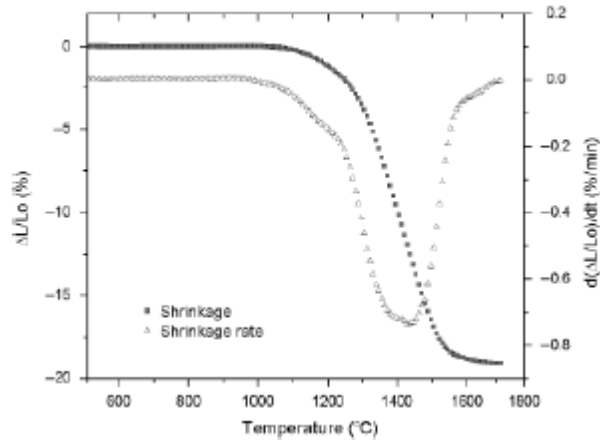


**Figure 4. Shrinkage and shrinkage rate of Er-doped  $Y_2O_3$  ceramics versus the temperature.**

The calcined powders were uniaxially pressed into pellets at approximately 15 MPa without any binding additives. After uniaxial pressing, the pellets were given an additional pressing for 5 min using a cold isostatic press (American Isostatic Press 3-12-60 C, Columbus, OH) operating at 206 MPa to obtain a green density of about 55%.

### *Sintering*

In order to study the effect of conventional sintering and two-step sintering on the microstructure of  $Y_2O_3$  ceramics, green bodies were sintered by both conventional sintering and two-step sintering under vacuum (less than  $10^{-3}$  Pa). Conventional sintering was performed at temperatures ranging from 1300 – 1600 °C in 50 °C intervals at a heating rate of 10 °C/min. After reaching the desired temperature, the furnace was cooled naturally to room temperature. For the two-step sintering, the samples were heated at a heating rate of 10 °C/min to a higher temperature ( $T_1$ ), and then cooled down at 50 °C/min to a lower temperature ( $T_2$ ) and held at  $T_2$  for 20 hours. The  $T_2$  temperature was determined from the maximum linear shrinkage rate as measured by vertical dilatometer (Linseis, Model L75, Princeton Junction, NJ). The green bodies were heated at a heating rate of 10 °C/min to 1700 °C, and then cooled down at 30 °C/min to 700 °C. After that, the furnace was cooled down naturally to room temperature.

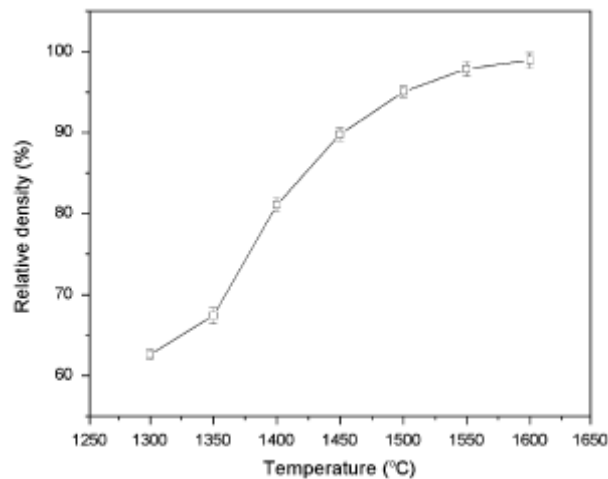


**Figure 5. The relative density of Er-doped  $Y_2O_3$  ceramics versus the sintering temperature.**

In order to obtain transparent  $Y_2O_3$  ceramics, the fully dense two-step sintered samples were subsequently hot isostatically pressed (HIP; model 6-30H, American Isostatic Press, Columbus, OH) at 1300 °C under an argon pressure of 206 MPa for 3 hours which is denoted as HIPed two-step sintering. For comparison, a Er doped  $Y_2O_3$  transparent ceramic was also prepared by conventional sintering at 2000 °C for 6 hours at a heating rate of 5 °C/min.

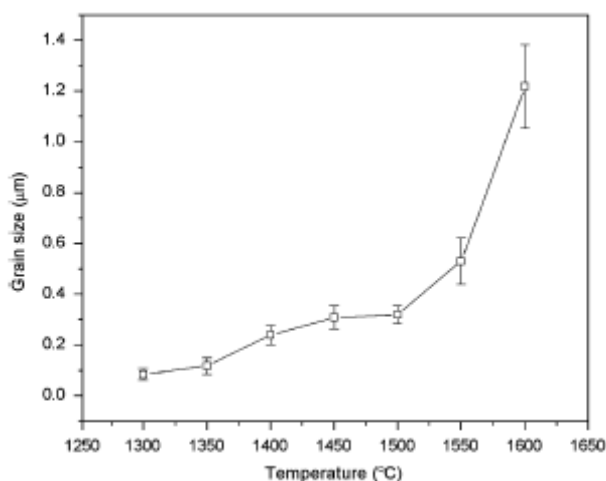


**Figure 6. The average grain size of Er-doped  $Y_2O_3$  versus the sintering temperature.**

## Results and Discussion

### *Powder characterization*

Figure 1 shows the FTIR spectra of the uncalcined and calcined  $Y_2O_3$  precursor. The FTIR spectra of uncalcined precursor exhibits a broad peak over the range from 3000-3750  $cm^{-1}$  and a peak at 1640  $cm^{-1}$ , which can be attributed to the OH stretching and OH bending frequencies, respectively. The IR absorption due to  $NO_3^-$  is observed at 1342  $cm^{-1}$ .<sup>21</sup> The presence of the  $\nu_3$  asymmetric and symmetric stretching vibrations of the  $CO_3^{2-}$  at 1520 and 1403  $cm^{-1}$ , as well as  $\nu_1$  symmetric stretching mode of  $CO_3^{2-}$  at 1051  $cm^{-1}$  and  $\nu_2$  out-of-plane deformation mode of  $CO_3^{2-}$  at 844  $cm^{-1}$  indicate the adsorption of carbon dioxide during preparation. It is well known that yttrium hydroxide can adsorb carbon dioxide from the atmosphere during precursor drying and/or storage [13,14]. The peak at around 1114  $cm^{-1}$  is associated with  $SO_4^{2-}$  [22]. The presence of  $SO_4^{2-}$  can inhibit volume diffusion and/or grain boundary diffusion which results in low agglomerated particles after calcination [23].

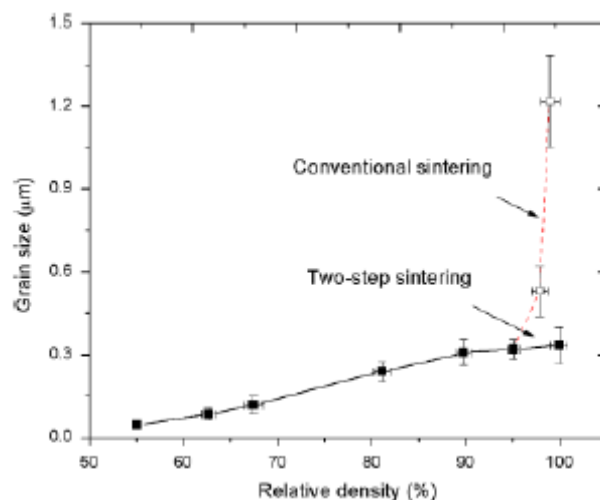


**Figure 7. Grain size and density of 0.25% Er-doped  $Y_2O_3$  in two-step sintering and conventional sintering.**

The vibrational features from molecular water, free hydroxyl groups,  $NO_3^{2-}$ , and  $SO_4^{2-}$  are no longer present upon calcination at  $1050^\circ C$ , while the Y-O vibration at  $562\text{ cm}^{-1}$  is a key indication of highly crystalline  $Y_2O_3$  [24]. The XRD patterns of uncalcined and calcined precursors are provided in Figure 2. The XRD pattern of uncalcined precursor shows the peaks of a hydrated yttrium hydroxyl nitrate with chemical formula  $Y_2(OH)_{5.14}(NO_3)_{0.86}\cdot nH_2O$  (JCPDS card no. 32-1435). After calcination at  $1050^\circ C$  for 4 hours, the yttrium precursors transform to cubic  $Y_2O_3$  (JCPDS card no. 41-1105). The morphology of the  $Y_2O_3$  nanopowders obtained by calcination at  $1050^\circ C$  for 4 hours are shown in Figure 3. The  $Y_2O_3$  nanopowders are loosely agglomerated and fairly uniform with the average particle size of  $45\pm 10\text{ nm}$ . The specific surface area of the  $Y_2O_3$  nanopowders was  $14.23\text{ m}^2/\text{g}$ . The equivalent particle size ( $D_{BET}$ ) is  $84\text{ nm}$  indicating a slight agglomeration of  $Y_2O_3$  nanopowders.

### Sintering

The densification behavior of Er doped  $Y_2O_3$  studied by dilatometry is shown in Figure 4. The onset of densification is about  $1100^\circ C$ . The linear shrinkage rate is maximal when the temperature reaches about  $1400^\circ C$ . Figure 5 shows the relative density of Er doped  $Y_2O_3$  ceramics as a function of the sintering temperature. It can be seen that the relative density of the sintered samples increases rapidly with increasing sintering temperature within the range from  $1350^\circ C$  and  $1450^\circ C$ .

The average grain size of sintered samples as a function of the sintering temperature is shown in Figure 6. The average grain size of sintered samples increases slowly with increasing sintering temperature below  $1500^\circ C$  but increases rapidly with increasing sintering temperature above  $1500^\circ C$ . The average grain size of sintered samples at  $1500^\circ C$  is about  $320\text{ nm}$ .

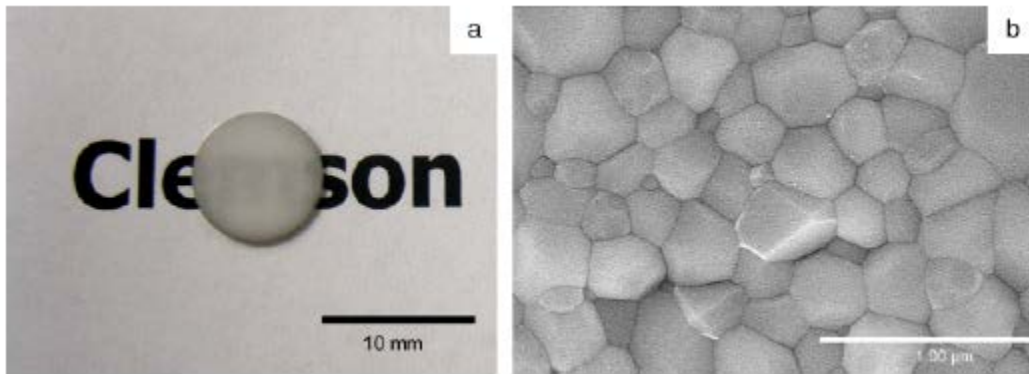


**Figure 8. (a) Optical image of the two-step-sintered Er-doped  $Y_2O_3$  ceramic. (b) Scanning electron microscopy micrograph of the two-step-sintered Er-doped  $Y_2O_3$  ceramic.**

Figure 7 shows the average grain size as a function of the relative density of sintered samples. It could be seen that the average grain size increases slowly with increasing the relative density below 95%. However, when the relative density reaches about 95%, the average grain size increases rapidly indicating the transition from the intermediate state of sintering to the final stage of sintering. In the intermediate stage of sintering, the continuous pore channels locate along the grain edges. The presence of these pores suppresses the grain growth. However, such pores channels collapse in the final stage of sintering to become isolated pores which typically results in decreasing pore pinning and triggering accelerated grain growth [25].

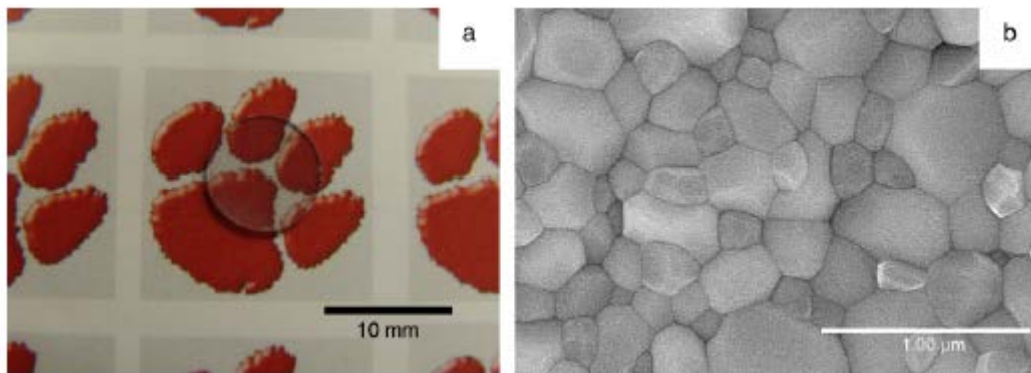


**Figure 9. (a) Optical image of the polished hot isostatically pressed (HIPed) Er-doped  $Y_2O_3$  ceramic. (b) Scanning electron microscopy micrograph of the microstructure of the HIPed Er-doped  $Y_2O_3$  ceramic.**

From above results, it could be seen that the highest densification rate occurs within a sintering temperature between 1350 °C and 1450 °C while the rapid grain growth occurs at the sintering temperature above about 1500 °C. Since the densification and grain growth occur at different temperature it is possible to obtain a fully dense ceramics without promoting grain growth [26]

In order to obtain an ultrafine grain structure while achieving a fully densified ceramic, two-step sintering was employed. The samples were heated to  $T_1$  in order to achieve an intermediate density and to render pores unstable and then cooled to  $T_2$  and isothermally held until a fully dense and transparent ceramic was obtained.

The results of Figure 6 indicated that the grain size increases rapidly above 1500 °C. Therefore,  $T_1$  should be lower than 1500 °C in order to avoid grain growth. Further, it is known from Figure 4 that the maximum linear shrinkage rate occurs at about 1400 °C; accordingly, this defines for this work the second temperature,  $T_2$ . For two-step sintering, the green compacts were heated at 1500 °C and then cooled to 1400 °C and held isothermally for 20 hours.

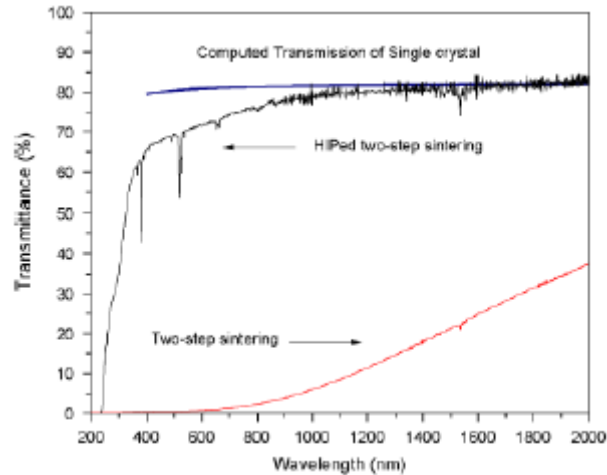


**Figure 10. Optical transmission spectra of the two-step-sintered Er:Y<sub>2</sub>O<sub>3</sub> ceramic, hot isostatically pressed two-step-sintered Er:Y<sub>2</sub>O<sub>3</sub> ceramic, and Y<sub>2</sub>O<sub>3</sub> single crystal.**

The relative density of two-step sintered Y<sub>2</sub>O<sub>3</sub> ceramics was greater than 99%. The sintered ceramic was translucent, as is shown in Figure 8(a), indicating some remnant porosity. The average grain size of two-step sintered Y<sub>2</sub>O<sub>3</sub> ceramics was 332 ± 52 nm (representative SEM image provided in Figure 8(b)). The grain size of the Er doped Y<sub>2</sub>O<sub>3</sub> samples was shown in Figure 7 to increase from the starting particle size of 45 ± 10 nm to 320 ± 35 nm during the first sintering step. During the second sintering step, the relative density of the sample increases from 95% to greater than 99% while the grain size of the sample increased only slightly from 320 ± 35 to 332 ± 52 nm.

Although the two-step sintering method can suppress the grain growth, the 20 hour sintering performed in this work showed that it cannot entirely eliminate the residual pores that deteriorate the optical transparency of the samples. Typically, a transparent Y<sub>2</sub>O<sub>3</sub> ceramic is sintered at temperature between 1700 – 2170 °C [8-12]. This high temperature sintering provides a significant driving force for eliminating residual pores. The two-step sintering conducted in this work is done at lower temperatures that seem not to provide sufficient driving force for eliminating residual pores. Therefore, in order to remove such pores, an additional driving force was applied by subsequently hot isostatically pressing sintered samples.

The hot isostatically pressing of the samples was carried out at 1300 °C in an argon pressure of 206 MPa for 3 hours. After HIPing, the translucent ceramic becomes highly transparent as shown in Figure 9(a). The average grain size of the HIPed sample is 343 ± 70 nm (Figure 9(b)). The HIPing ceramic samples at a temperature lower than  $T_2$  can eliminate the residual pores by taking advantage of the pressure-assisted densification without promoting grain growth.

Figure 10 shows the room temperature transmission spectra of the two-step sintered ceramic and the HIPed two-step sintered ceramic over the wavelength region of 200 to 2000 nm. The in-line transmittance of a  $Y_2O_3$  single crystal was computed from refractive index data reported by Nigara [20]. The transmittance of the non-HIPed two-step sintered ceramic is less than 2% in visible range (400 – 800 nm) due to scattering from residual pores in the microstructure. After HIPing, the residual pores were eliminated resulting in a significant improvement in the optical clarity. Above 1200 nm, the transmittance of the HIPed two-step sintered  $Y_2O_3$  ceramic is equivalent to that of a single crystal. The absorption peak at about 390 and 540 nm are due to the  $Er^{3+}$  dopant.

### Lasing Results on Yttria Ceramics

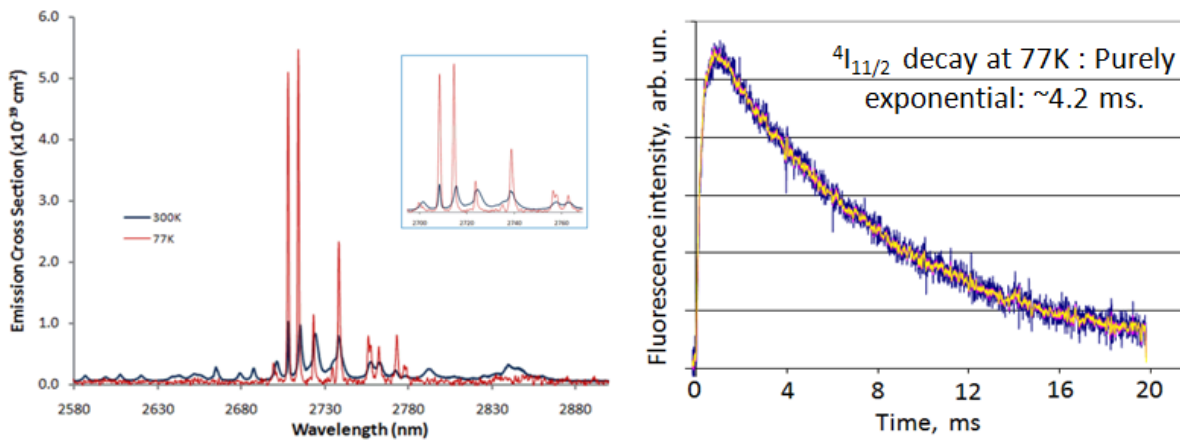


**Figure 11. (left) Emission cross-section of  $Er^{3+}:Y_2O_3$  ceramics at cryogenic and room temperatures and (right) measured radiative lifetimes at cryogenic temperatures.**

Figure 11 provides spectroscopic results on the  $Er^{3+}:Y_2O_3$  ceramics. As can be seen the  $Er^{3+}:Y_2O_3$  ceramics exhibit a ~6x increase in  $4I_{11/2} \rightarrow 4I_{13/2}$  cross section when cryo-cooled permitting lasing from less ideal samples; hence this was studied as a proof-of-concept. Regular  $\sim 1.6 \mu\text{m}$  ( $4I_{13/2} \rightarrow 4I_{15/2}$ ) emission does not enjoy such an enhanced cryo-cross-section, and due to loss figure lasing at 1599.5 nm was not achieved in these samples. As is shown below, the  $Er:Y_2O_3$  ceramics did lase at 3  $\mu\text{m}$  though the efficiency was roughly half that of the best Japanese samples; most likely due to impurity absorptions from the unpurified precursors.

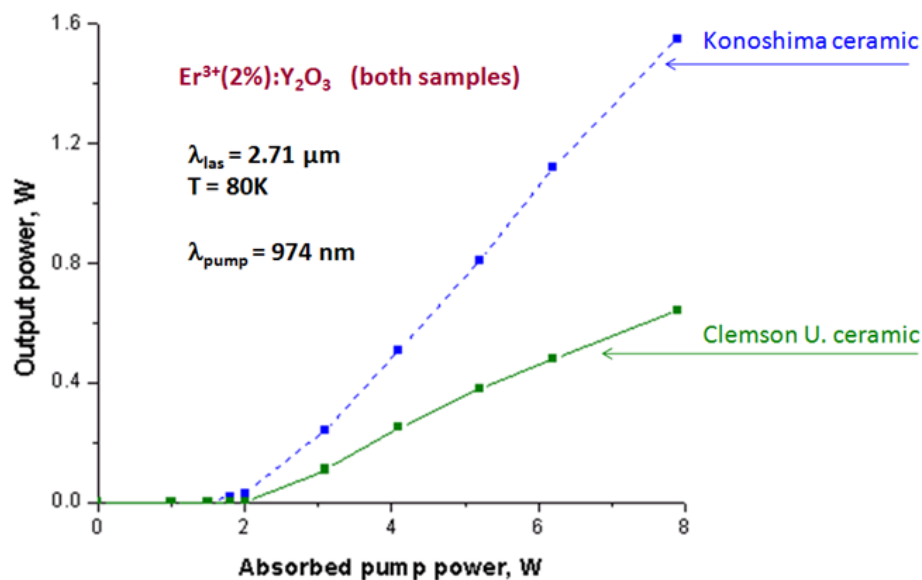


Figure 12. Laser measurement on the  $\text{Er}^{3+}:\text{Y}_2\text{O}_3$  ceramics at cryogenic temperatures relative to the best Japanese ceramics.

Efforts are underway to remake these ceramics from hydrothermally purified precursors which should reduce the background absorption and increase the radiative quantum efficiency.

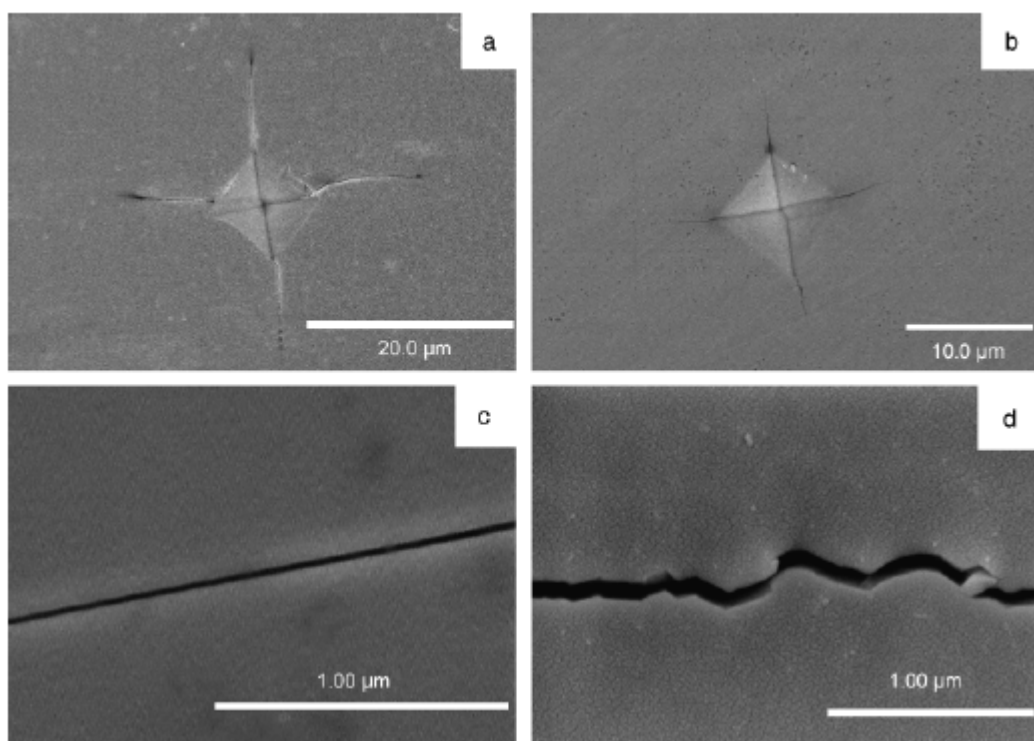


Figure 13. Micrograph of the indentation in (a) conventionally sintered ceramic and (b) hot isostatically pressed (HIPed) two-step-sintered ceramic; micrograph of the indentation crack in (c) a conventionally sintered ceramic and (d) a HIPed two-step-sintered ceramic.

The Vickers microhardness and fracture toughness for sub-micron grained  $Y_2O_3$  ceramics were measured by indentation. For comparison, an Er-doped  $Y_2O_3$  transparent ceramic was also prepared by conventional sintering at 2000 °C for 6 hours. The average grain size of this conventionally sintered ceramic was  $328 \pm 73 \mu\text{m}$ .

The microhardness and fracture toughness of the conventional sintered ceramic and HIPed two-step sintered transparent ceramics are shown in Table 1. The microhardness and fracture toughness of the conventionally sintered transparent  $Y_2O_3$  ceramics with an average grain size of  $328 \mu\text{m}$  are close to the value obtained by Harris, et al. [27] for hot isostatically pressed, polycrystalline  $Y_2O_3$  ceramics with an average grain size of  $450 \mu\text{m}$ . The microhardness of the conventionally sintered, large grain sized ceramic is 7.23 GPa. As the grain size decreases to  $0.3 \mu\text{m}$  by use of HIPed two-step sintering, the microhardness increases up to 9.09 GPa. It has commonly been accepted that microhardness generally increases with decreasing grain size as the dislocations generated by the indenter are blocked by the grain boundaries [28]. In conventionally sintered transparent ceramics with an average grain size of  $328 \mu\text{m}$ , the size of indentation is about  $10 \mu\text{m}$  which is very small compared to grain size. However, as the grain size decreased, the effect of grain boundaries become significant due to the increasing microhardness. The microhardness of HIPed two-step sintered ceramic exceeds that of the conventionally sintered ceramic by about 25%.

**Table 1. The microhardness and fracture toughness of transparent Er:Y<sub>2</sub>O<sub>3</sub> ceramics**

Sample	Microhardness (GPa)	Fracture toughness (MPa·m <sup>1/2</sup> )	Relative density (%)	Grain size (μm)
Conventional sintering	$7.23 \pm 0.35$	$0.81 \pm 0.07$	99.73	328
HIPed-Two step sintering	$9.09 \pm 0.41$	$1.39 \pm 0.07$	99.81	0.34

Fracture toughness also exhibited a similar behavior. The indentation cracks in the  $328 \mu\text{m}$  average grain sized samples are longer and straighter as shown in Figure 13 (a) and (c). As grain size decrease, the indentation cracks are shorter and less-straight as shown in Figure 11 (b) and (d), as a result of both the increasing fracture toughness. The fracture toughness of a HIPed two-step sintered ceramic with an average grain size of  $0.3 \mu\text{m}$  exceeds that of the conventionally sintered ceramic with an average grain size of  $328 \mu\text{m}$  by about 70%. A similar trend of the grain size dependence with microhardness and fracture toughness in fully dense  $Y_2O_3$  was also observed by Tani et al. [29].

### Section Conclusions

Er doped  $Y_2O_3$  nanopowders with the average particle size of 45 nm and low agglomeration were synthesized by a solution precipitation method. The green compacts of these nanopowders were sintered by two-step sintering and then hot isostatically pressed in order to obtain highly

transparent nanograined  $Y_2O_3$  ceramics. The resulting 0.3  $\mu m$  grain sized transparent  $Y_2O_3$  ceramic exhibited equivalent transparency to that of the single crystal beyond 1200 nm. The microhardness and fracture hardness of the HIPed two-step sintered transparent  $Y_2O_3$  ceramic with an average grain size of 0.3  $\mu m$  exceeded those of conventionally sintered transparent  $Y_2O_3$  ceramic with an average grain size of 328 with an average grain size of 0.3  $\mu m$  by 25% and 70%, respectively.

### References:

1. J. Kong, J. Lu, K. Takaichi, T. Uematsu, K. Ueda, D. Y. Tang, D. Y. Shen, H. Yagi, T. Yanagitani, and A. A. Kaminskii, *Appl. Phys. Lett.*, **82**[16] 2556-2558 (2003).
2. G. Boulon and V. Lupei, *J. Lumin.*, **125**[1-2] 45-54 (2007).
3. J. R. Lu, K. Takaichi, T. Uematsu, A. Shirakawa, M. Musha, K. Ueda, H. Yagi, T. Yanagitani, and A. A. Kaminskii, *Jpn. J. Appl. Phys.*, **41**[12A] L1373-L1375 (2002).
4. S. K. Dutta and G. E. Gazza, *Mater. Res. Bull.*, **4**[11] 791-& (1969).
5. H. Eilers, *J. Eur. Ceram. Soc.*, **27**[16] 4711-4717 (2007).
6. J. Mouzon, A. Maitre, L. Frisk, N. Lehto, and M. Oden, *J. Eur. Ceram. Soc.*, **29**[2] 311-316 (2009).
7. N. Saito, S. Matsuda, and T. Ikegami, *J. Am. Ceram. Soc.*, **81**[8] 2023-2028 (1998).
8. T. Ikegami, J. G. Li, T. Mori, and Y. Moriyoshi, *J. Am. Ceram. Soc.*, **85**[7] 1725-1729 (2002).
9. L. Wen, X. D. Sun, Q. Lu, G. X. Xu, and X. Z. Hu, *Opt. Mater.*, **29**[2-3] 239-245 (2006).
10. Y. H. Huang, D. L. Jiang, L. X. Zhang, and Q. L. Lin, *Chinese J. Inorg. Chem.* **25**[4] 571-577 (2009).
11. Greskovich, C and J. P. Chernoch, *J. Appl. Phys.*, **44**[10] 4599-4606 (1973).
12. W. H. Rhodes, *J. Am. Ceram. Soc.*, **64**[1] 13-19 (1981).
13. A. Ikesue, K. Kamata, and K. Yoshida, *J. Am. Ceram. Soc.*, **79**[2] 359-364 (1996).
14. G. Wang and V. D. Krstic, *Philos. Mag. A*, **78**[5] 1125-1135 (1998).
15. I. W. Chen and X. H. Wang, *Nature*, **404**[6774] 168-171 (2000).
16. X. H. Wang, P. L. Chen, and I. W. Chen, *J. Am. Ceram. Soc.*, **89**[2] 431-437 (2006).
17. K. Serivalsatit, B. Y. Kokuoz, B. Kokuoz, and J. Ballato, *Optics Letters*, **34**[7] 1033-1035 (2009).
18. M. Mendelson, *J. Am. Ceram. Soc.*, **52**[8] 443-& (1969).
19. A. A. Kaminskii, M. S. Akchurin, R. V. Gainutdinov, K. Takaichi, A. Shirakawa, H. Yagi, T. Yanagitani, and K. Ueda, *Crystallogr. Rep.*, **50**[5] 869-873 (2005).
20. G. R. Anstis, P. Chantikul, B. R. Lawn, and D. B. Marshall, *J. Am. Ceram. Soc.*, **64**[9] 533-538 (1981).
21. L. M. Seaverson, S. Q. Luo, P. L. Chien, and J. F. McClelland, *J. Am. Ceram. Soc.*, **69**[5] 423-429 (1986).
22. K. Nakamoto, pp. xv, 338 p. in 2d ed.). New York, : Wiley-Interscience. (1970).
23. I. Takayasu, J. G. Li, I. Sakaguchi, and K. Hirota, *J. Am. Ceram. Soc.*, **87**[3] 517-519 (2004).
24. H. Gong, D. Y. Tang, H. Huang, T. S. Zhang, and J. Ma, *Mater. Chem. Phys.*, **112**[2] 423-426 (2008).
25. M. N. Rahaman, pp. 482-485, CRC/Taylor & Francis, Boca Raton, FL (2007).
26. J. G. Li and Y. P. Ye, *J. Am. Ceram. Soc.*, **89**[1] 139-143 (2006).

27. D. C. Harris, G. A. Hayes, N. A. Jaeger, L. D. Sawyer, R. C. Scheri, M. E. Hills, K. R. Hayes, S. E. Homer, Y. L. Tsai, and J. J. Mecholsky, *J. Am. Ceram. Soc.*, **75**[5] 1247-1253 (1992).
28. I. J. McColm, pp. 6, Plenum Press, New York, 1990.
29. T. Tani, Y. Miyamoto, M. Koizumi, and M. Shimada, *Ceram. Int.*, **12**[1] 33-37 (1986).

## **Section IV. Sub-micrometer Grain-Sized Transparent Erbium-doped Scandia Ceramics**

### **Section Summary**

Er-doped transparent  $\text{Sc}_2\text{O}_3$  ceramics with an average grain-size of 0.3- $\mu\text{m}$  were synthesized from solution-derived nanoparticles using a two-step sintering process followed by hot isostatic pressing (HIP). The two-step sintered ceramics showed a remarkable decrease in grain size with relative density over 98% prior to HIPing. After HIPing, the  $\text{Sc}_2\text{O}_3$  ceramics became highly transparent, with negligible grain growth, and exhibited optical transmittance of about 80%, nominally the Fresnel limit, for wavelengths greater than about 1.0  $\mu\text{m}$ .

### **Introduction**

Scandia ( $\text{Sc}_2\text{O}_3$ ) is a promising host material for high energy solid state lasers [1] This cubic sesquioxide readily can be doped with rare earth ions thus permitting a wide range of possible emissions.[2-5] Moreover,  $\text{Sc}_2\text{O}_3$  exhibits a thermal conductivity of about 17 W/m·K, which is higher than that for YAG (~ 11 W/m·K) or for  $\text{Y}_2\text{O}_3$  (14W/m·K) [6]. Thermal conductivity is especially critical as high energy laser systems continue to scale towards multi-kilowatt power levels.

Unfortunately,  $\text{Sc}_2\text{O}_3$  possesses a melting temperature of about 2420 °C [6], which makes the growth of high purity and quality crystals using melt techniques difficult though lower temperature hydrothermal methods have proven successful [7]. Transparent ceramics offer an alternative route to such refractory oxide gain media.

Ceramics typically can be processed at lower temperatures (~ 70% of the melting temperature) [8] therefore by-passing some of the challenges of single crystal growth from high temperature melts. Furthermore, ceramics can possess added advantages relative to single crystals including faster production rates, the fabrication of both larger sizes and composite laser structures, uniform doping concentrations, and better mechanical behavior [9-10]

Transparent  $\text{Sc}_2\text{O}_3$  ceramics have been successfully fabricated by vacuum sintering compacts of nanoparticles at high temperature (1700° – 1750 °C) [5,8,11-12] These  $\text{Sc}_2\text{O}_3$  ceramics have relatively large grain sizes, ranging from 10-30  $\mu\text{m}$ , due to significant grain growth that occurs during the final stage of sintering [5,8,11]. As a result of the larger grain sizes these ceramics generally do not offer significant enhancements to strength or thermal shock resistance if compared to transparent ceramics with smaller grain size [13].

Pressure-assisted sintering, e.g., hot isostatic pressing (HIP), can be an effective approach for achieving full density and small grain size. A key advantage of pressure-assisted sintering is the

ability to enhance significantly the densification rate relative to the coarsening rate. Thus, a sample can be sintered to high density at lower sintering temperature or shorter sintering time than conventional sintering thereby promoting a smaller grain size. However, the sample must first achieve a fairly high level of closed porosity (> 92% of theoretical density) in order to transmit more effectively the external pressure exerted during HIP. However, at such levels of densification rapid grain growth usually occurs during the final stage of sintering. Additionally, pores tend to separate from the grain boundaries due to abnormal grain growth. Those pores, now isolated within a grain, are more difficult to remove when compared with those pores located along grain boundaries where multiple diffusion pathways exist. These residual pores scatter light and greatly reduce the transparency of the resultant ceramics. The high level of transparency particularly required for high energy laser systems necessitates very low residual porosity.

Two-step sintering, first proposed by Chen, et al., [14-15] is a promising technique to fabricate dense nanocrystalline ceramics without grain growth in the final stage of sintering. In the first step, a sample is heated to a higher temperature ( $T_1$ ) to obtain a density greater than 75%, which corresponds to a condition in which pores are unstable against shrinkage. The sample is then cooled to a lower temperature ( $T_2$ ) where grain boundary diffusion is active but grain boundary migration is greatly slowed. Therefore, densification should continue without significant grain growth by prolonged isothermal heating at the lower temperature. This technique is a promising approach for obtaining high density samples with small grain sizes, which then can be HIPed to achieve high transparency. This has been shown experimentally for another cubic sesquioxide, yttria [13,16].

In this work, we report the fabrication of sub-micrometer grain-sized transparent  $\text{Sc}_2\text{O}_3$  ceramics by two-step sintering followed by HIP. Even though the sesquioxides are cubic, hence optically isotropic, grain boundaries can often cause optical scattering and so the synthesis of such sub-micrometer, hence sub-wavelength, grain-sized ceramics should exhibit reduced scattering. This is critical for next generation high energy laser systems where absorption and scattering must be mitigated.

## **2. Experimental procedure**

### *2.1 Powder preparation and sample compaction*

In this study, 0.25 atom percent Er-doped  $\text{Sc}_2\text{O}_3$  nanopowders were prepared by a co-precipitation technique. A scandium nitrate solution was prepared by dissolving  $\text{Sc}_2\text{O}_3$  powder in excess amounts of nitric acid at approximately 80°C. Erbium nitrate pentahydrate (Acros Organics, 99.9%, Fair Lawn, NJ) was added into the scandium nitrate solution to yield 0.25 atom% Er doped  $\text{Sc}_2\text{O}_3$ . A 1.0 M ammonium hydroxide was solution added drop-wise into an equivolume amount of 0.2 M erbium doped scandium nitrate solution in order to precipitate erbium-doped scandium hydroxide. After homogenizing for an hour, the hydroxyl precipitates were separated by centrifugation and then washed several times with water. Erbium-doped scandium sulfate was prepared by dissolving the hydroxyl precipitates with a stoichiometric amount of sulfuric acid. In this case, the Er-doped  $\text{Sc}_2\text{O}_3$  nanopowders were prepared by adding drop-wise a 1.0 M hexamethylenetetramine (HMT) solution into the 0.1 M of scandium sulfate solution under mild stirring at 80°C. HMT releases  $\text{OH}^-$  gradually during heating, which help to control homogeneous precipitation [17] After homogenizing for an hour, the precipitates were

washed several times with water and dried in vacuum oven at 70°C. The precursors were calcined at 1100°C for 4 hours under flowing oxygen gas at 3 L/min to yield Sc<sub>2</sub>O<sub>3</sub> nanopowders.

The morphology of the Sc<sub>2</sub>O<sub>3</sub> nanopowder was observed using transmission electron microscopy (TEM; model H7600T, Hitachi, Pleasanton, CA). The average particle size was determined by averaging the diameter of approximately 200 particles. Phase identification was performed by an X-ray diffractometer (XRD; XDS 2000, Scintag, Cupertino, CA) using CuK<sub>α</sub> with wavelength of 0.15406 nm in the range of 2θ = 10°-70°. Infrared spectra were recorded by Fourier transformed infrared spectrometer (FTIR; Nicolet 6700 FT-IR, Thermo Scientific, Waltham, MA) in the region of 400-4000 cm<sup>-1</sup>. The calcined nanopowders were uniaxially pressed into pellets at approximately 15 MPa without any binder and then cold isostatically pressed under a pressure of 200 MPa. The green density of pellets was about 50%.

## 2.2 Sintering

Conventional sintering was carried out at 1300°-1600°C under vacuum (<10<sup>-3</sup> Pa) at a heating rate of 10°C/min in 50°C temperature intervals. After reaching the desired temperature the furnace was cooled naturally to room temperature. For two-step sintering, the green compacts were heated to a higher temperature (T<sub>1</sub>) with a heating rate of 10°C/min and cooled down to a lower temperature (T<sub>2</sub>) with a cooling rate of 50°C/min. The samples were isothermally held at T<sub>2</sub> for 20 hours.

In order to obtain transparent Sc<sub>2</sub>O<sub>3</sub> ceramics, the dense (> 98%) two-step sintered samples were subsequently hot isostatically pressed (HIP; model 6-30H, American Isostatic Press, Columbus, OH) at 1300°C under an argon pressure of 206 MPa for 3 hours which is denoted as 'HIPed two-step sintering.'

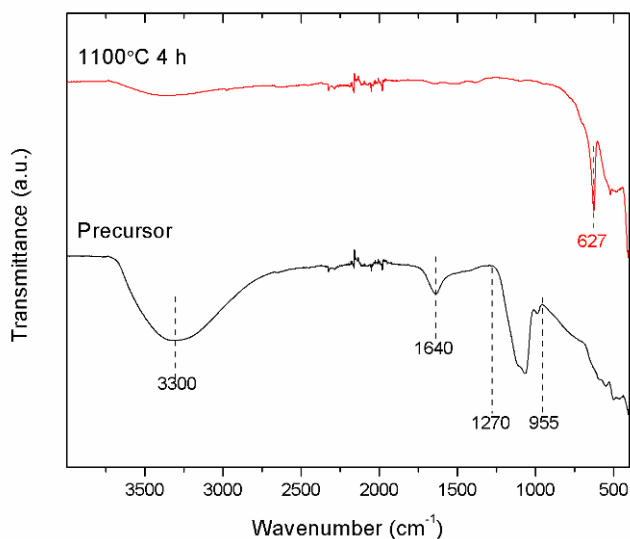


**Figure 1. FTIR spectra of the precipitated precursors and the Er-doped Sc<sub>2</sub>O<sub>3</sub> nanopowder calcined at 1100°C for 4 hours.**

### 2.3 Characterization of sintered samples

The bulk density of the sintered samples was determined by the Archimedes method using distilled water. The density of distilled water is 0.9982 g/cm<sup>3</sup>. The relative density was determined as the ratio of measured density to theoretical density of Sc<sub>2</sub>O<sub>3</sub> which is 3.84 g/cm<sup>3</sup> (JCPDS card no.42-1463). The sintered samples were mechanically polished using 600, 800, and 1200 grit silicon carbide papers. Final polishing was performed with colloidal silica suspension. The microstructure of the sintered samples was observed using a field-emission scanning electron microscopy (FE-SEM; model 4800, Hitachi, Pleasanton, CA). The average grain size of the sintered samples was determined by lineal intercept method from SEM images followed ASTM E112-96. Based upon the tetrakaidecahedron shape model and a log-normal distribution of grain sizes, the average grain size was calculated using  $\bar{D} = 1.571 C/(M \cdot N)$ , where  $\bar{D}$  is the average grain size;  $C$  the measuring line length;  $M$  the magnification; and  $N$  the number of grains intercepted by measuring line [18]. The optical transmittance of the sintered Sc<sub>2</sub>O<sub>3</sub> ceramics was measured over the wavelength region from 200 to 2000 nm using a UV-VIS spectrometer (Perkin Elmer UV/VIS/NIR Lambda 900, Norwalk, CT) at normal incidence. The samples thickness is about 1 mm.

## 3. Results and Discussion

### 3.1 Powder characterization

The FTIR spectra of the precipitate precursor and the Sc<sub>2</sub>O<sub>3</sub> nanopowder calcined at 1100°C for 4 hours are shown in Fig. 1. The precipitated precursor exhibits the absorption band of a hydrated basic sulfate [8]. The broad peak at ~3300 cm<sup>-1</sup> is attributed to the OH stretching vibration which is the coupled effects of molecular water (symmetric  $\nu_1$  and anti-symmetric  $\nu_3$ , at ~3200-3500 cm<sup>-1</sup>) and free hydroxyl groups which are coordinated with scandium ions but not part of molecular water (~3000-3800 cm<sup>-1</sup>). The absorption peak at ~1640 cm<sup>-1</sup> is the characteristic of H-O-H bending mode ( $\nu_2$ ) of molecular water. The multiple bands in the ~955-1270 cm<sup>-1</sup> range are characteristic of SO<sub>4</sub><sup>2-</sup>. The absorption due to molecular water, free hydroxyls, and SO<sub>4</sub><sup>2-</sup> are no longer present after calcining at 1100°C for 4 hours. The absorption peak at ~627 cm<sup>-1</sup> is attributed to the Sc-O vibration. XRD patterns of the precipitate precursor and the Sc<sub>2</sub>O<sub>3</sub> nanopowders calcined at 1100°C for 4 hours are shown in Fig. 2. The precipitated precursor exhibits a low degree of crystallinity and the XRD pattern cannot be identified against known scandium oxide compounds. However, a similar XRD pattern was also observed by Li, et al., [19] from the precursor prepared by a similar method. After calcination at 1100 °C for 4 hours, the precursor transforms into cubic Sc<sub>2</sub>O<sub>3</sub> (JCPDS card no. 42-1463). The morphology of Er-doped Sc<sub>2</sub>O<sub>3</sub> nanopowders calcined at 1100°C for 4 hours is shown in Fig. 3. The calcined nanopowders are loosely agglomerated and uniform in size with average particle size of 39 ± 12 nm.

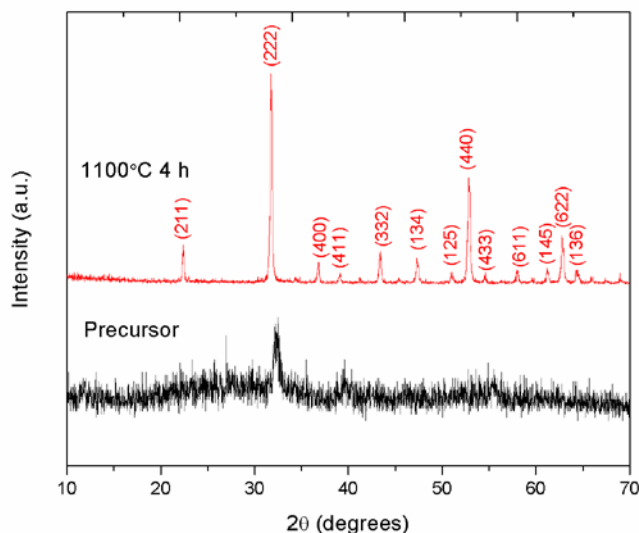


**Figure 2. XRD patterns of the precipitate precursor and the Er-doped  $\text{Sc}_2\text{O}_3$  nanopowder calcined at 1100°C for 4 hours.**

## 3.2 Sintering

### 3.2.1 Conventional sintering

Conventional sintering was carried out in order to study the effect of sintering temperature on densification and grain growth. Figure 4 shows the relative density and the grain size of the sintered samples as a function of temperature. The relative density of the sintered samples increases rapidly from 72% to 92% with increasing temperature in the range of 1300-1450 °C while the grain size of sintered samples increases slowly. In contrast, the relative density of the sintered samples increases slowly to about 1450 °C while the grain size of sintered samples increases rapidly. The densification was nearly complete (>99%) at 1600°C without an isothermal dwell.

Figure 5 shows the average grain size as a function of relative density. The average grain size increases slowly with an increasing in the relative density below 92%. However, the average grain size increases rapidly with an increase in relative density above 92%. The transition in grain growth behavior indicates the transition of sintering state from intermediate state to final stage. According to Coble's sintering model, [20] the cylindrical pores locate along the grain edges during the intermediate state. These pores can limit the grain boundary migration, for which grain growth is suppressed. These pore channels collapse becoming isolated pores after the final stage begins which results in a decrease in pore pinning and accelerated grain growth [21-22].

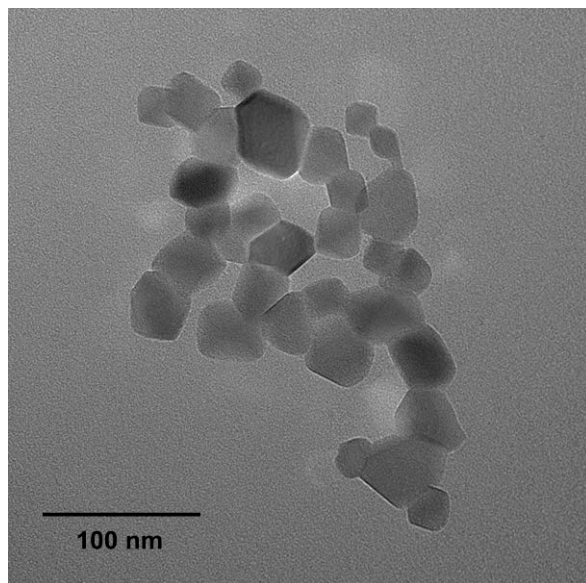


**Figure 3.** Transmission electron microscopy of Er-doped Sc<sub>2</sub>O<sub>3</sub> nanopowders calcined at 1100°C for 4 hours.

### 3.2.2 Two-step sintering

Green compacts were sintered using various two-step firing schedules as shown in Table 1. The relative density and the average grain size of the sintered samples are also included in Table 1.

**Table 1.** Two-step sintering of Er-doped Sc<sub>2</sub>O<sub>3</sub> ceramics

Sample	T <sub>1</sub> (°C)	Relative density (%)	Grain size G <sub>1</sub> (µm)	T <sub>2</sub> (°C)	Relative density (%)	Grain size G <sub>2</sub> (µm)
TSS1	1550	97.89	0.49	1500	99.59	0.68
TSS2	1550	97.89	0.49	1450	99.28	0.59
TSS3	1550	97.89	0.49	1400	99.17	0.50
TSS4	1500	95.66	0.38	1450	99.59	0.76
TSS5	1500	95.66	0.38	1400	99.09	0.47
TSS6	1500	95.66	0.38	1350	99.28	0.40
TSS7	1450	92.23	0.31	1400	99.27	0.45
TSS8	1450	92.23	0.31	1350	99.29	0.37
TSS9	1450	92.23	0.31	1300	99.22	0.30
TSS10	1450	92.23	0.31	1250	94.87	0.32
TSS11	1400	86.05	0.25	1350	98.87	0.36
TSS12	1400	86.05	0.25	1325	98.18	0.28

TSS13	1400	86.05	0.25	1300	92.52	0.28
-------	------	-------	------	------	-------	------

According to Chen and Wang, [14-15] the success of two-step sintering depends strongly on the selections of  $T_1$  and  $T_2$ . The green compacts are sintered at  $T_1$  in order to obtain a relative density higher than 75% in order to render pores unstable and able to shrink. If the relative density is lower than this critical density, the pore size is large compared to the grain size. Thus, such pores are thermodynamically stable and can not be removed [23]. This critical density may vary, depending on pore size and microstructure [24], which is influenced by the morphology of the precursor powders and the forming process. In this work, the lowest starting density for the second step was 86%.

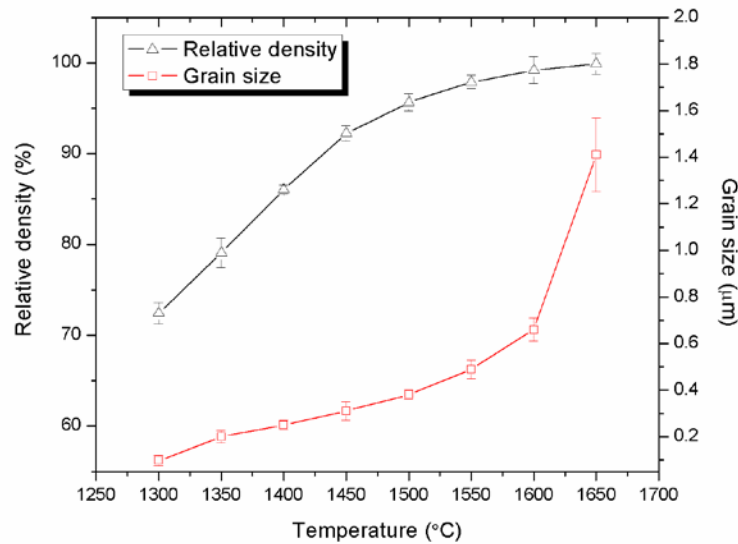


**Figure 4. The relative density and average grain size of Er-doped  $Sc_2O_3$  ceramics versus sintering temperature.**

For the selection of  $T_2$ , the second step sintering must be performed at the temperature where grain boundary migration is suppressed while grain boundary diffusion remains active [14-15]. If the second step sintering is performed at too low of a temperature, sintering is exhausted before full density is achieved. If the second step sintering is performed at too high temperature, grain growth is observed. The kinetic window for reaching full density without grain growth is shown in Fig. 6. where the solid symbols indicate the condition to obtain full density without grain growth for the  $Sc_2O_3$  samples synthesized in this work. The open symbols that lie above the upper boundary indicate conditions where grain growth will occur. The open symbols that lie below the lower boundary indicate conditions where no grain growth is observed but densification is exhausted. It could be seen that the upper boundary of  $T_2$  required for densification without grain growth increases with the increasing grain size at  $T_1$  ( $G_1$ ). This can be explained by the increasing driving force at smaller grain sizes, so that grain growth of smaller grain-sized ceramics occurs at lower temperatures [14-15,25-26]. In contrast, the lower boundary of  $T_2$  required for the densification without grain growth decreases with the increasing  $G_1$ . This suggests that grain boundary diffusion itself can be suppressed at lower temperature. Interface kinetics in very fine grain materials generally is limited due to difficulties in maintaining diffusion sources and sinks to accommodate point defects. This effect is lessened at

larger grain sizes so densification can progress at lower temperatures [14-15,25-26]. A similar kinetic window is also observed in  $Y_2O_3$  [14-15],  $BaTiO_3$  [25-26], Ni-Cu-Zn Ferrite [25], and  $BiScO_3$ - $PbTiO_3$  [27].

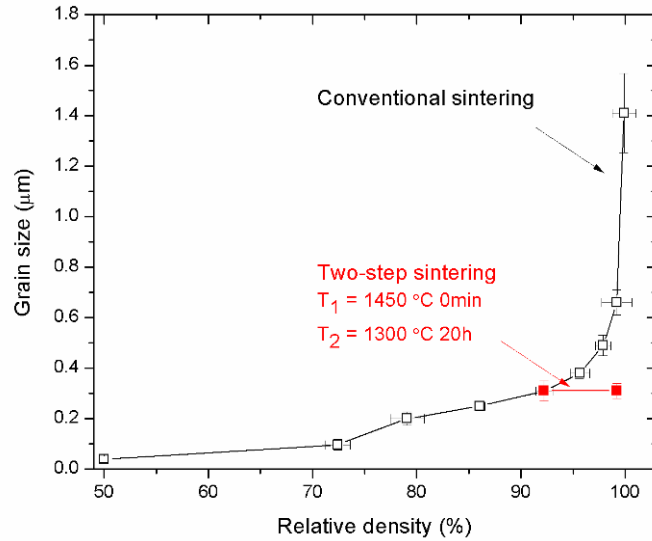


**Figure 5. The average grain size and relative density of Er-doped  $Sc_2O_3$  in two-step sintering and conventional sintering.**

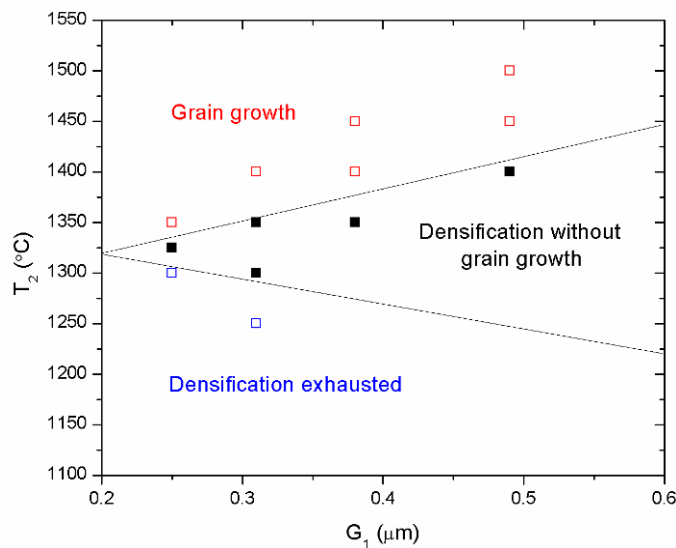


**Figure 6. Kinetic window for achieving full density without grain growth.**

A comparison of microstructural development versus relative density of Er-doped  $Sc_2O_3$  ceramics sintered by two-step sintering and by conventional sintering is shown in Fig. 5. As can be seen, dense  $Sc_2O_3$  ceramics with average grain size about  $0.3 \mu m$  are produced by two-step sintering. The grain size of two-step sintered ceramics is significantly smaller than those prepared using conventional sintering. Unfortunately, these two-step sintered ceramics are opaque, likely due to the remnant porosity in microstructure.

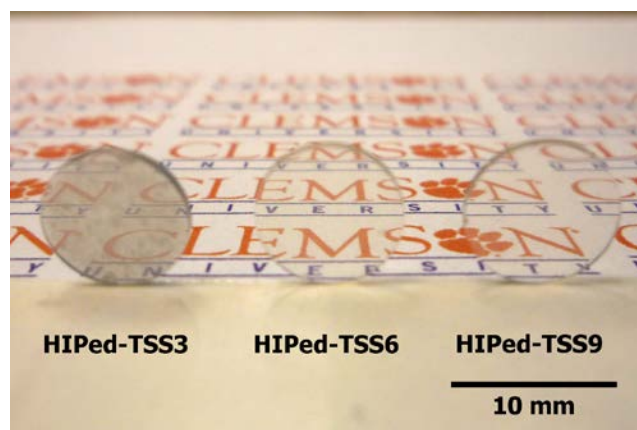


Figure 7. Optical micrograph of polished hot isostatically pressed two-step-sintered (HIPed-TSS) Er-doped  $\text{Sc}_2\text{O}_3$  ceramics.

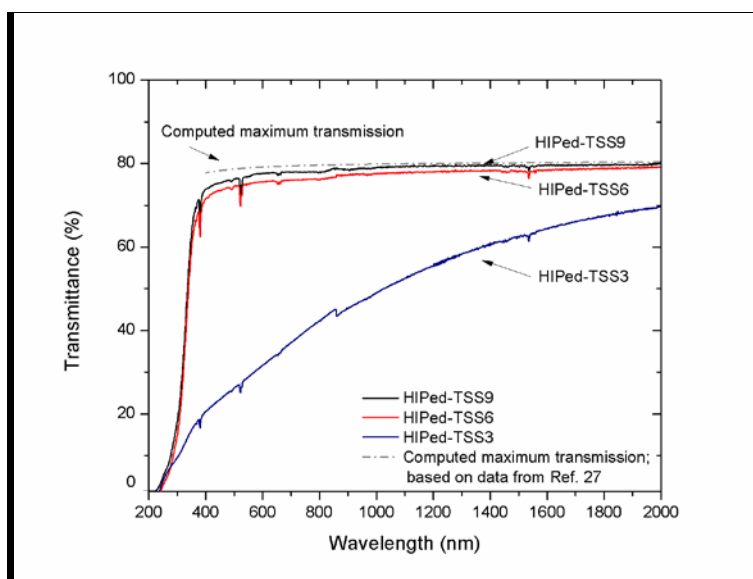


Figure 8. The optical transmittance of HIPed two-step-sintered (HIPed-TSS) Er-doped  $\text{Sc}_2\text{O}_3$  ceramics

Two-step sintering was also performed at higher temperatures (TSS1, TSS2, and TSS3, see Table 1) in order to investigate the feasibility of fabricating sub-micrometer grained transparent  $\text{Sc}_2\text{O}_3$  ceramics by two-step sintering without HIP. TSS1 exhibited the best transparency. However, it was, at best, translucent and not transparent. Therefore, the further HIP was conducted in order to remove residual pores in the microstructure.

### 3.3.3 Hot Isostatic pressing

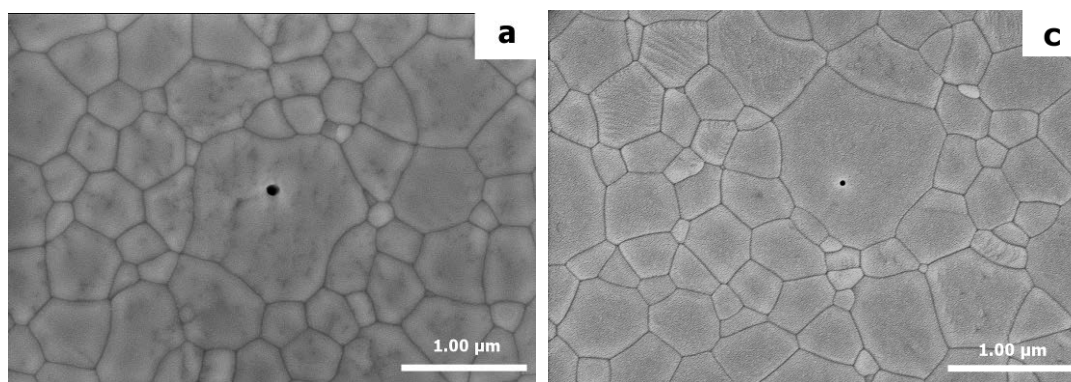
Hot isostatic pressing (HIP) was performed at 1300 °C under an argon pressure of 206 MPa for 3 hours using the high density two-step sintered samples, i.e., TSS3, TSS6, and TSS9. Each sample was sintered at different  $T_1$  and  $T_2$  values. The HIPed two-step-sintered samples are denoted as HIPed-TSS. The average grain size of HIPed two-step-sintered ceramics is close to the average grain size of two-step sintered ceramics, as is shown in Table 2. HIP at lower

temperatures can eliminate the residual pores by taking advantage of pressure-assisted densification without promoting grain growth.

**Table 2. The average grain size and the optical transmittance of sintered Er-doped Sc<sub>2</sub>O<sub>3</sub> ceramics.**

Sample	Grain size (μm)		The optical transmittance of HIPed two-step sintered ceramics (%)	
	Two-step sintering	HIPed two-step sintering	at 1.53 μm	at 1.00 μm
TSS3	0.50 ± 0.05	0.53 ± 0.08	63	49
TSS6	0.40 ± 0.03	0.42 ± 0.04	79	79
TSS9	0.30 ± 0.03	0.33 ± 0.04	80	80

Figure 7 shows an optical micrograph of selected polished HIPed two-step sintered-ceramics. The HIPed-TSS3 has lower transparency compare to the others. The optical transmittance of polished HIPed two-step sintered-ceramics is shown in Fig. 8. For comparison, the calculated maximum transmission, using refractive index data reported by Takaichi, et al.<sup>28</sup> is also included in Fig. 8. The absorption peaks at about 382, 525, 658, and 1534 nm are due to the absorption transition of Er<sup>3+</sup> ions [29]. The transmittance of HIPed-TSS3 is about 63% at the wavelength of 1.53 μm, which is the main emission of interest from Er<sup>3+</sup>.<sup>29</sup> The transmittance of HIPed-TSS6 and HIPed-TSS9 at the wavelength of 1.53 μm is about 79% and 80%, respectively. Also, the transmittance of HIPed two-step ceramics at 1.0 μm, which is not resonant with an Er<sup>3+</sup> absorption band yet is close to the emission of other active laser ions, i.e. Yb<sup>3+</sup> and Nd<sup>3+</sup>, is included in Table 2. The lower transmittance of HIPed-TSS3 compare to the others might be explained by the effect of T<sub>1</sub>. TSS3 was sintered at T<sub>1</sub> equal to 1550°C. At 1550°C, grains begin growing rapidly as was shown in Fig. 4.



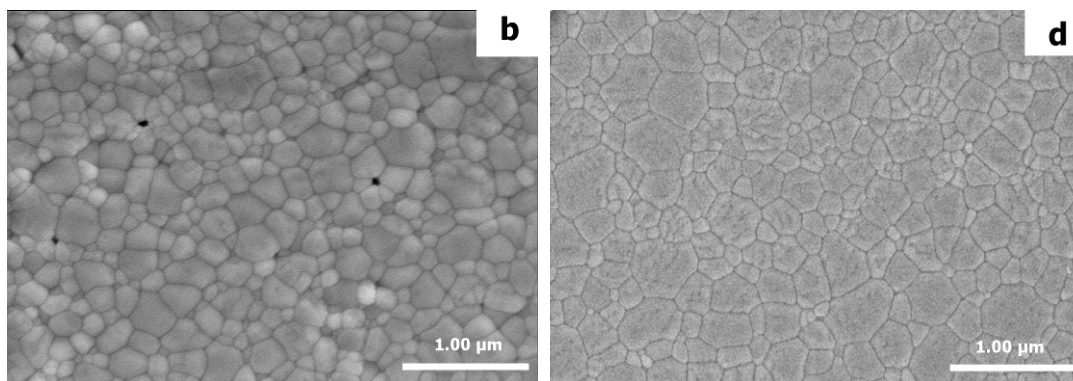


**Figure 9. Scanning electron microscopy micrograph of the microstructure of Er-doped  $\text{Sc}_2\text{O}_3$  ceramic sintered (a) at  $1550^\circ\text{C}$  for 0 min and (b) at  $1450^\circ\text{C}$  for 0 min, and the microstructure of (c) HIPed-TSS3 and (d) HIPed-TSS9.**

As a result, pores tend to separate from the grain boundaries and become intra-granular pores as shown in Fig. 9(a). These pores cannot be eliminated by two-step sintering and HIP, as shown in Fig. 9(c), resulting in the reduction of transparency due to scattering. The reduction of the transmittance at a shorter wavelength is also due to the scattering of the residual pores in microstructure. On the other hand, TSS6 and TSS9 were sintered at  $T_1$  equal to  $1500^\circ\text{C}$  and  $1450^\circ\text{C}$ , respectively. At such temperatures, grains grow slowly and pores are located at grain boundaries and triple grain junctions as is shown in Fig. 9(b). The inter-granular pores can be eliminated by two-step sintering and HIP, as shown in Fig. 9(d), resulting in the higher transparency. Therefore, the selection of  $T_1$  is critical since it influences the final grain size and transparency of the transparent ceramics.

## Conclusion

Loosely agglomerated 0.25% Er-doped  $\text{Sc}_2\text{O}_3$  nanopowders with an average particle size of about 40 nm were synthesized by solution precipitation using scandium sulfate and hexamethylenetetramine (HMT). The Er-doped  $\text{Sc}_2\text{O}_3$  ceramics with average grain size of 0.3  $\mu\text{m}$  and a relative density over 99% were obtained by using two-step sintering. The subsequent HIP of these ceramics led to submicrometer grain sized highly transparent  $\text{Sc}_2\text{O}_3$  ceramics. The optical transmittance of the transparent  $\text{Sc}_2\text{O}_3$  ceramics at the wavelength of 1.53  $\mu\text{m}$  reached 80%.

## Section References:

1. L. Fornasiero, E. Mix, V. Peters, K. Petermann, and G. Huber, *Cryst. Res. Technol.*, **34**[2] 255-260 (1999).
2. J. Lu, J. F. Bisson, K. Takaichi, T. Uematsu, A. Shirakawa, M. Musha, K. Ueda, H. Yagi, T. Yanagitani, and A. A. Kaminskii, *Appl. Phys. Lett.*, **83**[6] 1101-1103 (2003).
3. A. Lupei, V. Lupei, C. Gheorghe, and A. Ikesue, *J. Lumin.*, **128**[5-6] 918-920 (2008).
4. V. Lupei, A. Lupei, C. Gheorghe, and A. Ikesue, *J. Lumin.*, **128**[5-6] 901-904 (2008).
5. C. Gheorghe, A. Lupei, V. Lupei, L. Gheorghe, and A. Ikesue, *J. Appl. Phys.*, **105**[12] - (2009).
6. L. Fornasiero, E. Mix, V. Peters, K. Petermann, and G. Huber, *Ceram. Int.*, **26**[6] 589-592 (2000).
7. C. D. McMillen and J. W. Kolis, *J. Cryst. Growth*, **310**[7-9] 1939-1942 (2008).

8. J. G. Li, T. Ikegami, and T. Mori, *J. Am. Ceram. Soc.*, **88**[4] 817-821 (2005).
9. A. A. Kaminskii, M. S. Akchurin, R. V. Gainutdinov, K. Takaichi, A. Shirakava, H. Yagi, T. Yanagitani, and K. Ueda, *Crystallogr. Rep.*, **50**[5] 869-873 (2005).
10. V. Lupei, A. Lupei, and A. Ikesue, *J. Alloys Compd.*, **380**[1-2] 61-70 (2004).
11. J. G. Li, T. Ikegami, and T. Mori, *J. Mater. Res.*, **18**[8] 1816-1822 (2003).
12. V. Lupei, A. Lupei, and A. Ikesue, *Appl. Phys. Lett.*, **86**[11] 111118 (2005).
13. K. Serivalsatit, B. Kokuoz, B. Y. Kokuoz, M. Kennedy, and J. Ballato, *J. Am. Ceram. Soc.*, **93**[5] 1320-1325 (2010).
14. I. W. Chen and X. H. Wang, *Nature*, **404**[6774] 168-171 (2000).
15. X. H. Wang, P. L. Chen, and I. W. Chen, *J. Am. Ceram. Soc.*, **89**[2] 431-437 (2006).
16. K. Serivalsatit, B. Y. Kokuoz, B. Kokuoz, and J. Ballato, *Opt. Lett.*, **34**[7] 1033-1035 (2009).
17. P. L. Chen and I. W. Chen, *J. Am. Ceram. Soc.*, **76**[6] 1577-1583 (1993).
18. M. Mendelson, *J. Am. Ceram. Soc.*, **52**[8] 443-446 (1969).
19. J. G. Li, T. Ikegami, T. Mori, and Y. Yajima, *J. Am. Ceram. Soc.*, **87**[6] 1008-1013 (2004).
20. R. L. Coble, *J. Appl. Phys.*, **32**[5] 6 (1961).
21. C. P. Cameron and R. Raj, *J. Am. Ceram. Soc.*, **71**[12] 1031-1035 (1988).
22. M. Mazaheri, A. M. Zahedi, and S. K. Sadrnezhaad, *J. Am. Ceram. Soc.*, **91**[1] 56-63 (2008).
23. W. D. Kingery and B. Francois, in *Sintering and Related Phenomena*. Edited by G. C. Kuczynski, N. S. Hooton, and C. F. Gibbon. Gordon and Breach, New York, 1967.
24. K. Bodisova, P. Sajgalik, D. Galusek, and P. Svancarek, *J. Am. Ceram. Soc.*, **90**[1] 330-332 (2007).
25. X. H. Wang, X. Y. Deng, H. L. Bai, H. Zhou, W. G. Qu, L. T. Li, and I. W. Chen, *J. Am. Ceram. Soc.*, **89**[2] 438-443 (2006).
26. X. H. Wang, X. Y. Deng, H. Zhou, L. T. Li, and I. W. Chen, *J. Electroceram.*, **21**[1-4] 230-233 (2008).
27. T. T. Zou, X. H. Wang, W. Zhao, and L. T. Li, *J. Am. Ceram. Soc.*, **91**[1] 121-126 (2008).
28. K. Takaichi, H. Yagi, P. Becker, A. Shirakawa, K. Ueda, L. Bohaty, T. Yanagitani, and A. A. Kaminskii, *Laser Phys. Lett.*, **4**[7] 507-510 (2007).
29. C. Gheorghe, S. Georgescu, V. Lupei, A. Lupei, and A. Ikesue, *J. Appl. Phys.*, **103**[8] - (2008).

## Section V. Synthesis of Er-doped Lu<sub>2</sub>O<sub>3</sub> Nanoparticles and Transparent Ceramics

### Section Summary

Transparent rare earth-doped Lu<sub>2</sub>O<sub>3</sub> ceramics have received much attention for use in solid-state scintillator and laser applications. The fabrication of these ceramics, however, requires ultrafine and uniform powders as precursors. Presented here is the synthesis of Er-doped Lu<sub>2</sub>O<sub>3</sub> nanopowders by a solution precipitation method using Er-doped lutetium sulfate solution and hexamethylenetetramine as a precipitant and the fabrication of Er-doped Lu<sub>2</sub>O<sub>3</sub> transparent ceramics from these nanopowders. The precipitated precursors were calcined at 1100 °C for 4 hours in order to convert the precursors into Lu<sub>2</sub>O<sub>3</sub> nanoparticles with an average particle size of

60 nm. Thermal decomposition and phase evolution of the precursors were studied by simultaneous thermal analysis (STA), Fourier transform infrared spectroscopy (FTIR) and x-ray diffraction (XRD). Er-doped  $\text{Lu}_2\text{O}_3$  transparent ceramics were fabricated from these nanopowders using vacuum sintering followed by hot isostatic pressing at 1700 °C for 8 hours. The transparent ceramics exhibit an optical transmittance of 78% at a wavelength of 1.55  $\mu\text{m}$ .

## Introduction

Rare-earth doped lutetium oxide ( $\text{Lu}_2\text{O}_3$ ) has attracted interest as a potential material for application in scintillators and lasers [1, 2]. The interest is attributable to its broad range of transparency, relatively low phonon energy, and high stopping power for x-rays [1, 3]. Furthermore, it possesses a low thermal expansion coefficient ( $4 \times 10^{-7} \text{ K}^{-1}$ ) and high thermal conductivity (12.5 W/mK), which are critical for high power laser gain media [2, 4]. However, growing high-purity and quality rare-earth doped lutetium oxide single crystals is quite difficult due to its high melting temperature (2490 °C).

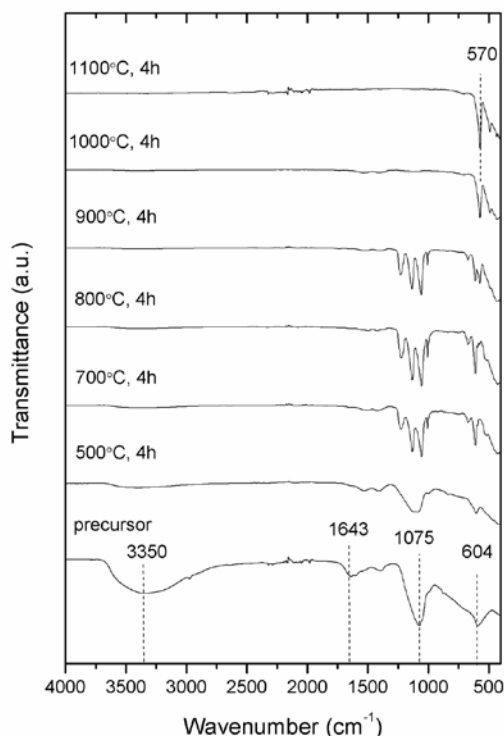


**Figure 1. FTIR spectra of the precipitate precursor and the Er: $\text{Lu}_2\text{O}_3$  nanopowders calcined at various temperatures for 4 hours.**

Transparent ceramics have been intensively developed as an alternative to single crystals for many years. Compared with single crystals, transparent ceramics possess selected advantages including lower fabrication temperatures, feasibility for larger size samples, better chemical homogeneity, and enhanced mechanical properties [5, 6]. Due to the cubic crystallographic structure of lutetium oxide, it should be possible to achieve high transparency without scattering

from grains of different orientations. Transparent rare-earth doped  $\text{Lu}_2\text{O}_3$  ceramics have been successfully fabricated by combination of nanocrystalline powder technology and vacuum sintering [2, 7] or atmosphere controlled sintering method [8, 9]. The primary reason of this success was the fabrication of ultrafine, monosized, and low agglomerated  $\text{Lu}_2\text{O}_3$  nanopowders by solution precipitation.

Many reports have prepared  $\text{Lu}_2\text{O}_3$  nanopowders by solution precipitation methods using various precipitants, e.g., ammonium hydroxide ( $\text{NH}_4\text{OH}$ ) [10], ammonium hydrogen carbonate ( $\text{NH}_4\text{HCO}_3$ ) [10, 11], and oxalic acid ( $\text{H}_2\text{C}_2\text{O}_4$ ) [11]. However, the local heterogeneous distribution of precipitants and lutetium ions during the precipitation process can lead to the precipitation of highly agglomerated  $\text{Lu}_2\text{O}_3$  nanoparticles with a relatively broad size distribution. This problem can be solved through the use of a precipitant that can generate slowly precipitating ligands simultaneously and uniformly throughout the solution.

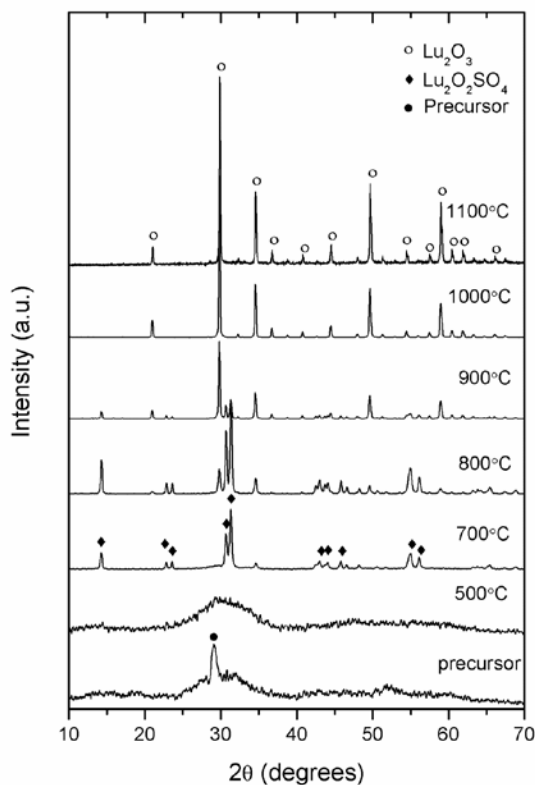


**Figure 2. X-ray diffraction patterns of the precipitate precursor and the Er-doped  $\text{Lu}_2\text{O}_3$  nanopowders calcined at various temperatures for 4 hours.**

Hexamethylenetetramine (HMT) can release precipitating ligands at elevated temperature by decomposing into ammonia and formaldehyde, causing an increase in the solution pH. The slow decomposition of HMT minimizes the local heterogeneous distribution of the precipitating ligands ( $\text{OH}^-$ ) and hence improves the uniformity of precursor particles [12, 13]. Furthermore, conventional starting salts, i.e., nitrate salts, chloride salts, and sulfate salts, also effect the rare-

earth oxide powder properties. For  $\text{Sc}_2\text{O}_3$  nanopowders synthesis, the use of the sulfate salt as a starting material leads to well-dispersed  $\text{Sc}_2\text{O}_3$  nanopowders, whereas hard-aggregated powders are formed with the use of the nitrate salt as a starting material. Since  $\text{SO}_4^{2-}$  has a higher coordination capability than does  $\text{NO}_3^-$ , sulfates show stronger complexing effects, which leads to the formation of a more loosely agglomerated scandium basic sulfate precursor. The basic sulfate precursor can be converted to well-dispersed  $\text{Sc}_2\text{O}_3$  nanopowders after calcination [12].

Presented in this section is the fabrication of loosely-agglomerated Er-doped  $\text{Lu}_2\text{O}_3$  nanopowders by a solution precipitation method using Er-doped lutetium sulfate solution and HMT as a precipitant. The powders were compacted and sintered into transparent Er-doped  $\text{Lu}_2\text{O}_3$  ceramics by vacuum sintering and subsequently hot isostatic pressing (HIP) and their optical properties are reported.

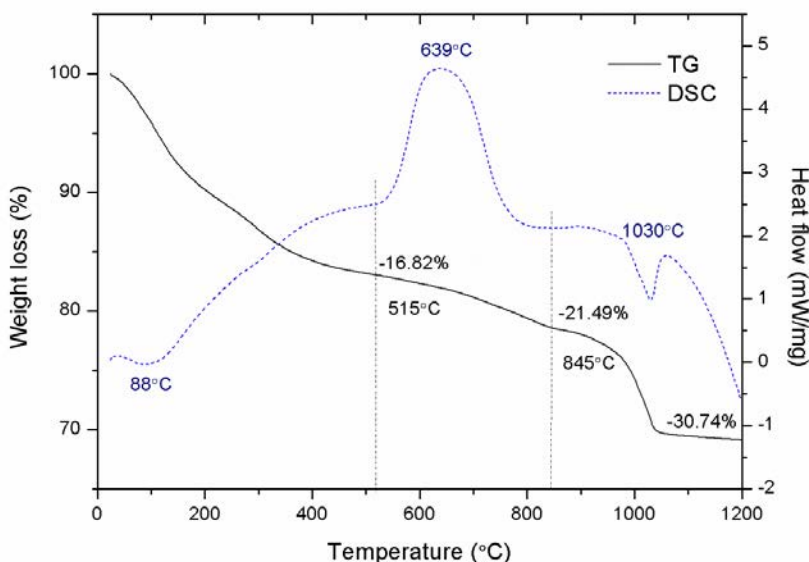


**Figure 3. TG/DTA curves of the precipitate precursor.**

### **Selected Procedures**

In this study, 0.25 atom percent Er-doped  $\text{Lu}_2\text{O}_3$  nanopowders were synthesized by a co-precipitation technique. A lutetium nitrate solution was prepared by dissolving  $\text{Lu}_2\text{O}_3$  powder in excess amounts of nitric acid at approximately 80 °C. Erbium nitrate pentahydrate (Acros Organics, 99.9%, Fair Lawn, NJ) was added into the lutetium nitrate solution according to the formula 0.25 at% Er-doped  $\text{Lu}_2\text{O}_3$ . A 100 ml of 1.0 M ammonium hydroxide was dripped into a 100 ml of 0.2 M Er-doped lutetium nitrate solution at a rate of about 5 ml/min in order to precipitate Er-doped lutetium hydroxide. After homogenizing for an hour, the hydroxyl precipitates were separated by centrifugation and then washed several times with water to remove impurities. The Er-doped lutetium sulfate was prepared by dissolving the hydroxyl precipitates with a stoichiometric amount of sulfuric acid. The Er-doped  $\text{Lu}_2\text{O}_3$  nanopowders were prepared by dripping a 100 ml of 2.0 M HMT solution into the 100 ml of 0.1 M Er-doped

lutetium sulfate solution at a rate of about 5 ml/min under mild stirring at 80 °C. After homogenizing for an hour, the precipitates were washed several times with water and dried in vacuum oven at 70 °C. The precursors were calcined at various temperatures for 4 hours under flowing oxygen gas at 3 l/min to produce Er:Lu<sub>2</sub>O<sub>3</sub> nanopowders.

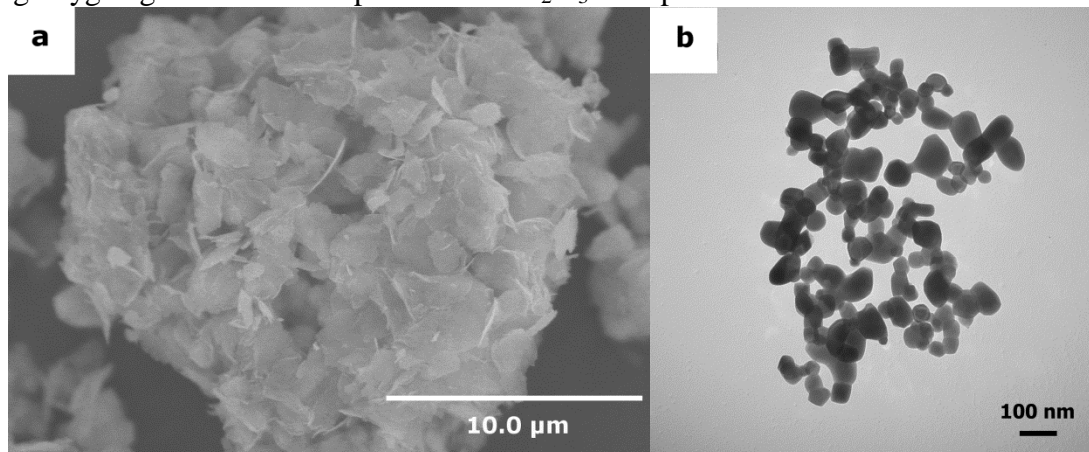


**Figure 4. (a) SEM image showing morphology of the precipitate precursor (b) TEM image showing Er-doped Lu<sub>2</sub>O<sub>3</sub> nanoparticles calcined at 1100 °C for 4 hours.**

Thermal decomposition and phase evolution of the precursors were investigated using simultaneous thermal analysis (STA; STA449C, Netzsch, Germany), X-ray diffraction (XRD; XDS 2000, Scintag, Cupertino, CA), and Fourier transformed infrared spectrometry (FTIR; Nicolet 6700 FT-IR, Thermo Scientific, Waltham, MA). The morphology of Lu<sub>2</sub>O<sub>3</sub> nanopowders was observed using transmission electron microscopy (TEM; model H7600T, Hitachi, Pleasanton, CA) and scanning electron microscopy (SEM; model 4800, Hitachi, Pleasanton, CA). The average particle size was determined by averaging diameter of approximately 200 particles from TEM images.

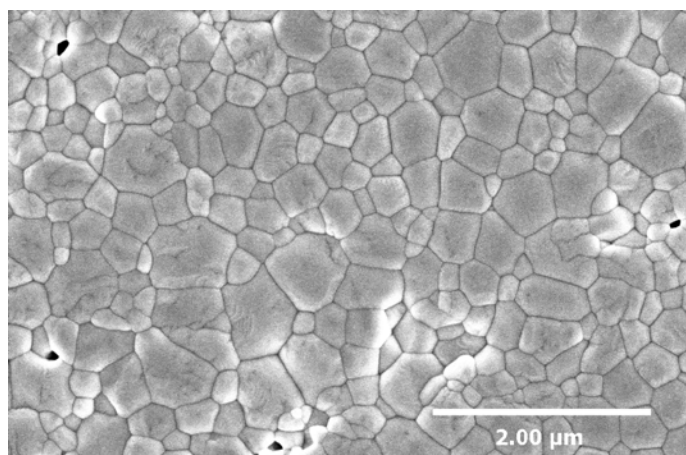


**Figure 5. SEM image showing microstructure of the two-step sintered ceramic.**

The calcined nanopowders were uniaxially pressed into pellets of 13 mm in diameter and 1 mm in thickness at approximately 15 MPa without any binder and then cold isostatically pressed under a pressure of 200 MPa. The green density of pellets was about 50%. The green pellets were sintered using a two-step sintering technique under a vacuum of less than about 10<sup>-3</sup> Pa in

order to limit grain growth [14, 15]. In two-step sintering, the samples were heated from room temperature to 1600 °C. The temperature was then immediately decreased to 1500 °C and held for 20 hours in order to obtain close porosity before naturally cooling down to room temperature. The samples were subsequently hot isostatically pressed at 1700 °C in an Ar pressure of 206 MPa for 8 hours.

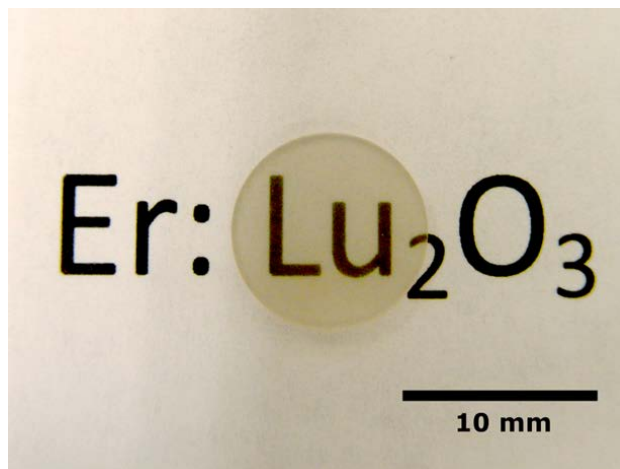


**Figure 6.** Optical image of the polished sintered Er-doped  $\text{Lu}_2\text{O}_3$  ceramic.

The sintered samples were mechanically polished using 600, 800, and 1200 grit silicon carbide papers. Final polishing was performed with colloidal silica suspension. The microstructure of sintered samples was observed by a field-emission scanning electron microscopy (FE-SEM; model 4800, Hitachi, Pleasanton, CA). The average grain size of the sintered samples was determined from SEM images using the lineal intercept method following ASTM E112-96. An optical transmittance of the sintered ceramics was measured over the wavelength region from 200 to 2000 nm using a UV-VIS spectrometer (Perkin Elmer UV/VIS/NIR Lambda 900, Norwalk, CT) at normal incidence. The samples thickness was about 1 mm.

## Results and Discussion

### *Powder characterization*

Figure 1 shows the FTIR spectra of the precipitate precursor and the Er-doped  $\text{Lu}_2\text{O}_3$  nanopowders calcined at various temperatures for 4 hours. The precipitate precursor shows the absorption of a hydrated sulfate compound. The broad absorption centered at  $3350\text{ cm}^{-1}$  is attributed to O-H stretching of molecular water whereas the peak at  $1643\text{ cm}^{-1}$  is due to H-O-H bending mode. The broad peaks centered at  $1075$  and  $604\text{ cm}^{-1}$  are the absorption peaks of  $\text{SO}_4^{2-}$ . Calcining at  $700^\circ\text{C}$  for 4 hours decreases the OH absorption bands while those of  $\text{SO}_4^{2-}$  are split into several peaks. The absorption peaks at  $1226$ ,  $1130$ , and  $1056\text{ cm}^{-1}$  are due to antisymmetric stretch vibration modes of  $\text{SO}_4^{2-}$  tetrahedra. The absorption peak at  $1006\text{ cm}^{-1}$  is attributed to a symmetric stretch vibration mode of  $\text{SO}_4^{2-}$ . The absorption peaks at  $675$  and  $611\text{ cm}^{-1}$  are associated with antisymmetric bending vibration modes of  $\text{SO}_4^{2-}$  [16]. The splitting of the broad absorption bands indicates the rearrangement of the structure. All these absorption peaks disappear after calcining at  $1100^\circ\text{C}$  for 4 hours indicating the complete decomposition of the hydroxide and the sulfate. Furthermore, the presence of the absorption peak at  $\sim 570\text{ cm}^{-1}$  after calcining at  $1100^\circ\text{C}$  for 4 hours is attributed to the stretching of Lu-O bond [8].

The x-ray diffraction patterns of the precipitate precursor and the Er-doped  $\text{Lu}_2\text{O}_3$  nanopowders calcined at various temperatures for 4 hours are shown in Fig. 2. The x-ray diffraction pattern of the precipitate precursor exhibits very broad peaks indicating poor crystallinity. The poor crystallinity precursor transforms to a  $\text{Lu}_2\text{O}_2\text{SO}_4$  phase (JCPDS card no. 53-0166) after calcining at 700 °C for 4 hours. The narrower XRD peak linewidths confirm the higher degree of crystallinity of the  $\text{Lu}_2\text{O}_2\text{SO}_4$  phase. After calcining at 800 °C for 4 hours, the  $\text{Lu}_2\text{O}_2\text{SO}_4$  phase has partially converted to a cubic crystalline  $\text{Lu}_2\text{O}_3$  phase (JCPDS card no.86-2475) and fully converted to a pure  $\text{Lu}_2\text{O}_3$  phase after calcining at 1100 °C for 4 hours.

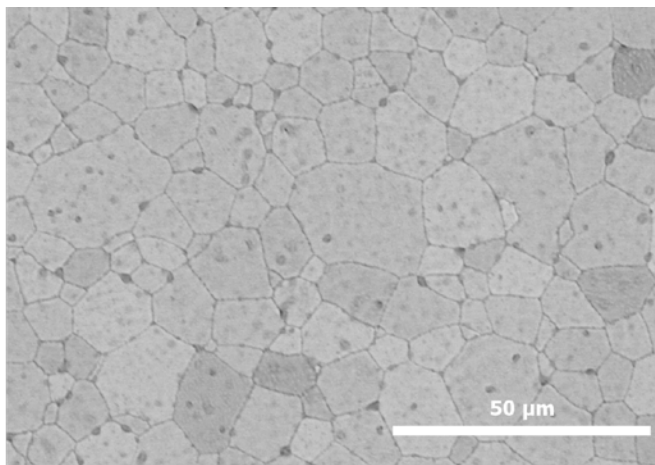


**Figure 7. SEM image showing microstructure of the transparent Er-doped  $\text{Lu}_2\text{O}_3$  ceramic after hot isostatic pressing at 1700°C for 8 hours.**

Figure 3 shows TG/DTA curves of the precipitate precursor. The hydrated lutetium sulfate compound decomposes to  $\text{Lu}_2\text{O}_3$  through 3 major steps. The weight loss (-16.82%) and the broad endothermic peak below 515 °C are attributed to the evaporation of adsorbed moisture and molecular water. The exothermic peak centered at 639 °C is due to the formation of the  $\text{Lu}_2\text{O}_2\text{SO}_4$  phase as is shown in XRD and FTIR results. The weight loss (-30.74%) occurring above about 845 °C and the endothermic peaking at 1030 °C are caused by desulfurization as the  $\text{Lu}_2\text{O}_2\text{SO}_4$  phase converts to  $\text{Lu}_2\text{O}_3$  phase.

Figure 4 shows morphologies of the precipitate precursor and the Er-doped  $\text{Lu}_2\text{O}_3$  nanopowder calcined at 1100 °C for 4 hours. The precipitate precursor consists of flakey particle agglomerates (Fig. 4(a)). The flake particles collapse into nanoparticles after calcining at 1100 °C for 4 hours. The nanoparticles are loosely agglomerated and uniform in size with an average particle size of  $60 \pm 16$  nm (Fig 4(b)).

#### *Fabrication and optical properties of transparent Er-doped $\text{Lu}_2\text{O}_3$ ceramics*

The nanopowder calcined at 1100 °C for 4 hours was used for the fabrication of transparent ceramics. The powder compact was sintered using two-step sintering as describe above. Two-step sintering permits densification at lower temperatures, compared with conventional sintering. Hence, the residual pores are maintained at grain boundaries and triple junctions as shown in Fig 5 , which can more readily be eliminated during subsequently hot isostatic pressing [17]. The as-sintered ceramic achieved about 99% of theoretical density with an average grain size of  $0.55 \pm$

0.08  $\mu\text{m}$ . The transparent Er-doped  $\text{Lu}_2\text{O}_3$  ceramic was obtained after hot isostatic pressing the two-step sintered ceramic at 1700  $^\circ\text{C}$  for 8 hours in an Ar pressure of 206 MPa. The transparency of the ceramic is such that letters can be easily read through a 1-mm-thick pellet, as is shown in Fig 6. However, extensive grain growth was observed (Fig. 7). The average grain size of the transparent ceramic was  $15.9 \pm 2.3 \mu\text{m}$ . Dark spots also were observed in the SEM images. The chemical composition of the dark spots was investigated using energy dispersive x-ray spectroscopy (EDX), which indicated that the chemical composition of the dark spots was similar to that of Er-doped  $\text{Lu}_2\text{O}_3$  grains. The reason of the dark spot appearance is unclear and need to be further investigated.

The optical transmittance of the transparent Er-doped  $\text{Lu}_2\text{O}_3$  ceramic is shown in Fig. 8. The calculated maximum transmission, based on the refractive index reported by Kaminskii, et al., [18] is also included in Fig 8. The absorption peaks at about 380, 524, and 1538 nm are due to the absorption transition of  $\text{Er}^{3+}$  ions. The optical transmittance of the transparent Er-doped  $\text{Lu}_2\text{O}_3$  ceramic is about 78% at the wavelength of 1.55  $\mu\text{m}$ , which is the main emission of interest from  $\text{Er}^{3+}$ . The optical transmittance is lower at the shorter wavelength due to the scattering of the residual pores in microstructure.

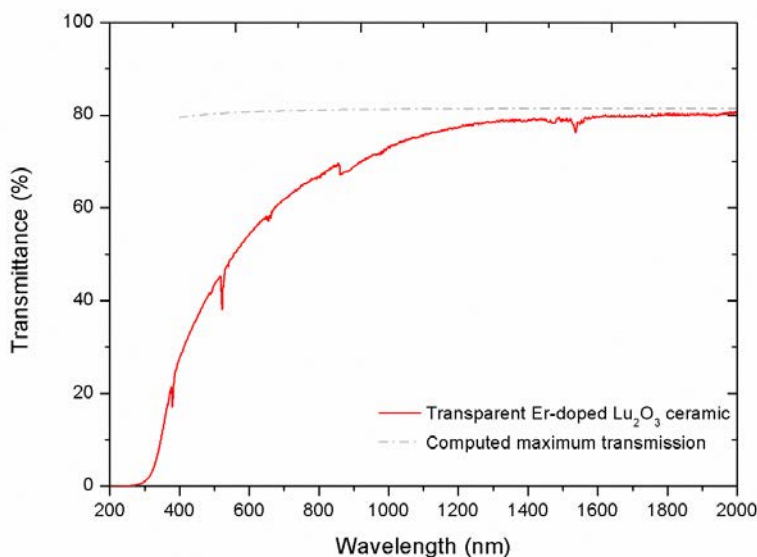


**Figure 8. The optical transmittance of the transparent Er-doped  $\text{Lu}_2\text{O}_3$  ceramic.**

### Section Conclusions

In the present work, Er-doped  $\text{Lu}_2\text{O}_3$  nanopowders were obtained by calcining a precipitate precursor precipitated from lutetium sulfate solution with HMT at 1100  $^\circ\text{C}$  for 4 hours. The nanopowders were loosely agglomerated with an average particle size of 60 nm. Transparent Er-doped  $\text{Lu}_2\text{O}_3$  ceramics were fabricated from the nanopowders by hot isostatic pressing two-step sintered ceramics at 1700  $^\circ\text{C}$  for 8 hours. The optical transmittance of the transparent ceramics reaches about 78% at 1.55  $\mu\text{m}$ . However, the optical transmittance decreases at the shorter wavelength due to the scattering of remnant porosity which will be a subject of continued optimization.

## Section References

- [1] A. Lempicki, C. Brecher, P. Szupryczynski, H. Lingertat, V.V. Nagarkar, S.V. Tipnis, S.R. Miller, Nucl. Instrum. Meth. A, 488 (2002) 579-590.
- [2] J. Lu, K. Takaichi, T. Uematsu, A. Shirakawa, M. Musha, K. Ueda, H. Yagi, T. Yanagitani, A.A. Kaminskii, Appl. Phys. Lett., 81 (2002) 4324-4326.
- [3] L.Q. An, J. Zhang, M. Liu, S.W. Wang, J. Am. Ceram. Soc., 88 (2005) 1010-1012.
- [4] Q.W. Chen, Y. Shi, J.Y. Chen, J.L. Shi, J. Mater. Res., 20 (2005) 1409-1414.
- [5] V. Lupei, A. Lupei, A. Ikesue, J. Alloys Compd., 380 (2004) 61-70.
- [6] A.A. Kaminskii, M.S. Akchurin, R.V. Gainutdinov, K. Takaichi, A. Shirakawa, H. Yagi, T. Yanagitani, K. Ueda, Crystallogr. Rep., 50 (2005) 869-873.
- [7] J.R. Lu, K. Takaichi, T. Uematsu, A. Shirakawa, M. Musha, K. Ueda, H. Yagi, T. Yanagitani, A.A. Kaminskii, Jpn. J. Appl. Phys., 41 (2002) L1373-L1375.
- [8] Q.W. Chen, Y. Shi, L.Q. An, J.Y. Chen, J.L. Shi, J. Am. Ceram. Soc., 89 (2006) 2038-2042.
- [9] D. Zhou, Y. Shi, J.J. Xie, Y.Y. Ren, P. Yun, J. Am. Ceram. Soc., 92 (2009) 2182-2187.
- [10] D. Zhou, Y. Shi, P. Yun, J.J. Xie, J. Alloys Compd., 479 (2009) 870-874.
- [11] Z.F. Wang, W.P. Zhang, B.G. You, M. Yin, Spectrochim. Acta A, 70 (2008) 835-839.
- [12] J.G. Li, T. Ikegami, T. Mori, Y. Yajima, J. Am. Ceram. Soc., 87 (2004) 1008-1013.
- [13] P.L. Chen, I.W. Chen, J. Am. Ceram. Soc., 76 (1993) 1577-1583.
- [14] X.H. Wang, P.L. Chen, I.W. Chen, J. Am. Ceram. Soc., 89 (2006) 431-437.
- [15] I.W. Chen, X.H. Wang, Nature, 404 (2000) 168-171.
- [16] M.d.F.V. de Moura, J.d.R. Matos, R.F. de Farias, Thermochim. Acta, 414 (2004) 159-166.
- [17] K. Serivalsatit, J. Ballato, J. Am. Ceram. Soc., 93 (2010) 3657-2662.
- [18] A.A. Kaminskii, M.S. Akchurin, P. Becker, K. Ueda, L. Bohaty, A. Shirakawa, M. Tokurakawa, K. Takaichi, H. Yagi, J. Dong, T. Yanagitani, Laser Phys. Lett., 5 (2008) 300-303.

## Section VI. On the Fabrication of All-Glass Optical Fibers from Crystals

### Section Summary

The highly non-equilibrium conditions under which optical fibers conventionally are drawn afford considerable, yet under-appreciated, opportunities to realize fibers comprised of novel materials or materials that themselves cannot be directly fabricated into fiber form using commercial scalable methods. Presented here is an in-depth analysis of the physical, compositional, and selected optical properties of silica-clad erbium-doped yttrium aluminosilicate glass optical fibers derived from undoped, 0.25, and 50 weight % Er<sup>3+</sup>-doped YAG crystals. The YAG-derived fibers were found to be non-crystalline as evidenced by x-ray diffraction and corroborated by spectroscopic measurements. Elemental analysis across the core/clad interface strongly suggests that diffusion plays a large role in this amorphization. Despite the non-crystalline nature of the fibers, they do exhibit acceptable low losses (~ 0.15 – 0.2 dB/m) for many applications, broad-band emissions in the near-infrared, and enhanced thermal conductivity along their length while maintaining equivalent mechanical strength with respect to conventional silica optical fibers. Further, considerably higher rare-earth doping levels are realized than can be achieved by conventional solution or vapor-phase doping schemes. A discussion of opportunities for such approaches to non-traditional fiber materials is presented.

### Introduction

The vast majority of optical fiber is made from combinations of core and clad compositions that are variations on the same theme. In other words, the cladding and core are essentially the same material but with a minor compositional perturbation to adjust the refractive indices to permit light confinement and guidance. Such similarities between core and clad materials yield additional benefits such as amenability to co-drawing and well-matched expansion coefficients. However, using the same family of core and clad materials severely restricts the choice of materials from which fibers can be made. Over the years, there have been occasional successes in fabricating optical fibers comprised of considerably dissimilar materials including all-glass fibers [1,2,3], crystalline fibers [4,5], and glass-clad, crystal core fibers.[6,7] However, the trend within the optical fiber community has been more focused on developing fiber geometries of ever-greater complexity than on new combinations of materials that could enable addition and value-added optical and optoelectronic functions.

This paper provides a thorough materials characterization of optical fibers prepared from a crystalline starting material for the core; specifically Er<sup>3+</sup>-doped YAG. The choice of Er:YAG was due to recent work using conventional fiber draw techniques to make glass-clad fibers with cores purportedly containing (chromium doped) YAG.[8,9] In those reports, a single crystal of (Cr doped) YAG was sleeved inside a silica glass tube and drawn into fiber using a conventional fiber draw approach. The core material is molten at the temperature where the glass capillary tube (and optical cladding) softens. As the fiber is drawn and cools, there is hope that the melt might crystallize into a YAG core as it solidifies.

In the present work, silica glass-clad fibers of varying diameters were drawn from preforms containing undoped and erbium-doped YAG single crystals in the core. These preforms were drawn into fiber at temperatures above the melting point of the YAG core crystal. X-ray diffraction was used as the primary tool to examine crystallinity in the resultant fiber core. Optical absorption and emission measurements of rare-earth-doped fiber samples were made to provide a secondary indication of crystallinity since spectral linewidths broaden in amorphous hosts. Diffusion from cladding to core, which is likely at the high draw temperatures, was investigated using EDX for elemental analysis. Lastly, since the ultimate goal is the practical use of the fiber, both the strength and the thermal conductivity of the drawn fibers - properties important for high-power amplifier applications – were studied.

Although our initial hope was that the fibers would possess some degree of YAG crystallinity, the resultant cores were found to be a fully amorphous yttrium-alumino-silicate glass. However, the fibers did exhibit beneficial physical and optical properties that make them of potential interest as optical amplifiers and lasers. The results are insightful into how this molten core process can be a valuable processing approach to realizing optical fibers with cores comprising materials that are either highly dissimilar from the cladding or would not themselves be amendable to the direct fabrication into fiber form.

## **Experimental Procedures**

Commercial grade single crystals of YAG (undoped, 0.25 wt.% Er doped, and 50 wt.% Er doped) for use in the core of the preforms were provided by Northrop Grumman Synoptics (Charlotte, NC). The YAG boule was core-drilled (Ceramare, Piscataway, NJ) into rods

measuring 3 mm in diameter and approximately 40 mm in length. Optical quality silica glass (F300) for use as the cladding was purchased from Heraeus Tenevo (Buford, GA).

A series of the silica glass capillary tubes were drawn to differing sizes and sleeved within one another to yield a preform having an outer diameter of 51 mm and an inner diameter of 3 mm. This preform was then fire polished using an internal procedure. The YAG core rod then was placed in the center of the capillary cladding glass preform.

For each of the YAG compositions (undoped, 0.25 and 50% Er:YAG) from which the preform was prepared a series of large fibers (canes) were drawn to varying diameters in order to quantify diffusion effects on the core composition. Following the collection of these canes, each YAG-derived fiber was drawn down to 125  $\mu\text{m}$ , coated with a single layer of UV curable polymer (DSM Desolite 3471-3-14), and about 1 km was collected on a spool for a variety of subsequent measurements. All fibers were drawn at approximately 2025  $^{\circ}\text{C}$  using the Heathway fiber draw tower at Clemson University.

#### *X-Ray Diffraction*

Powder x-ray diffraction patterns were collected using a Scintag XDS 2000-2 powder diffractometer with Cu  $K\alpha$  radiation ( $\lambda = 1.5418 \text{ \AA}$ ) and a solid-state Ge detector. Diffraction patterns were collected from 5-65 $^{\circ}$  in 2-theta in 0.03 $^{\circ}$  steps at rates of 2-10 seconds per step. Samples were analyzed both as intact fibers and as pulverized powders. Further, in some cases both the core and the silica cladding were analyzed and in selected cases, the silica cladding was partially removed by etching in dilute HF acid.

#### *Microscopic and Elemental Analysis*

Prior to examination the fiber ends were mechanically polished with 600 grit silicon carbide (SiC) bonded paper. Un-coated samples were investigated using a Hitachi 3400N scanning electron microscope (SEM). Energy Dispersive X-ray Spectroscopy (EDX) was performed to examine the distribution of major elements (Si, O, Al, Y and Er). Elemental compositions were measured at several locations along a line traversing the core. The microscope was operated at 20 or 30 kV and 10 mm working distance under variable pressure. EDX typically has a spatial resolution of about 1  $\mu\text{m}$ .

#### *Fiber Attenuation and Spectroscopic Measurements*

Baseline fiber attenuation measurements were performed using a Photon Kinetic 2500 Optical Fiber Analysis System. In this case the attenuation wavelength dependence was measured with 10 nm wavelength increments. A 5 and 10 meter cut-back length was used for the fiber drawn using the undoped YAG crystal and 0.25 weight percent erbium doped YAG crystal, respectively.

In order to characterize the fibers spectroscopically, with the purpose of determining whether they have crystalline or amorphous structure, significantly higher (than 10 nm) spectral resolution is required. For this purpose fiber absorption was measured by using the standard “cut-back” technique, whereby the light from the fiber-coupled “white light” source (Yokogawa AQ4305 White Light Source) transmitted through the fiber under investigation was spectrally

analyzed by the AQ6370 optical spectrum analyzer (OSA). Spectrally dispersed, with the 1 nm OSA resolution, light intensities (log scale) separately measured on the samples of 2.688 m and 0.653 m long were subtracted and then divided by the differential length (2.035 m “cutback”) in order to infer the true dB/m core absorption value.

The  $^4I_{13/2} - ^4I_{15/2}$   $\text{Er}^{3+}$  fluorescence spectra were measured using an Acton 2500i monochromator, thermoelectrically cooled InGaAs detector and lock-in amplifier. The monochromator slits were chosen to provide a resolution better than 0.35 nm. Fluorescence was always collected perpendicular to the fiber axis. This collection mode, even though it does not offer a higher signal-to-noise ratio, does avoid spectral distortions due to fluorescence emission re-absorption of waveguided light. It also helps to avoid systematic errors in lifetime measurements associated with fluorescence radiation trapping. All obtained spectra were corrected for the spectral response of the entire system. For spectral scanning fluorescence was excited by electrically chopped 976-nm fiber coupled GaAs diode laser. The same setup was utilized for fluorescence lifetime measurements, except a short-pulse (~10-ns) excitation source, frequency-doubled Nd:YAG laser at 532 nm, was used in this case. Time resolution for the lifetime measurements was 3  $\mu\text{s}$ . The lifetime was measured by a Tektronix digital oscilloscope with the averaging used for signal-to-noise improvement.

#### *Thermal Conductivity Measurements*

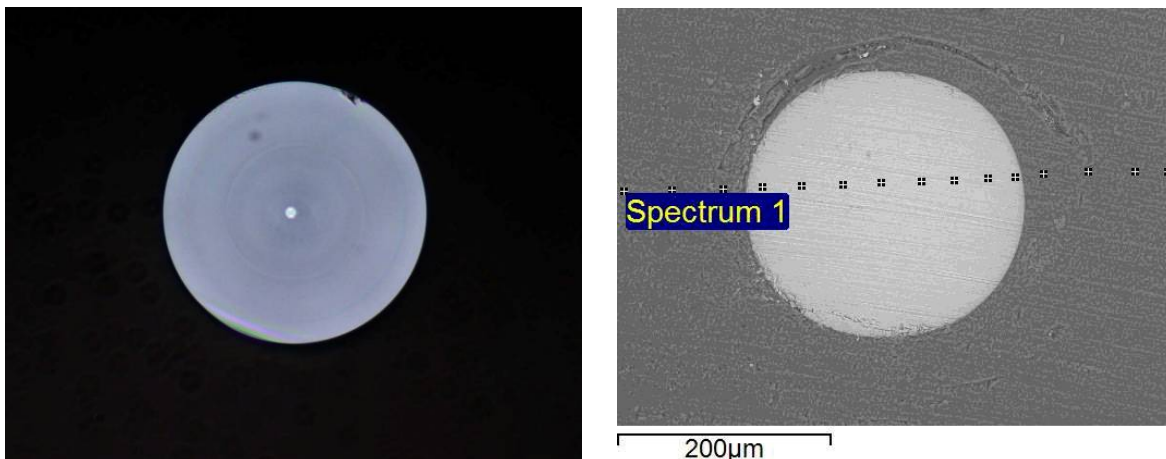
The geometry and size of optical fibers is not conducive to conventional four-probe steady state thermal conductivity measurement methods. Therefore, the Parallel Thermal Conductance, or PTC, system was used to measure the thermal conductance along the length of the samples at temperatures ranging from 10K to room temperature.[ ] Samples were cooled with a cryo-cooler to the desired temperature set by the user at an adjustable cooling rate then warmed up while the system begins to take the data with preset temperature intervals. For the optical fibers discussed here, the cooling rate was 1 K/min and the samples were mounted on the stage with Ag paste (DuPont 4924N).

#### *Fiber Strength Measurements*

It is well known that any crystallization in glasses can dramatically decrease the strength since it leads to sharp features that are effective stress concentrators. Fused silica optical fiber must be strong in order to survive the stresses it experiences during component fabrication and during service. Typical fiber is very strong (~5 GPa) but occasional weak defects are removed by proof testing at typically 350 or 700 MPa. Any crystallization in the fiber could degrade the strength below the proof stress and so would make the fiber unusable in conventional component designs. The mechanical properties of the fibers described here have therefore been characterized using industry standard test methods using both two-point flexure[ ] and uniaxial tension.[ ] Fused silica exhibits fatigue or stress corrosion cracking due to environmental moisture. For this reason all measurements have been made in a controlled environment at  $23.0 \pm 0.2^\circ\text{C}$  and  $50 \pm 3\%$  humidity.

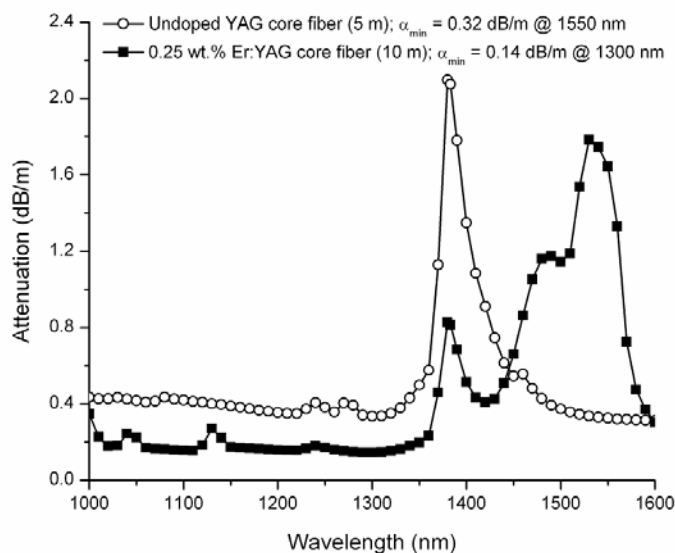
## **Results and Discussion**

Figure 1 provides an optical micrograph of the conventional (125  $\mu\text{m}$ ) fiber after fabrication. As can be seen, the core is central, circular, and guides light. The concentric cladding tubes that had been layered to provide the desired core/clad ratio were well-fused.



**Figure 1. Optical (left) and electron microscopic (right) image of different representative fibers drawn from a YAG starting core crystal. The optical micrograph (left) is of a fiber with a 125 μm outer diameter. The electron micrograph (right) is of a fiber drawn to a diameter such that the core was about 250 μm. The points marked across the core region (right) indicate where elemental analysis was performed (see Figures 6 – 8).**

Earlier iterations led to non-circular cores which most likely were due to ovalities in the starting cladding tubes. Since the core is molten at the draw temperatures, it would tend to flow and take on the shape of its “container.” Light from a He-Ne laser (632.8 nm) propagated through a several meter length of 125 μm diameter fiber exhibited a far-field pattern consistent with a low-moded fiber ( $4 < V < 6$ ) with an NA of approximately 0.38 and  $\Delta n \sim 0.049$ . Given that the index of the core precursor YAG crystal exceeds 1.8 the measured NA clearly indicates a considerable amount of diffusion from the silica cladding into the (molten) core during draw. This is quantified in greater detail later in this paper.



**Figure 2. Spectral attenuation of the undoped and lightly-doped (0.25 wt.% Er:YAG in the preform) “YAG”-core fiber. Absorption band peaked at 1385 nm is due to OH groups in the as-grown crystal.**

In order to make an estimation of the spectral attenuation, a cut-back measurement was made using a Photon Kinetics 2500 unit on selected lengths of 125  $\mu\text{m}$  undoped and 0.25 wt.% doped fiber. The results are shown in Figure 2. A 5 m length of the undoped fiber exhibited a minimum loss (background attenuation) of about 0.33 dB/m at a wavelength of 1300 nm (where there is no OH or  $\text{Er}^{3+}$  absorption lines). A 10 m length of the lightly-doped fiber exhibited a lower loss: about 0.14 dB/m at a wavelength of 1300 nm. These loss values are roughly 100 times lower than those achieved in Ref. 8 for a Cr-doped analog. The absorption due to the erbium dopant also is observed and is discussed in more detail below. In both cases, the peak at approximately 1385 nm is due to residual OH in the as-grown crystal from which the core rod was cut.

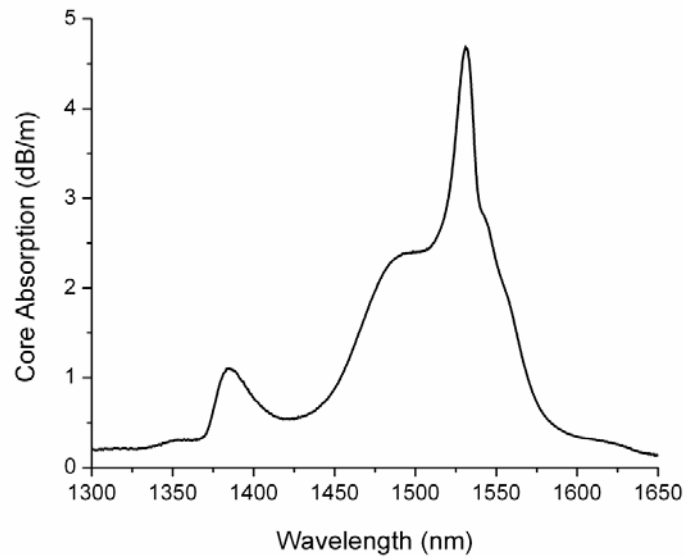


**Figure 3. Core absorption spectrum of the fiber drawn from the preform containing a 0.25 wt.% Er:YAG crystal; 1 nm spectral resolution. Absorption peak at 1385 nm is also attributed to residual water absorption from the as-grown crystal.**

A higher resolution absorption spectrum for the fiber made from the 0.25 wt. % Er:YAG is shown in Figure 3. The figure is indicative of about 4.5 dB/m  $\text{Er}^{3+}$  peak core absorption (above the  $\sim 0.15\text{-}0.2$  dB/m background transmission loss) at 1532.5 nm for this low concentration fiber. The observed difference between the relatively low peak absorption values ( $\sim 1.6$  dB/m) in the Photon Kinetics 2500 attenuation measurement (Figure 2) and true absorption measurements (Figure 3) can be attributed to the highly under-resolved nature of the former. This difference is, as expected, the most prominent for the sharpest and narrowest 1532.5 nm absorption peak. Better resolution of the “cutback” measurement allows observation of the true spectral width of the major Er absorption peak in the fiber as well as any spectroscopic fine structure on the long-wavelength side of the absorption curve.

This is a quite reasonable level of transparency for such a non-optimized initial study. In order to further characterize the optical properties of these fibers, the luminescence spectrum and luminescence lifetime were evaluated.

Figure 4 provides the absorption spectra of the YAG-derived fiber compared to that of single crystalline Er:YAG as well as two erbium doped fiber amplifier (EDFA) fibers. The broad and “smooth” Er<sup>3+</sup> absorption features in the drawn fiber, versus those of the original Er:YAG in the preform, implies a non-crystalline environment in the core of the drawn fiber. However, the observed linewidth is somewhat narrower than that of Er<sup>3+</sup> doped into typical telecom-type alumino- and germano-silicate glass hosts. These features can be seen in Figure 4, which provides the normalized absorption spectra from the fiber derived from the Er:YAG containing preform compared to those from an Er:YAG single crystal and two commercial EDFA fibers.

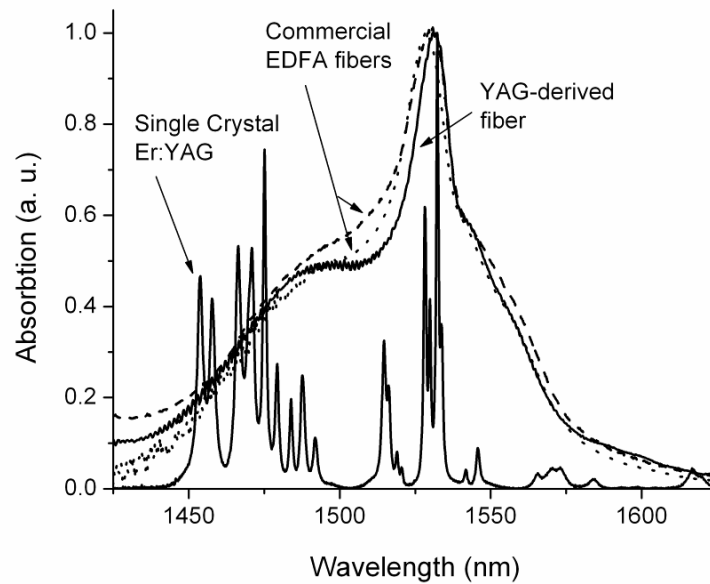


**Figure 4. Normalized absorption spectrum of the optical fiber derived from the Er:YAG containing preform compared to that for a YAG single crystal and two commercial erbium-doped fiber amplifier (EDFA) fibers.**

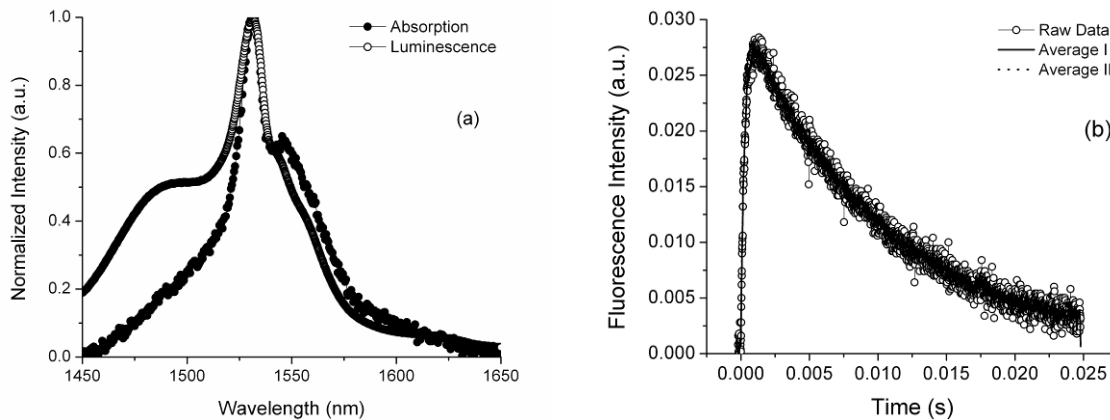


**Figure 5. Spectroscopic properties of the fiber drawn using the 0.25 wt.% Er:YAG crystal in the core: (a) fluorescence corrected for spectral response of the spectrometer overlaid with the absorption of the fiber; (b) fluorescence kinetics of the 0.25 wt.% Er<sup>3+</sup>-doped fiber measured at 1532.5 nm with the ~10-ns pulse excitation at 532 nm.**

Figure 5 provides the normalized  ${}^4I_{13/2} \rightarrow {}^4I_{15/2}$  Er<sup>3+</sup> fluorescence and absorption spectra (Figure 5a) and the measured fluorescence intensity as a function of time (Figure 5b). Like Figure 4, the Figure 5a spectra are indicative of an amorphous structure though the linewidth of the central peak is narrower than found in conventional EDFA glasses. Additionally, the ~ 10 ms first e-folding lifetime from the fiber is somewhat longer than the typical lifetime for Er-doped silica-based glasses. In order to better understand if there were any crystallographic considerations at play, x-ray diffraction and elemental analysis was performed.

Thicker fibers, due to the larger amount of core material relative to a thinner fiber, were analyzed using powder x-ray diffraction. In all cases, the cores were found to be x-ray amorphous. This is in contrast to a previous report in the literature for a fiber fabricated using a fiber draw process[9], which cites results on laser-heated pedestal grown fibers [ ], even though the formation processes and thermal histories are entirely different. The authors note the formation of crystalline  $\gamma$ -Al<sub>2</sub>O<sub>3</sub> having an anomalously large unit cell parameter derived from selected area electron diffraction (0.856 nm versus the accepted value of 0.790 nm), which they attribute to the Cr-doping. Such a large lattice expansion seems unlikely based on the low dopant concentrations reported (0.5 mol %) and the crystallite analyzed is more likely extremely Cr-heavy or an alternative phase. The work does not provide sufficient detail to understand the chemical identity of the observed crystals or how they might result from the composition or fiber fabrication process.

In the present study, a manifestation of the amorphous nature of the core is found in the overlay of the absorption spectra of Er-doped YAG single crystal and Er-doped YAG-derived fibers (Figure 3). Single-crystalline Er:YAG has very sharp, well defined and mostly fully resolved, even at room temperature, absorption peaks which belong to different inter-Stark transitions between the  ${}^4I_{15/2}$  and  ${}^4I_{13/2}$  manifolds of Er<sup>3+</sup> ions in YAG. Meanwhile, Er-doped YAG core fiber exhibits a smooth absorption contour with much less structure, and inter-Stark transitions mostly manifest themselves by little “shoulders” in the wings of the major absorption peak at 1532.5 nm, which is similar to Er-doped glass absorptions.

In order to further understand this, elemental mapping using the electron microscope was performed. The series of squares noted in Figure 1 (right) marks the locations where elemental analysis using Energy Dispersive X-ray Spectroscopy (EDX) was performed. EDX provides the relative amounts of each element present in the region evaluated. Figures 6, 7, and 8 provide the Si, O, Y, Al, and Er elemental profiles across the core and part of the glass cladding from the YAG (Y<sub>3</sub>Al<sub>5</sub>O<sub>12</sub>)-derived fibers at each erbium doping level and a variety of fiber diameters. The specific fiber diameters at which the elemental analysis was performed were chosen arbitrarily.

There are a few interesting points to be made from Figures 6 through 8. First, the presence of silicon (in the form of silica) in the core implies diffusion from the cladding into the core. This is

reasonable to expect since one has a melt (the YAG core) in contact with a soft glass (the silica cladding) at elevated temperatures (~ 2050 °C). Diffusion is a thermally activated process and so the high processing temperatures for silica fibers further facilitates inter-diffusion. Second, the smaller the core, the more silicon (i.e., silica) diffuses in from the cladding. This also is expected: the smaller the fiber, the shorter the diffusion length, the greater the concentration of the solute (diffusing species from cladding) in the solvent (core). Last, the compositional profiles are more step-like than expected for a diffusion-related process. This is likely due to the fiber fabrication process which promotes homogenization of the molten core as it transitions from the bulk preform through the neck down region and into the fiber where the composition is quenched into constancy.

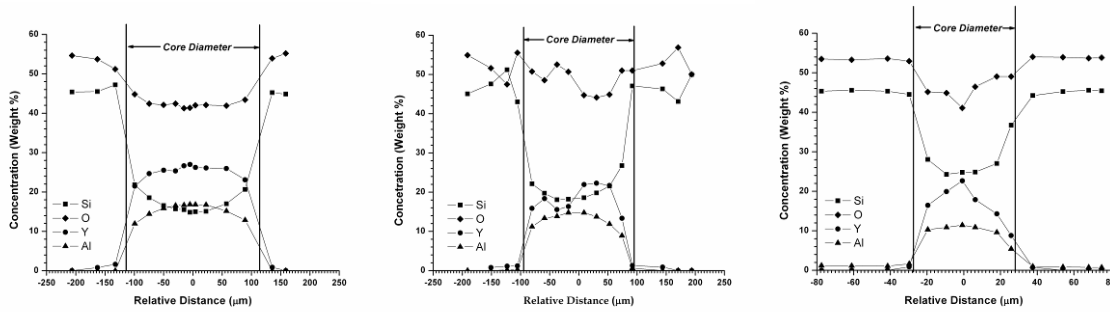


**Figure 6. Elemental profiles (relative elemental composition as a function of position across the fiber) for the undoped fiber. The figures on the left, middle, and right were drawn to core sizes of 230, 191, and 57  $\mu\text{m}$ , respectively.**

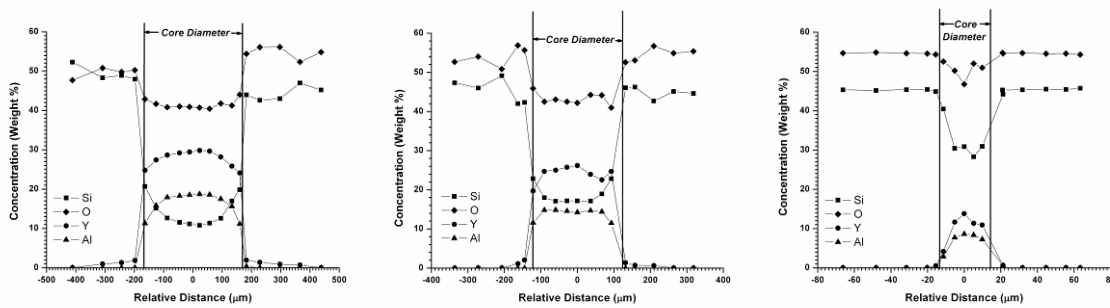


**Figure 7. Elemental profiles (relative elemental composition as a function of position across the fiber) for the for drawn from a preform containing 0.25 weight percent Er:YAG. The figures on the left, middle, and right were drawn to core sizes of 369, 248, and 24  $\mu\text{m}$ , respectively. Note that the erbium concentration is too small to be measurement in this particular experiment.**

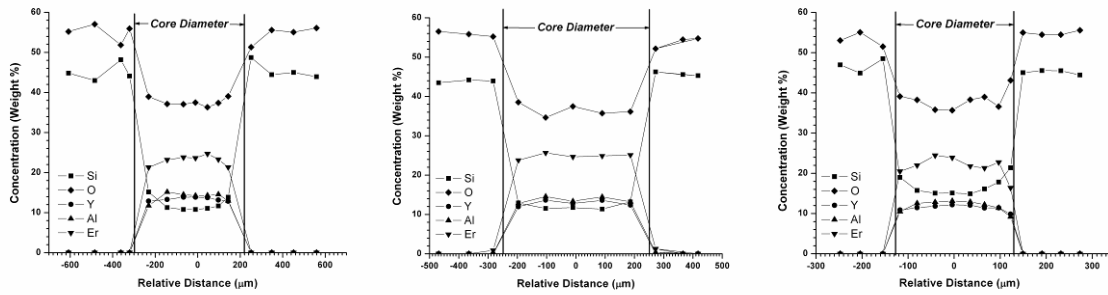


**Figure 8. Elemental profiles (relative elemental composition as a function of position across the fiber) for the fiber drawn from a preform containing 50 weight percent Er:YAG. The figures on the left, middle, and right were drawn to core sizes of 600, 500, and 260  $\mu\text{m}$ , respectively.**

An additional effect of silica diffusion from the cladding is that the core composition is “diluted.” For example, the fiber drawn from a preform containing 50 weight percent Er:YAG exhibited about 20-25 weight percent  $\text{Er}^{3+}$  in the final fiber, depending upon the core size. While this dilution obviously reduces the amount of dopant in the fiber relative to that in the preform, none-the-less there is a considerably higher doping level than could be achieved under the more conventional methods employed to add rare-earths into a fiber; e.g., solution doping and vapor phase doping. Accordingly, this molten core approach could be used to yield doped fibers with unusually high rare earth doping levels; even higher potentially than was achieved in Ref. 2.

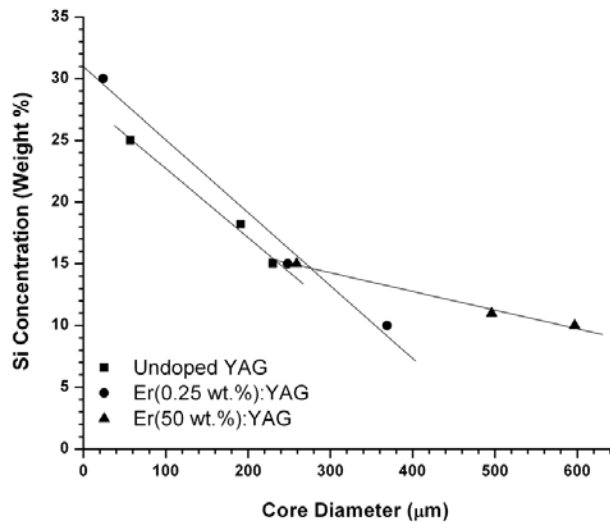


**Figure 9. Silicon concentration (indicating  $\text{SiO}_2$  content) in the center of the fiber core taken from the data of Figures 6 through 8. The lines are guides to the eye.**

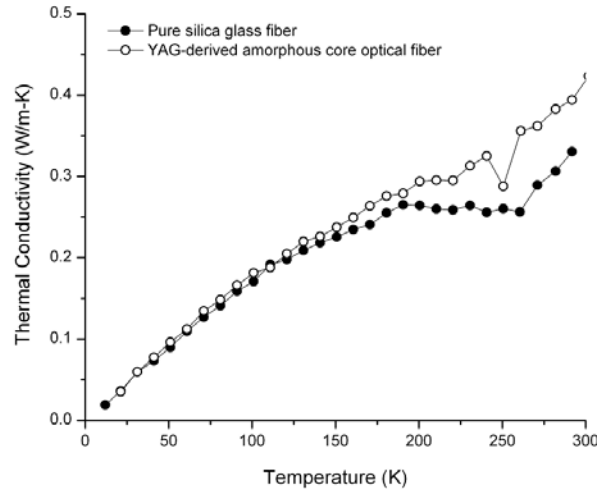


**Figure 10. Thermal conductivity as a function of temperature measured along the fiber length.**

Figure 9 is a compilation of the data from Figures 6 through 8 and shows the concentration of silicon (as silica) at the center of each core of diameter noted. The lines are provided as a guide to the eye and to show trends for the doped and undoped samples. Needless to say, the diffusivity of silica in each composition of molten YAG is slightly different and likely accounts for the measurable differences in concentration. If one were to take an average concentration at each diameter, then the silicon concentration decreases monotonically with increasing core size, hence diffusion length, as would be expected. A more in-depth evaluation of the inter-diffusion between the molten YAG core and the glass cladding is underway and will be reported separately. The purpose here is to provide an initial quantification of the diffusion effects on core composition such that postulations could be made on the crystallography, or lack thereof, in these resultant fibers.

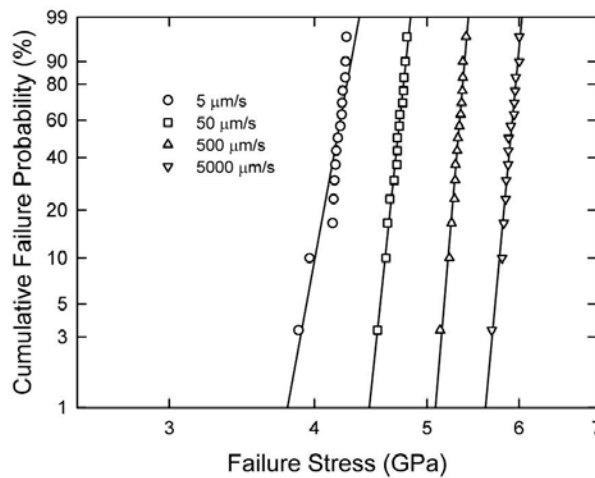


**Figure 11. Weibull probability plot of the strength of undoped fiber measured in two-point bending at four different faceplate speeds.**

Even in the case of the largest core fiber, where the diffusion distance is longest, the center of the core possesses approximately 10 weight percent silicon (as silica) from the cladding. The amorphous nature of the core then is likely due to some combination of two effects: (1) the presence of the silica in the YAG leads to a more stable yttrium aluminosilicate (YAS) glass and (2) the significant quench rate ( $\sim 2000$  °C/s) of the melt to the solid during the fiber fabrication process prevents crystallization of the core. It is more likely that the composition (effect 1) plays the dominant role since equally high quench rates have recently been shown to still permit highly crystalline fibers utilizing similar draw techniques.[7]

Based on this recent success in fabricating crystalline core fibers via fiber draw techniques [7], an original hope for this study was that silica-clad, crystalline YAG core fibers could be realized. This would be of value to higher power amplifiers and lasers where thermal management and heat dissipation is critical. Even though the fibers were found to be amorphous, the thermal conductivity (Figure 10) was measured as a function of temperature along a 4 cm length of the large core fiber. A bare glass silica fiber of equivalent diameter was drawn for direct comparison.

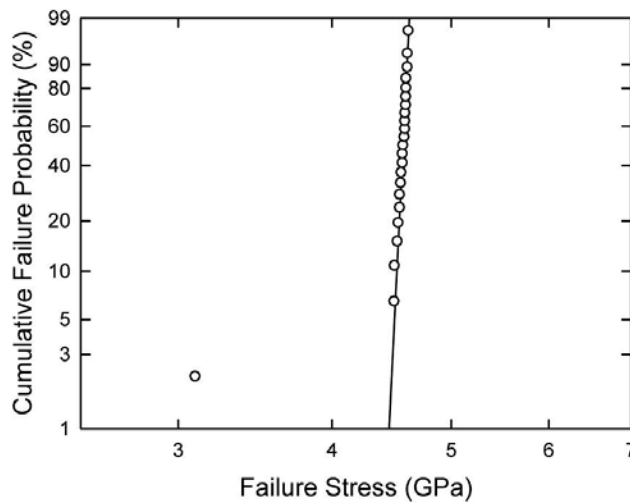


**Figure 12. Weibull probability plot of the strength of fiber drawn from the 50% Er:YAG containing preform measured in uniaxial tension at a stress rate of 30 MPa/s.**

At low temperatures, the fiber derived from the YAG core preform exhibits equal thermal conductivity to that of a conventional silica-based optical fiber. This is not particularly surprising because of the small core-to-clad ratio; hence the fiber is principally silica. However, at temperature approaching room temperature, there is a deviation and the fiber derived from YAG exhibits a thermal conductivity along its length that is  $\sim 20\%$  higher than a conventional silica fiber. The reason for this enhanced thermal conductivity is unclear to date but is reproducible and is a subject for continued study.

In order to fully characterize these fibers, their mechanical properties also were investigated. Figure 11 shows the results of two-point bend strength measurements on the undoped YAG

fiber. The results are graphed on a Weibull probability plot. This plot is widely used to visualize strength distributions. In this case all four distributions are narrow as is typical of fused silica optical fiber. The strength is measured at four faceplate speeds in order to characterize the stress corrosion cracking behavior which occurs in the humid environment. The stress corrosion susceptibility parameter,  $n$ , calculated from these data is 20.9 with a 95% confidence interval of 20.2 to 21.6. Again, this behavior is very typical of fused silica optical fiber.

However, two-point bending is not sensitive to the presence of large defects in the core of the fiber, such as might be produced by crystallization or residual bubbles from the core melt, since the stress at any point in the bent fiber is proportional to the distance from the neutral axis, i.e., the distance from the center of the core. For a  $\sim 6 \mu\text{m}$  diameter core and a  $125 \mu\text{m}$  diameter fiber, the stress at the core/clad interface is only  $\sim 0.05\%$  of the maximum stress at the surface of the fiber. For this reason the strength has been characterized using uniaxial tension using a 0.5 m gauge length in which the entire volume of the fiber is subjected to the same stress. Figure 12 shows the results for the strength of fiber derived from the 50 % Er:YAG measured at a stress rate of 30 MPa/s. Except for one weaker specimen at  $\sim 3 \text{ GPa}$ , the strength distribution is narrow with values typical of fused silica. The broken ends of the weaker specimen were recovered and examined in the optical microscope. The two fracture surfaces were not mirror images of each other meaning the fiber shattered locally at failure, as is typical for strengths above  $\sim 1 \text{ GPa}$ . Fractographic analysis was therefore unable to determine the position of the flaw causing failure. This weaker specimen could have been caused by a defect at the surface of the glass, which can occasionally occur, or at the core/clad interface. In either case the impact on reliability is not great – the strength of 3 GPa is much higher than typical proof stresses (typically 0.36 to 0.72 GPa) so the strength limiting defect would not cause failure during either proof testing or subsequent service. Further, if the flaw is indeed caused by the presence of a defect in the core, it is less severe than a flaw of an equivalent size at the surface because it is not exposed to environmental moisture and so will not fatigue due to stress corrosion.

While no severe defects were detected in the  $\sim 15 \text{ m}$  of fiber tested here, there is a possibility of very large flaws if much longer lengths of fiber were examined. Unlike the other properties of the fiber described here, which are average properties along the length of the fiber, strength depends on the extreme values of flaw sizes in the test length and so is well known to be length dependent. However, these early results on this fiber do conclusively show that the rapid quenching of a molten core during draw does not necessarily degrade the strength to the point where the fiber is unusable, at least on the length scale of tens of meters.

### *Residual Issues and Considerations*

The purpose of this paper was to provide a more in-depth analysis of the materials and physical properties of glass-clad optical fibers derived from a crystalline (YAG) core containing-preform. As with any initial study, there are a number of future efforts worth pursuing. More specifically, the following studies and developments would enable such fibers to be of greater value to the community:

- Determine through time, temperature, transformation thermal studies if it is possible to develop YAG crystallinity (or polycrystallinity) of the core. If polycrystallinity is achievable, then develop approaches to minimizing the grain size in order to optimize fiber transparency. Here previous work on glass ceramic optical fibers might be useful.[ ]

- There is a need for better understanding of the advantages and disadvantages of diffusion and other ways to control it (e.g., draw temperature, draw time, intermediate cladding layers as diffusion barriers, etc). Given the inevitability of diffusion, how might it be minimized or, at least, insightfully used to end with a core composition that provides desirable optical properties. The work of Ref. 7 proves that high degrees of crystallinity can be obtained in molten core-derived optical fibers even given moderate degrees of diffusion.
- Determine the application-specific balance between larger core size (i.e., less diffusion) and fiber flexibility.
- Develop approaches for tailoring the fiber numerical aperture for single mode operation as well as achieving more complex fiber designs.
- Continue to investigate the broadened range of materials and compositions permitted by such non-equilibrium molten core approaches to optical fibers.

### Section Conclusions

An in-depth analysis of optical fibers derived from a preform containing crystalline YAG as the starting core material. Conventional fiber draw parameters led to a core that was amorphous, which likely results from in-diffusion of silica from the cladding. Regardless, the resultant fibers exhibited background loss figures of  $\sim 0.1 - 0.3$  dB/m, room temperature thermal conductivity along its length that was roughly 20% higher than conventional optical fiber, and mechanical properties equivalent to standard optical fiber. The spectroscopic properties of Er<sup>3+</sup> doped into the precursor YAG corroborated the amorphous nature of the core material though the linewidth is somewhat narrower and fluorescence lifetime is somewhat longer than that in conventional silicate glasses. Efforts should continue to further evaluate the influence of processing conditions on core crystal composition (i.e., diffusion) and the potential development of a crystalline or polycrystalline core.

### Section References

1. E. Snitzer and R. Tumminelli, *Optics Letters* 14, 757 – 759 (1989).
2. J. Ballato and E. Snitzer, *Applied Optics* 34, 6848 – 6854 (1995).
3. N. Goel, R. Stolen, S. Morgan, J.-K. Kim, D. Kominsky, and G. Pickrell, *Optics Letters* 31, 438 – 440 (2006).
4. M. Fejer, J. Nightingale, G. Magel, and R. Byer, *Review of Scientific Instruments* 55, 1791 – 1796 (1984).
5. G. A. Magel, D. H. Jundt, M. M. Fejer, and R. L. Byer, *SPIE Proceedings on Infrared Optical Materials and Fibers*, Vol. 618, 89 – 94 (1986).
6. C. Lo, K. Huang, J. Chen, S. Tu, and S. Huang, *Optics Letters* 29, 439 – 441 (2004).
7. J. Ballato, T. Hawkins, P. Foy, R. Stolen, B. Kokuoz, M. Ellison, C. McMillen, J. Reppert, A. M. Rao, M. Daw, S. Sharma, R. Shori, O. Stafsudd, R. R. Rice, and D. R. Powers, *Optics Express* 16, 18675 – 18683 (2008).
8. Y. Huang, Y. Lu, J. Chen, Y. Hsu, Y. Huang, S. Huang, and W. Cheng, *Optics Express* 14, 8492 – 8497 (2006).
9. Y.-C. Huang, J.-S. Wang, Y.-K. Lu, W.-K. Liu, K.-Y. Huang, S.-L. Huang, and W.-H. Cheng, *Optics Express* 15, 14382 – 14388 (2007).

10. B. M. Zawilski, R. T. Littleton, and T. M. Tritt, *Review of Scientific Instruments* 72, 1770 – 1174 (2001).
11. “ITM-13 - Measuring dynamic strength and fatigue parameters of optical fibers by two-point bending,” TIA/EIA TSB 62-13, Telecommunications Industry Association, Washington, DC, (May 1, 2000).
12. “FOTP-28 - Method for measuring dynamic tensile strength and fatigue parameters of optical fibers by tension,” TIA/EIA-455-28-C, Telecommunications Industry Association, Washington, DC, (1999).
13. C.-Y. Lo, K.-Y. Huang, J.-C. Chen, C.-Y. Chuang, C.-C. Lai, S.-L. Huang, Y.-S. Lin, and P. S. Yeh, *Optics Letters* 30, 129 – 131 (2005).
14. B. N. Samson, P. A. Tick, and N. F. Borrelli, *Optics Letters* 26, 145 – 147 (2001).